A Study of Battery Energy Storage Dynamics in Power Systems

By

Damon Bazargan

A thesis submitted to the Faculty of Graduate Studies of
the University of Manitoba
in partial fulfillment of the requirements of the degree of

Doctor of Philosophy

Department of Electrical and Computer Engineering
University of Manitoba
Winnipeg, MB

Abstract

This thesis introduces an approach to study the effect of battery parameters on the stability and the response dynamics of a grid-connected battery energy storage systems (BESS). In this study, averaged-value modeling technique is used to formulate a grid-connected battery energy storage system. State equations are used to study the impact of battery parameters on system's performance. Furthermore, a fully-detailed transient model of a grid-connected battery energy storage system is developed in an electromagnetic transient simulation software (PSCAD/EMTDC). This model includes BESS components such as batteries, power-electronic converters, voltage source converters (VSCs) and BESS' controllers of all levels.

This research investigates the impact of battery parameters such as the internal resistance and the state of charge on the stability of BESSs and determines a stability region in which BESSs perform normal operation. It is shown that in an unstable region, the BESS is incapable of delivering the desired power to the grid. This research is also focused on improvement of BESS dc-link voltage regulation upon a change in the BESS power set-point and also BESS response dynamics in the grid. To analyse the stability region and improve the response dynamic of a BESS, an alternative configuration of battery cells in a battery bank is proposed and evaluated. Control systems of a BESS are also investigated as key contributors to the response dynamics of the system. A feed-back/feed-forward control strategy is proposed and evaluated to improve the response dynamic of a BESS.

The outcomes of this research are useful in the design stages of a BESS where response dynamics of an energy storage system is important. In addition, since the internal resistance of a battery increases by aging of battery cells, studying the effect of battery aging on BESS stability and operation is useful in annual maintenance of a commissioned BESS in the grid.

Copyright Forms

I acknowledge the use of the following IEEE copyrighted paper in preparation of this thesis. @ 2014 IEEE [D. Bazargan, S. Filizadeh, A. Gole, ”Stability analysis of converter-connected battery energy storage system in the grid,” *IEEE Trans. on Sustainable Energy*, vol. 5, no. 4, pp. 1204-1212, Oct. 2014]. In reference to IEEE copyrighted material which is used with permission in this thesis, the IEEE does not endorse any of University of Manitoba's products or services. Internal or personal use of this material is permitted. If interested in reprinting/republishing IEEE copyrighted material for advertising or promotional purposes or for creating new collective works for resale or redistribution, please go to the link below to learn how to obtain a License http://www.ieee.org/publications_standards/publications/rights/rights_link.html

Acknowledgement

Studying at the University of Manitoba is by far one of distinctive stages of my life where I experienced moments of love and hate, hope and disappointment, sadness and happiness and grew. I made lifetime friends without whom cold winter nights of Winnipeg was intolerable.

I had the chance to interact and cooperate with scholars of power systems and met with great people in academia and industry one of whom is Dr. Shaahin Filizadeh, my PhD advisor. I would like to thank him for his support and guidance during these years. His positive viewpoint motivated me in bottlenecks of my research project when I was disappointed of my results.

I also would like to thank Dr. Aniruddha Gole, my co-advisor. His knowledge and viewpoint was a great guide during the course of my studies at the University of Manitoba. He has been generous in sharing his experience with graduate students. He specially played an important role in improvement of team work attitude of students in power systems lab.

Most importantly, I would like to express my deepest thankfulness to my parents, who lovingly supported me during the course of this program as they always did in the rest of my life.

I am a believer that accomplishment of this research and the related coursework without the help and support of power systems group faculty and staff, my family and friends was not possible. At the end, I like to thank my wife, Seyedeh Sama, for her support during writing of my thesis and would like to dedicate this piece of work to her.

To my loving wife

who has made my life colorful with her love and presence

&

To my parents

who supported me in different stages of my life,
gave me confidence and taught me patience and hard work

Table of Contents

Table of Figures

List of Acronyms

BESS: Battery energy storage system

BMS: Battery management system

CAES: Compressed air energy storage

DoD: Depth of discharge

ESS: Energy storage system

FES: Flywheel energy storage

PHS: Pumped hydro energy storage

PLL: Phase lock loop

LPF: Low-pass filter

SoC: State of charge

SMES: Super-conducting magnetic energy storage

VSC: Voltage source converter

Chapter 1: Introduction

1.1 Introduction

Any mis-match in generation and consumption of electric power results in frequency and/or voltage deviations and may eventually cause instability in the grid [1], [2]. Hence, appropriate measures need to be taken to address control of power supply, and demand in the grid. This could be costly in certain circumstances; for example, generation, transmission, and distribution facilities need to have the capability to meet the maximum level of the demand. The maximum capacity may only be used infrequently and for short periods of time. As such, sizing generation, transmission, and distribution facilities to meet the maximum demand when the maximum capacity is not used frequently is not financially appealing and imposes extra costs on the end-users.

Alternatively, energy storage systems (ESSs) may be used to store electric energy in the grid to match the difference between power supply and demand. The electric energy may be stored in ESSs in different forms, e.g., chemical energy (in batteries), rotational kinetic energy (in flywheels), pressure potential energy (in compressed air storage systems), gravitational potential energy (in pumped hydro-electric facilities), electrical charges (in capacitors), and magnetic fields (in super-conducting magnetic energy storage) [3], [4], [5], [6]. Energy is restored and consumed in the form of electric energy when required. The stored energy is used when the supplied power is less than the consumed power. Hence, ESSs can be used to store excess generated energy in power systems. Besides, ESSs may also be used to reduce the cost of operation, and to improve power quality [7] [8] [9], reliability, and performance of the grid [5] [6] [10]. Various applications of ESSs are discussed in the next section of this chapter.

This study focuses on battery energy storage systems (BESSs) in the grid. BESSs, in particular those with lead-acid and lithium-ion battery banks, are considered as mature technology and are used worldwide; e.g., in 2013, 340 MWh of electric energy was stored in BESS facilities (mostly lead-acid and lithium-ion) in the United States [11].

Compared to other ESSs, BESSs have relatively low response time, and medium to high power and energy ratings, as will be discussed in the next section of this chapter. Consequently, BESSs may be used in high power or fast response applications such as bulk energy storage or power quality improvement applications [12].

This chapter continues with a brief introduction to energy storage systems. It describes different applications, types, and technologies of ESSs in the grid. Furthermore, it discusses the type of ESS that is typically used for each application. It also mentions parameters, key selection criteria, and location of ESSs in power systems.

After a brief introduction to ESSs, motivations and goals of this thesis will be described in the third section of this chapter. Finally, the last section highlights the steps taken to complete this research and outlines the remaining chapters of the thesis.

1.2 Energy storage systems in the grid

Energy storage systems may have different power (Watts) and energy (Watt-hour) ratings. In addition, other parameters that are usually addressed in type selection of ESSs include: response time, discharge duration, life cycle, and efficiency [13].

Response time indicates how quickly an ESS can reach the rated charge or discharge power capacity when required [14]. This is not the same for different ESSs and ranges from a few milliseconds to minutes. This parameter is important in successful scheduling of sources in

power systems; for example, the response time indicates the time in which a backup ESS can be online to compensate the lost power source if one source fails due to a fault in the grid [15].

Discharge duration presents the length of the period during which an ESS can discharge with rated power. The required discharge duration for each application is not the same. For example, for applications such as load levelling or peak-shaving, this could be in the order of hours while for power quality applications, the required discharge duration is in the order of seconds to minutes. Different applications of ESSs will be discussed later in this section.

Life cycle shows the number of cycles that an ESS is capable of storing and restoring energy. ESSs need to be replaced or have major overhaul beyond their life cycle. For example, in battery energy storage systems, internal resistance of cells increases with an increase in the number of cycles that the battery is charged and discharged. An increase in the internal resistance of battery causes a reduction in the efficiency of BESSs [16].

Efficiency is presented in the form of percentage and shows the ratio of the restorable energy to the stored energy in an ESS [4]. Due to losses in ESSs, only a percentage of stored energy is restorable. Efficiency of an ESS depends on the technology that is used in the ESS.

Table 1.1 compares different types of ESSs in terms of the parameters described above. This section continues with discussion on ESS technologies and applications.

1.2.1 Technologies

This section reviews deployed and mature technologies of energy storage systems in the grid. In terms of technological maturity, pumped hydro-electric storage systems, lead-acid and sodium sulfur BESSs may be classified as mature technologies. Compressed air storage systems, flywheels, sodium nickel chloride, sodium-ion, and lithium-ion BESSs are widely deployed in commercial targets. Super-conducting magnetic energy storage and super-capacitors are in

demonstration, and research and development phases [13]. Other types of ESSs with rare usage such as thermal energy storage systems are not discussed in this section.

Table 1.1: ESSs parameter comparison [13] [14] [17]

Technology	Power (MW)	Energy (MWh)	Efficiency (%)	Life cycle (x1000)	Response time	Discharge Duration
Pumped Hydro	280-1400	1700-14000	70-80	13	10 min	hours
CAES	50-180	1400-3600	50	10-13	10 min	hours
Flywheel	0.01-100	0.005-200	80-95	100	10 min	minutes
Batteries	0.01-100	0.001-200	60-80	2-5	seconds	hours
SMES	0.2-100	10^{-4}-0.2	95	40yrs	milliseconds	seconds
Capacitors	0.1-1	10^{-6}-10^{-3}	95	20yrs	milliseconds	seconds

Pumped hydro-electric energy storage systems (PHSs) consume electric energy to pump water to a higher altitude reservoir. Hence, energy is stored as gravitational potential energy. The stored energy is restored as electric energy by releasing water through turbine/generator units to a lower reservoir. Pumped hydro-electric energy storage systems form 99 and 95 percent of the worldwide and the US storage capacities, respectively [11], [18]. This technology is suitable for high energy and high power applications such as energy shifting applications or bulk energy storage. The major drawbacks of PHSs are scarcity of available sites for the large reservoirs, slow response time, high capital cost for deployment of the facility, and negative environmental impact [19].

Compressed air energy storage systems (CAESs) take in electric energy to store energy in the form of compressed air. The energy is then restored in the form of electricity by burning a mixture of pressurised-air and natural gas in combustion chambers [17]. The hot gas from the combustor is then used to move a turbine. A CAES plant mainly consists of (1) compressors, (2) a motor-generator unit, (3) a gas turbine, and (4) a compressed air storage tank. CAESs are commonly used in locations where implementation of pumped hydro-electric storage systems are

not possible. A CAES has a relatively long discharge duration, low capital costs and relatively high efficiency [19].

Flywheel energy storage system systems (FESs) consume electricity to store energy in the form of momentum of a spinning mass. The kinetic energy stored in the spinning mass is restored in the form of electric power via motor/generator units when required. FESs are suitable for applications with short discharge duration. Hence, FESs can be used to improve power quality and frequency of the grid. FESs have relatively high life cycles (See Table 1.1) [14]. The main advantage of flywheels comparing to BESSs is that they have a longer life cycle [19].

Battery energy storage systems (BESSs) store electric energy in batteries. Electro-chemical batteries use chemical reactions (oxidation and reduction) to store electric energy. A battery cell consists of an anode, a cathode, and an electrolyte environment. In the cathode and anode, oxidation takes place during charging and discharging process respectively (storing and restoring electric power) [20], [21]. BESSs are composed of (1) battery banks, (2) dc-dc converters, (3) voltage source converters (VSC), and (4) control systems. Different battery cells may be used in a BESS with different chemistries such as lead-acid, nickel-cadmium, sodium-sulphur or lithium-ion [19]. The structure and components of battery energy storage systems are discussed in detail in Chapter 2 of this thesis.

Super-capacitors (SCs) are also used to store electric energy in an electric field. A capacitor consists of two electric conductors separated by a non-conducting material. Super-capacitors store energy by physically separating electric charges. SCs have a long cycle life due to the fact that they have no moving parts. SCs have relatively high efficiency compared to other ESSs [4]. The major problem with capacitor is their short discharge duration. Therefore, capacitors are mainly used in power quality applications [19].

Super-conducting magnetic energy storage systems (SMESs) use electric energy to generate a magnetic field capable of storing energy. A magnetic field is produced by using super-conductor coils. The stored energy is released whenever needed by discharging the coil. A SMES is composed of four sub-systems, namely (1) a super-conducting coil with magnet, (2) a cryogenic system to keep the coil at a low temperature, (3) a power conditioning system that controls the flow of current into or out of the coil, and (4) a control unit that is used to coordinate between sub-systems. SMESs have high efficiency and fast response time. This makes SMES a good candidate for applications such as frequency control, dynamic voltage support, and power quality improvement [4]. The major drawbacks of SMES facility deployment includes high capital cost and environmental impacts [19].

1.2.2 Applications

Energy storage systems may be used in different applications. Each application may have specific power, specific energy, or response time requirements. In this section applications of ESSs in power systems are discussed. Applications of ESSs in power systems can be categorised as (1) time-shift of energy and (2) grid operation support. Table 1.2 shows a list of ESS applications in the grid. Each application will be discussed individually in this section.

Table 1.2: ESS applications in the grid

Energy time-shift applications	Grid operation support applications
1) Power supply demand balance 2) Load levelling 3) Electricity market applications 4) Levelling generated power 5) Applications in smart grid 6) Elimination of the need to upgrade transmission lines	1) Power back up 2) Power quality 3) Spinning reverse 4) Black start

In time-shift of energy applications, energy is stored in ESSs at one time (usually non-peak hours) and is used at a later time (usually peak hours). The energy is stored with different purposes as described below.

1) Keeping a balance between power supplied and consumed in the grid: Balancing power supply and demand using conventional generation plants such as fossil fuel and hydro-electric plant is not efficient. Frequent adjustments of power generation levels reduces life time and increases maintenance expenses in these plants. Thus, utilization of ESSs in the grid helps to have a constant power generation in conventional power generation plants.
2) Levelling the consumed energy by a load in the grid: ESSs may be used to level the consumed energy by a load in the grid [22]. In this application, the ESS is installed close to the load in power systems. This saves transmission line capacity for other local users and helps utility companies in terms of scheduling and grid management.
3) Storing power in off-peak time (low cost) and restoring power in peak time (high cost) for financial benefit: During peak hours, energy consumption in the grid is higher compared

to off-peak hours. Utilities have different tariffs for peak hours and non-peak hours to encourage users to shift their usage from peak hours to non-peak hours. Hence, storing power during non-peak hours and restoring power during peak hours results in financial benefits for ESS facility owners [23].

4) Levelling generated power for intermittent sources of energy, e.g., wind or solar: Due to the unpredictable nature of renewable sources of energy, generated power from these sources are not constant. For example, wind speed or solar irradiance in a region might change. ESSs help to level output power by storing excess energy and restoring energy when required. For this application, ESSs are installed close to the renewable sources of energy [24] [25].
5) Engagement in power management of a smart grid: Smart grids manage power supply and demand to minimise cost and environmental concerns. In a smart grid, a considerable amount of energy is generated by renewable distributed generators. Hence, as mentioned earlier, ESSs are required to maintain the system stability and improve the system reliability [17]. In addition, ESSs are required to actively balance the generated and consumed power.
6) Elimination of the need to upgrade a transmission line by providing required power to the end-users: There might be a need to upgrade a transmission line to meet the power demand during peak hours. This means that during non-peak hours, the transmission line is capable of transmitting the required power while an upgrade is required to meet the power demand during peak hours. Alternatively, an ESS can be installed close to the load to store power in non-peak hours and provide the restored power to the end-users during peak hours [26] [27].

In grid operational support applications, ESSs help to maintain power quality and reliability, e.g., power back up, voltage and frequency regulation, spinning reserve, and black start.

1) ESSs may be used in the grid as a power source back up to increase the grid reliability. This is a particularly interesting application in remote areas with no local power generation capability. In circumstances where the remote community is isolated from the main grid due to a transmission line fault, the backup ESSs provides alternative power to the community [3].
2) ESSs may be used to improve the power quality by contributing to voltage and frequency regulation of the power system. Changes in the grid voltage or frequency may happen due to an imbalance of power supply and demand in the grid. In these circumstances, an energy storage system with a fast response time (fractions of a second) may be used to compensate the power imbalance of the grid [12].
3) ESSs may be used as an online or off-line reserve capacity to meet electric demand in power systems. This is known as spinning reserve or non-spinning reserve, respectively. Spinning reserve and non-spinning reserve are needed to maintain the system frequency stability during emergency operating conditions and unforeseen load swings.
4) ESSs may be used as black-start aid in the grid. Black-start provides capacity and energy after a system failure. A black-start unit provides energy to help other units restart and provide a reference frequency for synchronization. Pumped hydro-electric storage systems have been widely used for this application [12].

Table 1.3 compares the required response time, the duty cycle and the discharge duration of ESSs in several typical applications. The required response time is usually mandated by utility

companies. The required response time for load shift applications is usually referred to as ramping capacity and is measured in MW/min [15].

An ESS may be installed at different voltage levels and/or locations in a power system. It may be installed close to a generation unit or at the customers' end depending on the size and application. For example, in load leveling or power backup applications, the ESS will be installed close to the customer, while in leveling generated power by renewable sources, the ESS will be installed close to generation. Figure 1.1 shows an overview of a power system with different types of ESSs in different locations.

Table 1.3: ESS application comparison [13]

Application	Required response time	Discharge duty cycle	Discharge duration
3 hour load shift	10 mins	1 event / day	3 hours
Fluctuation suppression	20 milliseconds	90 cycles / hour	10 seconds
Angular stability	20 milliseconds	1 event /day	1 second
Voltage stability	20 milliseconds	1 event/day	1 second
Frequency support	20 milliseconds	1 event/day	10 mins

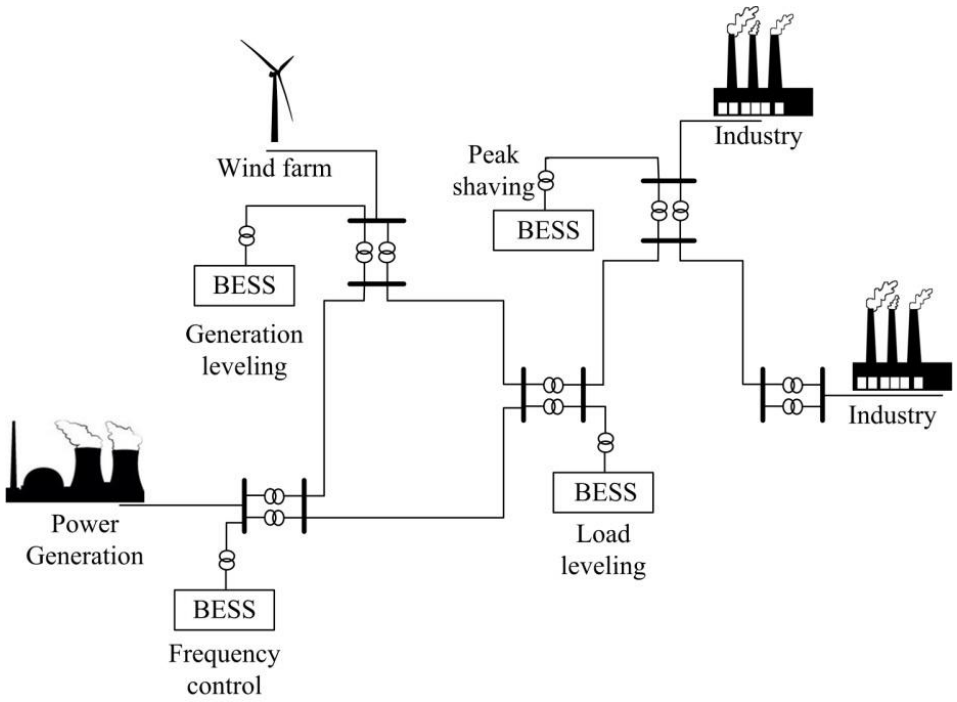

Figure 1.1: Schematic diagram of ESS location in the grid

In general, PHSs and CAESs are suitable for applications in scales above 100 MW with hours of discharge duration. They are used in time shifting applications. Flywheels, batteries, SMES and super-capacitors have a fast response (milliseconds) and therefore can be utilized for power quality applications [19].

1.3 Problem definition and research methodology

As discussed earlier, BESSs have many applications in the grid. With the increase in deployment of renewable sources of energy and implementation of smart grids in particular, it is anticipated that more BESS facilities will be deployed and will play key roles in power systems in future years. Hence, many researchers have focused on BESSs to improve their performance and operation.

In the existing literature, many aspects of a BESS have been studied as will be discussed in Chapter 2 of this thesis. These studies include aspects of operation [28] [29], economic assessment [30] [31] [32], design, and maintenance of BESSs [33]. BESSs have been studied in different applications such as in windfarms [34], solar PV systems [35] or in hybrid structure with a STATCOM in power systems [36]. These studies focus on challenges in each application or evaluate effective application of BESS in power systems.

As will be discussed in Chapter 2, BESSs consist of four main elements: (1) battery banks, (2) dc-dc converters, (3) voltage source converters, and (4) control units. Each component must be appropriately selected and sized for optimal operation of a BESS. [37], [38], [39] describe methods to size battery banks in a BESS. Appropriate sizing of a BESS facility is important for its economic operations. An oversized BESS is not economic due to excess capital costs, while an undersized BESS does not meet storage capacity requirements. [40] has used optimization

techniques to size BESS for peak shaving application and to level generated power of a solar PV system.

Most importantly, safe operation and failure modes of BESSs have been studied; e.g., [41] has studied fire hazards of BESSs. It has discussed the required electrical spacing of components, wiring criteria, controls, and failure modes of BESSs. As another example, [42] mentions developed codes and standards for deployment of BESSs in the grid from a safety standpoint. Considering the ongoing research on BESSs in the grid this thesis focuses on:

1) Studying the impact of battery parameters on BESS operation: In the literature, most studies focus on individual sub-systems rather than the system as a whole; for example [43] studies design of a dc-dc converter specifically for use in a BESS or [44] develops methods to improve battery operation in a BESS. Although literature review shows that many aspects of BESS operation and design have been covered, the author of this thesis believes that there is a gap in studying behaviour of a BESS as a system. A study with a systematic approach reveals the impact of system parameters on the performance and operation of a BESS. This research introduces an approach to study the impact of battery parameters on the operation of the BESSs. For this purpose, an averaged-value modeling technique is used to model a BESS in a power system. Afterwards a set of non-linear state equations are derived to represent a BESS. The state equations are capable of showing the system's behavior as will be shown in Chapter 3. Using state variable equations, it is possible to study the effect of system`s parameters (including battery parameters) on the system`s performance. The BESS averaged-value model is evaluated with EMT simulations of a detailed BESS model in PSCAD/EMTDC as will be shown in Chapter 3. Due to its high level of accuracy, an EMT model is generally believed to be a

high-fidelity representation of the nonlinear phenomena at hand. Hence, the EMT model is used as a benchmark in the simulations in this thesis.

2) Studying impact of battery parameters on the BESS stability in the grid: The BESS is studied with the intention of improvement of the BESS stability in this research. Improvement of BESS stability makes it a more reliable element of a power system. Improvement of a BESSs' stability may prevent unwanted outages in the grid. For this purpose, the effect of battery parameters on a BESS is studied by analysing the BESS state equations. The state equations are numerically solved for different operating points to identify the stable and the unstable regions. To enlarge the stability region a systematic approach to determine the configuration of the BESS battery bank is suggested in this thesis. The outcomes are evaluated by EMT simulations of a detailed BESS model in PSCAD/EMTDC. The study of battery parameter contributions to BESS stability has not been performed in the literature prior to this research to the best of the author's knowledge.

3) Improvement of BESS response dynamics: In this study, the impact of the battery`s internal resistance and the state of charge will be studied on BESS response dynamics. These are two important battery parameters as will be discussed in Chapter 2. To improve BESS response dynamics a systematic approach to adjust the configuration of BESS battery pack is suggested in this thesis. Furthermore, a feed-back/feed-forward controller is proposed and designed. Performance of the proposed methods are evaluated by EMT simulations of a detailed BESS model in PSCAD/EMTDC. Additionally, performance of the proposed feed-back/feed forward controller is evaluated through experiments on a small-scale BESS laboratory prototype. Neither the study of battery parameters' impact

nor the proposed feed-back/feed-forward controller on BESS performance has not been performed in the literature prior to this research to the best of the author's knowledge.

1.4 Limitations of this study

This study focuses on the operation of a BESS as a system. This study does not intend to focus on operation, optimal design and control, physical characteristics, and alternative topologies of components used in a battery energy storage system. For example studying the chemistry of batteries or optimisation of the dc-dc converter control system, voltage source converter and battery energy storage system are beyond the scope of this study. Furthermore, BESS components are modelled using averaged value modeling technique. Although this method simplifies the model and allows for derivations of closed-form formulae and development of control systems, it ignores high-frequency switching in the BESS components. Hence, it does neglect the system's higher order harmonics. Harmonics may adversely impact the performance of the system in particular if resonances exist in the system. In addition, this research does not study the impact of BESS on the operation of the grid. A BESS may have an impact on the operation of the grid such as increase of fault currents in the vicinity of the BESS location, change of power system's inertia, and the electricity bidding process in the grid.

1.5 Thesis organization

This chapter discussed applications and current technologies of energy storage systems in power systems. Important parameters in selection of an ESS technology were discussed. It also presented the problem definition, gap in the literature and the research methodology that will be used in this thesis.

Chapter 2 focuses on battery energy storage systems. At first, an overview of BESSs is presented. Afterwards, structure, topology, and components of a BESS is discussed. Important parameters for operation of batteries are discussed. In addition, the principle of operation of dc-dc converters and voltage source converters are explained. At the end, the control strategy of a BESS is presented in this chapter.

Chapter 3 is dedicated to modeling BESSs. The Shepherd battery model is presented in this chapter. Furthermore, averaged-value models of dc-dc converters and voltage source converters are presented. Afterwards, a BESS is modeled using averaged-value modeling technique and is represented in the form of a set of nonlinear state equations.

Chapter 4 presents stability analysis of a BESS using the state equations developed in Chapter 3. It also studies the required consideration for the BESS stability. The stability region for the BESS in terms of battery parameters is demonstrated in this chapter.

The thesis continues in Chapter 5 with a study of various approaches to improve BESS dc-link voltage regulation and response dynamics. The internal structure and control system of the BESS are investigated to find ways to improve the BESS response dynamics. In this chapter, EMT simulation cases of a detailed BESS model are presented to show effectiveness of the proposed methods in BESS response dynamic improvement. At the end, Chapter 6 presents a list of contributions of this study and suggests future works.

Chapter 2: Battery energy storage systems

Battery energy storage system facilities have been used in many countries and for different purposes in power systems. The increase in the penetration of renewable energy sources in the grid has caused an increase in the number of BESS facilities. Besides, government incentive programs and grid improvement strategies play an important role in this increase; for example, the state of California has mandated to have 1.325 GWh of installed energy storage facilities by 2020 [45], or ConEdison in the state of New York offers up to $2.10 per Watt-hour for installed advanced batteries [46].

This chapter explains the BESS structure and topology. Major components of a BESS will be explained. Furthermore, important battery parameters from an application standpoint are discussed. Battery types, basic principle of dc-dc converter operation, and basic principles of voltage source converter operation are presented in this chapter as well. At the end, the control systems of a BESS will be explained.

2.1 BESSs structure

A battery storage system is composed of battery banks, battery management systems (BMSs), fuses and switches, power conversion systems (dc to dc, and dc to ac), current, voltage, and power measurement tools, and communication and control systems.

Figure 2.1 shows a schematic diagram of components' interaction in a BESS. This figure also shows direction of the power flow within a BESS. Common topologies of BESSs are discussed later in this chapter.

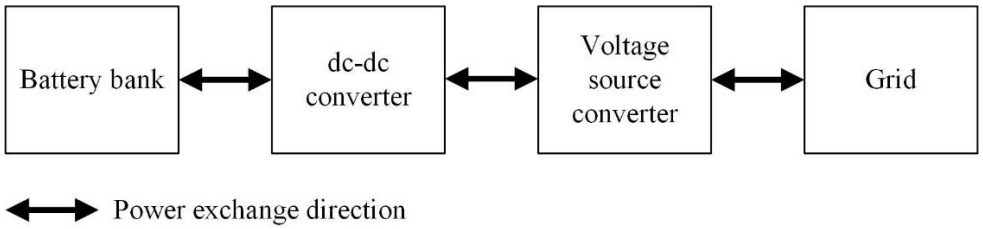

Figure 2.1: BESS component interaction schematic diagram

Battery banks consist of individual battery cells in series and/or in parallel. A group of battery cells (battery packs) are connected to each other via dc contactors to form battery banks. Dc contactors are used to disconnect a battery pack from the rest in cases where over/under-voltage or over-current occurs in a battery cell. Fuses and cooling systems are used in a battery pack to protect batteries against over-current and over-temperature [47]. Figure 2.2 shows the schematic diagram of a battery bank.

Battery monitoring and control systems, referred to as the battery management systems (BMSs), ensure safe operation of battery cells. BMSs are electronic boards composed of multiple digital and analogue inputs and outputs, central processing units, and also communication modules to communicate with supervisory control systems [48]. BMSs prevent individual cells from over-voltage, under-voltage, and over-temperature, and calculate the state of charge (SoC) in a battery cell. Battery cells are damaged in certain circumstances such as over-temperature, over-voltage and under-voltage. Definition of the state of charge is presented in detail in the next section of this chapter.

Power conversion systems such as dc-dc converters and voltage source converters (VSC) are used to connect battery banks to the grid. A dc-dc converter changes the level of dc voltage according to system requirements. A VSC converts dc to ac. A VSC is required for connection of dc equipment to the grid. Principles of operation of dc-dc converters and VSCs are discussed in the next section of this chapter.

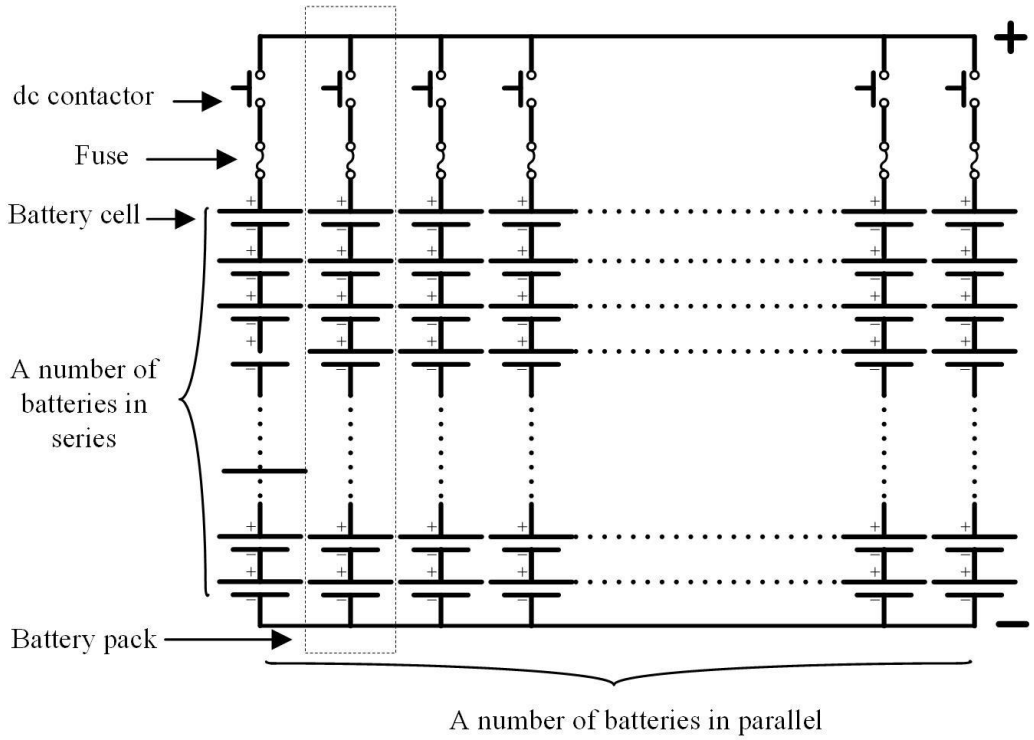

Figure 2.2: Structure of a battery bank in a BESS

The control system of a BESS uses measured values of current, voltage, and power to ensure that the delivered power is regulated and is equal to the power set-point. The power set-point could be positive or negative in value (the BESS may be storing or restoring energy) and is defined by the user. The control system of the BESS adjusts parameters of dc-dc converter and VSC such that the BESS exports/imports the set-point power to/from the grid. Principles of operation and topology of a BESS control system will be discussed in Section 2.3.

2.1.1 BESS topology

The components of a BESS may be connected to each other in different arrangements. This section discusses two most common arrangements. Figure 2.3 shows the schematic diagram of a BESS's component interconnections in a solar PV application. This topology is also used in low power (less than 20 kW) residential solar PV systems. Since the generated power by solar PV

panels is in the form of dc power, battery banks are connected to the solar PV panels via dc-dc converters. This means that solar panels can charge batteries directly (without the use of a VSC). Hence a local dc network is formed. Loads may also be connected to this local dc network to consume energy. The local dc network is then connected to the grid via a voltage source converter. As discussed earlier, BMSs actively monitor battery cells to prevent over/under-voltage and over-temperature conditions. The control system changes control parameters of the dc-dc converter and the VSC to ensure the required power is delivered/absorbed to/from the grid. This type of topology has limited applications in the literature due to complications of dc network implementation.

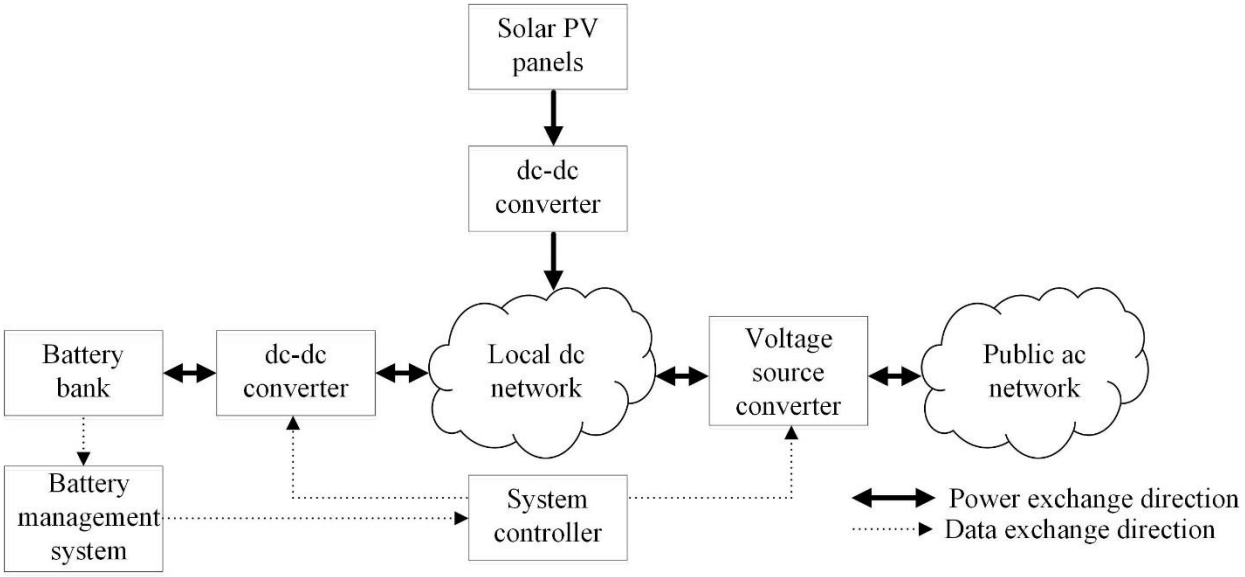

Figure 2.3: Topology of component interconnection in a BESS (solar PV application)

Figure 2.4 shows another BESS topology (BESS component inter-connection). This is the most common topology that has been used in the literature and is used in various BESS applications. In this topology, no local dc networks exist. The battery bank is connected to the grid via a dc-dc converter and a VSC. Furthermore, loads and other renewable sources are connected to the point of common coupling (PCC). The PCC is a point in the grid (shown as

public ac network in Figure 2.4) to which BESS, loads, and other power generation units are connected. In grid operation support applications, where a BESS is used to contribute to regulation of voltage and frequency in the grid, the voltage and frequency of the PCC are measured and regulated.

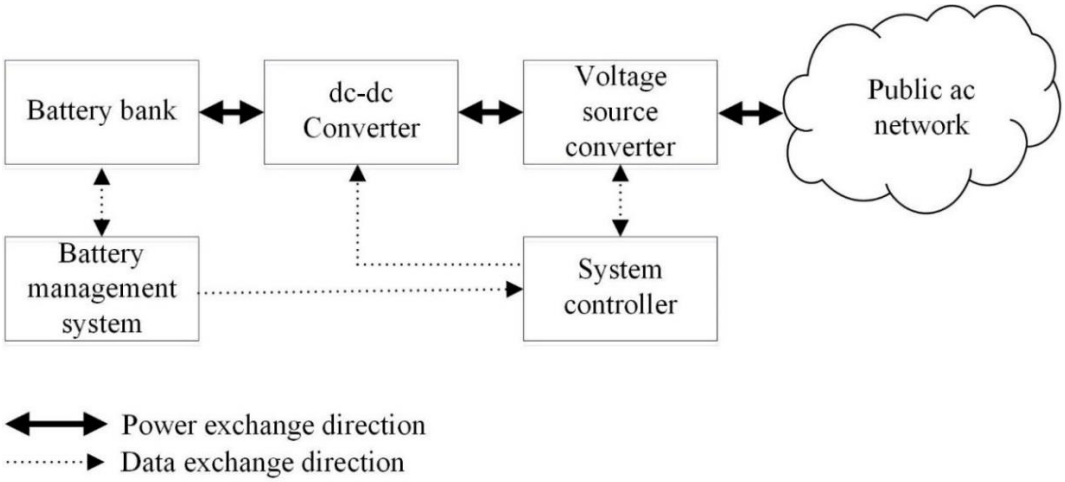

Figure 2.4: A common topology for BESS component connection

2.2 BESS Components

This section focuses on batteries, dc-dc converters, and voltage source converters (VSCs) used in a BESS. Batteries may differ in type and size. Section 2.2.1 discusses important battery parameters that are commonly used in battery applications. Section 2.2.2 describes battery types and characteristics. Sections 2.2.3 and 2.2.4 are dedicated to explaining the operation of dc-dc and voltage-source converters in a BESS, respectively.

2.2.1 Battery parameters

From an application standpoint, there are a certain number of battery parameters that needs to be monitored during the operation of a battery; such as, depth of discharge (DoD), efficiency, and state of charge (SoC) of the battery are among the parameters that need to be monitored.

Monitoring these parameters ensures safe and efficient operation of batteries in a battery energy storage system [49].

Depth of discharge (DoD) refers to the amount of the battery's capacity that has been used in each discharge cycle of the battery. It is expressed as a percentage of the battery's full capacity; for example, a 10 percent DoD indicates that 10 percent of the battery capacity is being used in each cycle (90 percent of energy stays in the battery cell). The deeper a battery is discharged during the life cycle, the shorter the expected life time. This is true for most of battery chemistries including lead-acid and lithium-ion [50].

Efficiency (shown by η) indicates the ratio of the restorable energy to the total stored energy. Efficiency is usually expressed in percentage. Only a certain percentage of the stored energy in a battery is restorable. This is due to loss of energy in battery cells. This loss could happen at the electrodes of the battery. This means that regardless of the energy storage time, a percentage of the energy is not restorable. Alternatively, another type of energy loss could occur due to chemical reactions in the battery during the energy storage process. In this type, the amount of energy loss is relevant to the time it takes to store energy. Efficiency of a battery is not constant and deteriorates with aging and degradation of the battery cell [51] [52].

Round-trip efficiency is the efficiency of a battery cell during a full charge-discharge cycle. The round-trip efficiency is usually calculated at the end of the charge-discharge cycle by measuring the restorable energy of the battery cell [53] [54].

State of charge (SoC) of a battery is an indicator of the level of accessible energy in a battery cell and is presented as a percentage. Equation (2.1) is used to calculate SoC in a battery cell. The numerator of the ratio shows integration of imported (positive) or exported (negative) current over time. The denominator shows rated capacity of the battery cell (in Ah). Since calculating the

available energy is the purpose of SoC, efficiency (η) is multiplied with the ratio in Equation (2.1) to consider the losses in the battery cell. This method of calculation of SoC is known as the coulomb counting method. This method is predominantly used to calculate SoC. Since this method integrates measured current, an error in measurement may be accumulated over time. Hence an enhanced coulomb counting method has been proposed in [55]. In this method, battery terminal voltage is measured to acknowledge when the battery is fully discharged. Battery terminal voltage drops significantly when the battery is depleted. The SoC is set to zero when the battery is fully depleted in the enhanced coulomb counting method. Thus the measurement error is not accumulated over time.

$$\mathrm{SoC} = \eta \frac{\int I(t)dt}{C} \tag{2.1}$$

2.2.2 Battery types

Conventional batteries are composed of electro-chemical cells. Each cell is composed of two electrodes (a cathode and an anode) and an electrolyte in a sealed container. During the discharge procedure, a reduction-oxidation reaction happens in the cell. During the discharge, electrons migrate from the anode (where oxidation occurs) to the cathode (where reduction occurs) [56]. On the other hand, during the charge procedure, the electro-chemical reaction is reversed. The electrolyte connects the anode and cathode and lets the ions move from side to side. Chemistries of the anode, the cathode, and the electrolyte are different in different types of battery cells. Hence, the chemical reaction is not the same either. The difference in chemistry of the cells causes different characteristics in battery cells such as different energy density, specific energy, efficiency, or life cycle. Energy density and specific energy are important factors in choosing

battery types in different applications. Energy density and specific energy are expressed in Watt-hours per litre (Wh/l) and Watt-hours per kilograms (Wh/Kg). Battery types with higher energy density and specific energy such as lithium-ion batteries are used mostly in mobile applications [57]. Table 2.1 shows the characteristics of different types of batteries. Common types of battery cells include: lead-acid, nickel-cadmium, sodium-sulphur, sodium-nickel-chloride, and lithium-ion.

Table 2.1: Battery cell characteristics [18]

Battery type	Cell voltage (V)	Energy density (Wh/L)	Specific energy (Wh/kg)
Lead–acid	2.0	50–90	25–50
Lithium-ion	3.7	250–676	75–200
Sodium–sulfur	~2.08	150–300	150
Nickel–Cadmium	1.0–1.3	50–150	40–60
Nickel–metal hydride	1.0–1.3	170–420	70–100
Sodium Nickel chloride	~2.58	150	94–120

Lead-acid batteries have been used in many energy storage facilities in power systems. Despite their low specific energy and power, short life cycle and high maintenance requirements, lead-acid batteries are a popular choice for BESSs due to their low cost. A lead-acid battery consists of lead metal and lead oxide electrodes in an electrolyte of about 37% sulphuric acid [19].

Lithium-ion batteries have high energy density and specific energy. Hence, lithium-ion batteries are widely used in mobile applications such as in electric vehicles or laptops. The electrodes in a lithium-ion battery are made of lithiated metal oxide graphitic. The electrolyte is made up of lithium salts dissolved in organic carbonates [19].

A sodium-sulphur battery consists of liquid sulphur and liquid sodium electrodes. The electrolyte is made of solid beta alumina ceramic. Sodium-sulphur batteries need to operate in a high temperature range (typically 300-350°C). This is a major drawback for these type of batteries [19].

Nickel-cadmium batteries consist of nickel hydroxide and cadmium hydroxide electrode plates and an alkaline electrolyte. Nickel-cadmium batteries have very low maintenance requirements. The main drawback of nickel-cadmium batteries is their relatively high cost [19].

Nickel-metal hydride batteries consist of nickel hydroxide and hydrogen absorbing alloy electrodes. Furthermore, nickel-metal hydride batteries have an alkaline electrolyte [19]. The nickel-metal hydride has less life cycle than nickel-cadmium. Nickel-metal hydride batteries suffer from high self-discharge, which is considerably greater than that of the nickel-cadmium batteries.

Sodium nickel chloride batteries (also known as ZEBRA) use liquid sodium and nickel chloride electrodes. Similar to sodium-sulphur batteries, the electrode is made of electrode solid beta alumina ceramic. It also operates at a high temperature range (typically 300-350°C). The required heat source for operation of this kind of batteries is a drawback in their application [19].

Batteries in a BESS are studied from an application standpoint in this study. Thus, parameters such as SoC (or internal battery voltage) or internal battery resistance are used in future chapters of this thesis. Focusing on the battery chemistry is not the intention of this study.

2.2.3 dc-dc Converters

Figure 2.5 shows the schematic diagram of a bi-directional dc-dc converter. A dc-dc converter is typically used to increase the level of battery bank voltage in a BESS. The shown dc-

dc converter (in Figure 2.5) is composed of switches (S_1, S_2), diodes (D_1, D_2), capacitors (C_1, C_2) and an inductor (L_1).

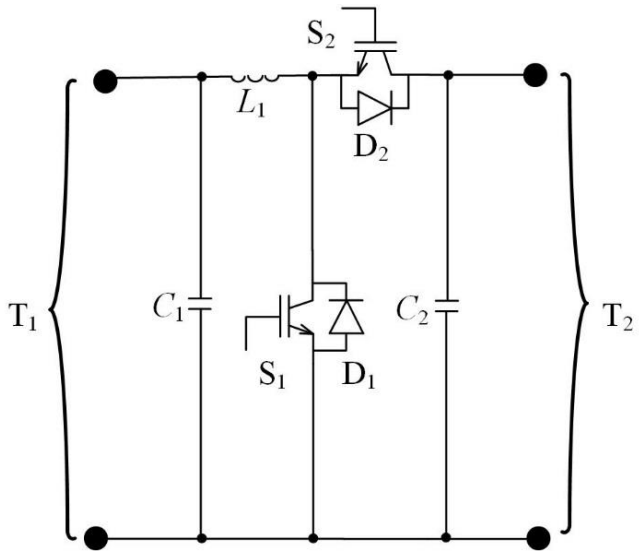

Figure 2.5: A bidirectional dc-dc converter

The battery bank is connected to one end of the converter in a BESS. Using this converter, power can travel in both directions; for example, if the battery bank is connected to terminal one (T_1), power can be transferred from the battery bank to terminal two (T_2) and vice versa. DC-DC converters are usually used to increase the battery bank's voltage level in a BESS. This means that usually the nominal voltage of terminal two (T_2) is more than the nominal voltage of terminal one (T_1). The bi-directional dc-dc converter operates in two modes: (1) boost (step-up), and (2) buck (step-down). Figure 2.6 shows the boost operating mode of a bi-directional dc-dc converter. In this mode power is transferred from terminal one (T_1) to terminal two (T_2). In the boost mode one of the switches (S_1) and one of the diodes (D_2) are active. S_2 and D_1 (see Figure 2.6) are not active in this mode.

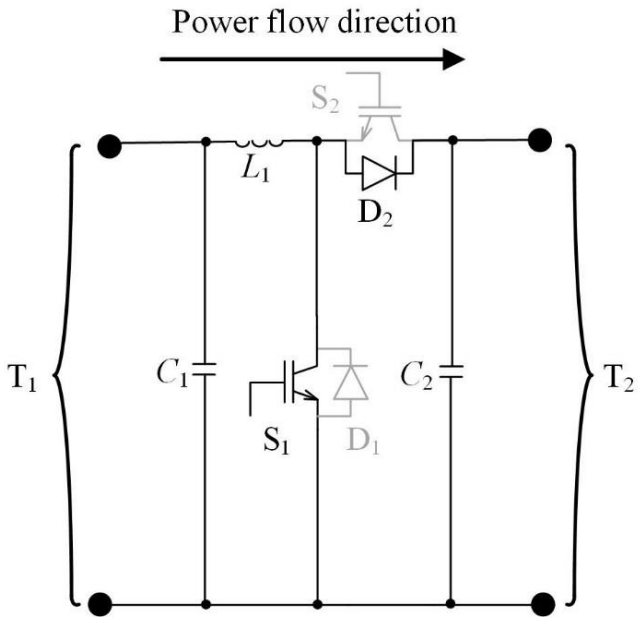

Figure 2.6: Boost dc-dc converter

Figure 2.7 shows the buck mode of a bi-directional dc-dc converter. In this mode, power is transferred from terminal two (T_2) to terminal one (T_1). In buck mode S_2 and D_1 are active. S_1 and D_2 (see Figure 2.7) are not active in this mode.

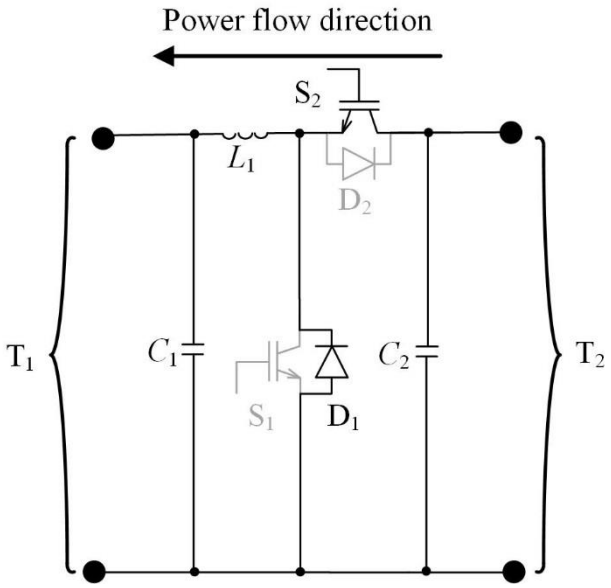

Figure 2.7: Buck dc-dc converter

In either boost or buck mode, the switches are only on for a period of time. The ratio of time in which the switch is on (T_{on}) over the total switching period (T_s) is known as the duty cycle. Equation (2.2) shows formulation of the duty cycle. Duty cycle is usually expressed in percentage. Duty cycle is a control parameter in a dc-dc converter and relates the input and the output terminal voltages of the boost and the buck converters. To derive an exact relationship between the terminal voltages (v_{T1} and v_{T2}) of the boost and the buck converter, the converter needs to be modeled. Chapter 3 is dedicated to modeling of the BESS components including the dc-dc converter. Usually a proportional integrator (PI) controller in a feed-back configuration is used to adjust the duty cycle according to system's power and/or terminal voltage requirements. Figure 2.8 shows schematic diagram of a PI controller.

$$\text{Duty Cycle} = \frac{T_{on}}{T_s} \tag{2.2}$$

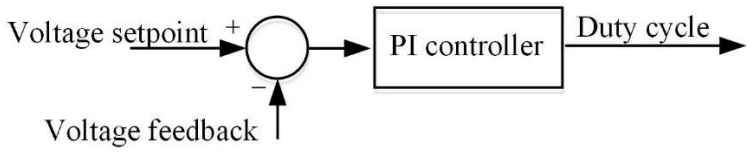

Figure 2.8: PI controller schematic diagram

The pulse-width modulation (PWM) technique is usually used to produce switching pulses in a dc-dc converter. The switching pulse is in Boolean form (either 1 when the switch is on, or 0 when the switch is off). In the PWM technique a reference signal is compared with a repetitive, high-frequency unity ramp. If the reference signal value is larger than the ramp value, the switching pulse is set to 1; otherwise it is set to 0. The frequency of the repetitive unity ramp is known as the switching frequency. Figure 2.9 shows the schematic diagram of the PWM

technique. As it appears from the figure, by increasing the value of the reference signal, the duty cycle of the converter increases [58] [59].

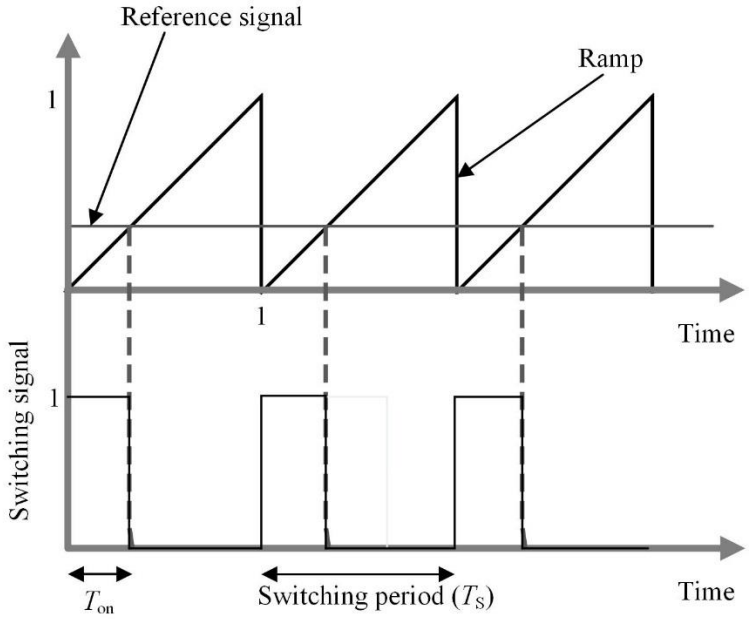

Figure 2.9: PWM technique in a dc-dc converter

2.2.4 VSC principles of operation

A voltage source converter (VSC) is used to convert dc power to ac power and vice versa in a BESS. A two-level single phase VSC is used to explain the operation of a two-level, 3-phase VSC in this section.

Figure 2.10 shows a single-phase VSC. An inductive-resistive (*RL*) load is connected to the VSC. Switches S_1 and S_2 operate one at the time in sequence to make a square wave voltage (see v_0 in Figure 2.10) across the load. Figure 2.11 shows output current and voltage waveforms of the two-level VSC shown in Figure 2.10. As shown in Figure 2.11, the current is lagging the voltage due to the inductive nature of the load. Although the voltage is a square wave it can be interpreted as a summation of sinusoidal waves with different frequencies by Fourier expansion.

Equation (2.3) shows the Fourier expansion of the load voltage (v_0 on the Figure 2.10) discussed above. Thus, the frequency of the first harmonic can be changed by a change in the switching frequency of the circuit shown in Figure 2.10. The amplitude of the fundamental harmonic can be controlled by the value of the voltage across switches (E in Figure 2.10). Thus, this method (square wave) does not provide a direct means for controlling the fundamental component. Besides, this method generates significant amount of higher order harmonics mainly in the low frequency band.

$$v_o = \sum_{k=0}^{n} \frac{4E}{k\pi} \sin\left(\frac{2\pi k}{T_s}\right) \tag{2.3}$$

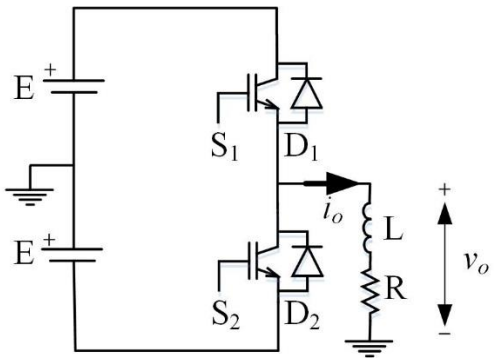

Figure 2.10: A single phase VSC

Figure 2.12 shows a PWM technique for the purpose of generating switching pulses (S_1 and S_2 switches) for a two level VSC. In this technique, a carrier signal is compared to a reference signal. If the value of the carrier signal is larger than the reference signal, the switch (S_1) is off; otherwise it is on. The status of the other switch (S_2) of the single phase VSC is complementary to that of the status of S_1. This means that if S_1 is on, S_2 is off and vice versa. The frequency of the carrier signal must be much higher than the frequency of the reference signal to prevent low

frequency harmonics in the output. In this method, the modulation index ($m=A_{\text{carrier signal}}/A_{\text{reference signal}}$) is defined as the ratio of amplitude of the reference signal to the carrier signal. The modulation index is used to control the amplitude of the generated voltage at the output of the VSC. Equation 2.4 shows formulation of the root mean square of first harmonic of the generated voltage in terms of the modulation index and voltage of the dc link ($2E$) in Figure 2.10.

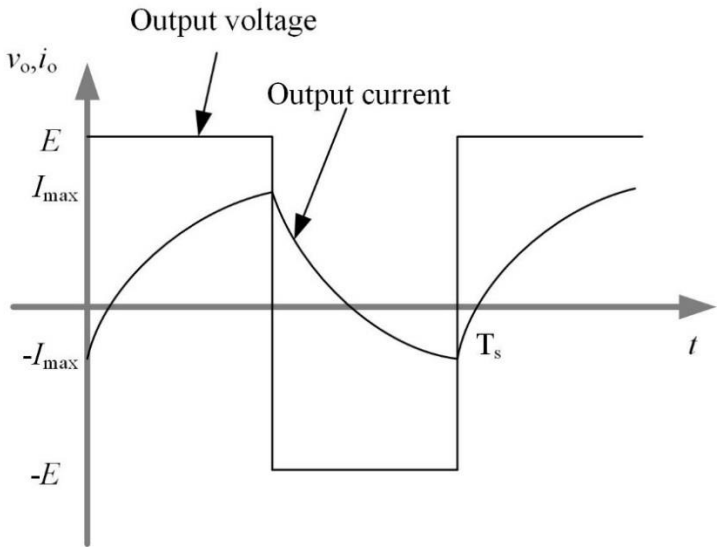

Figure 2.11: Voltage and current waveforms of a two-level VSC

$$V_{rms} = \frac{mE}{\sqrt{2}} \quad 0 < m < 1 \tag{2.4}$$

Figure 2.13 shows the schematic diagram of a 3-phase VSC. As shown, the 3-phase VSC is composed of 3 single phase VSCs that are operated with a 120 degrees phase difference from each other. This means that the generated waveforms at the outputs are 120 degrees apart. The operating principle of a 3-phase VSC is similar to the single phase VSC described earlier.

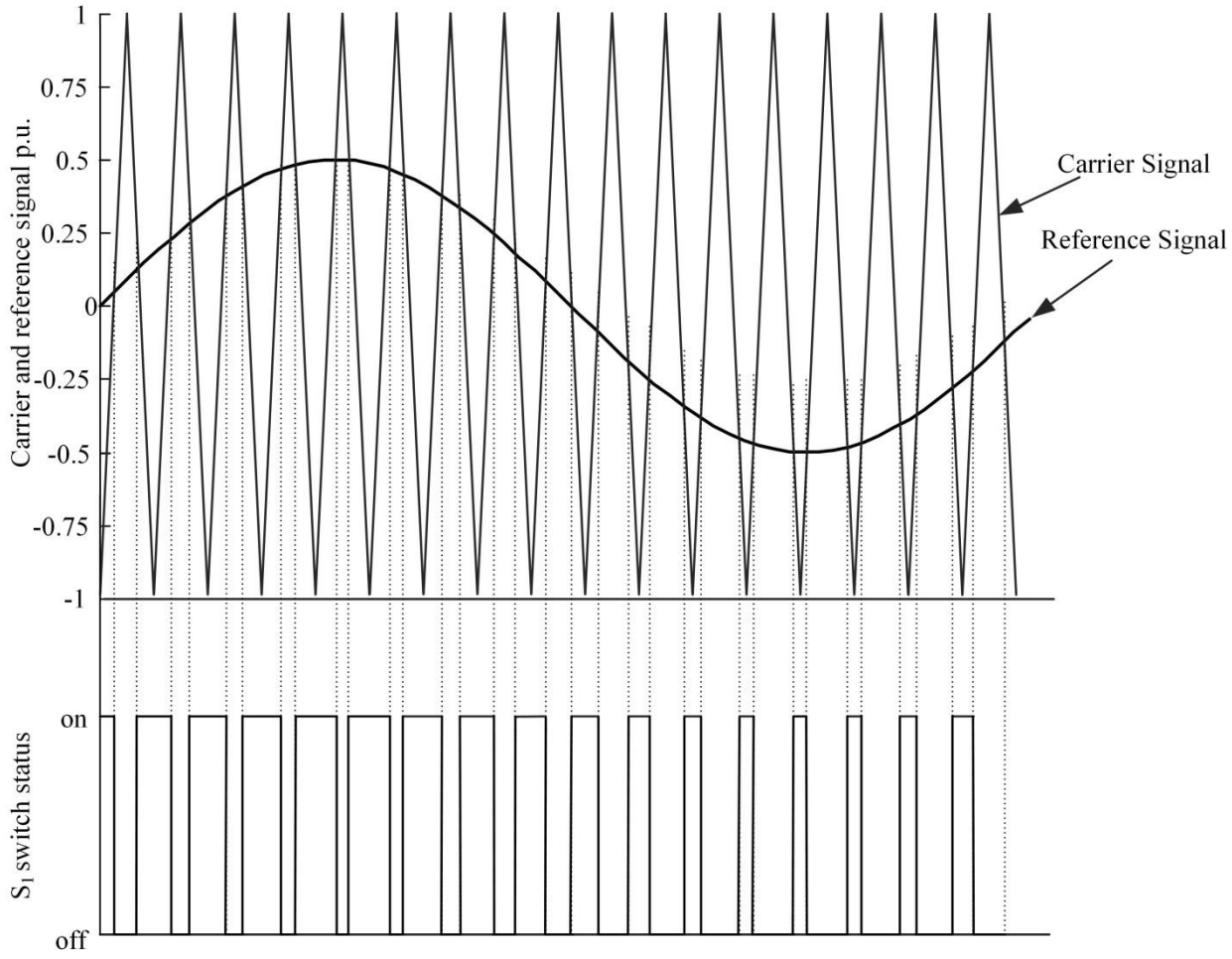

Figure 2.12: PWM technique for VSC switching signal generation

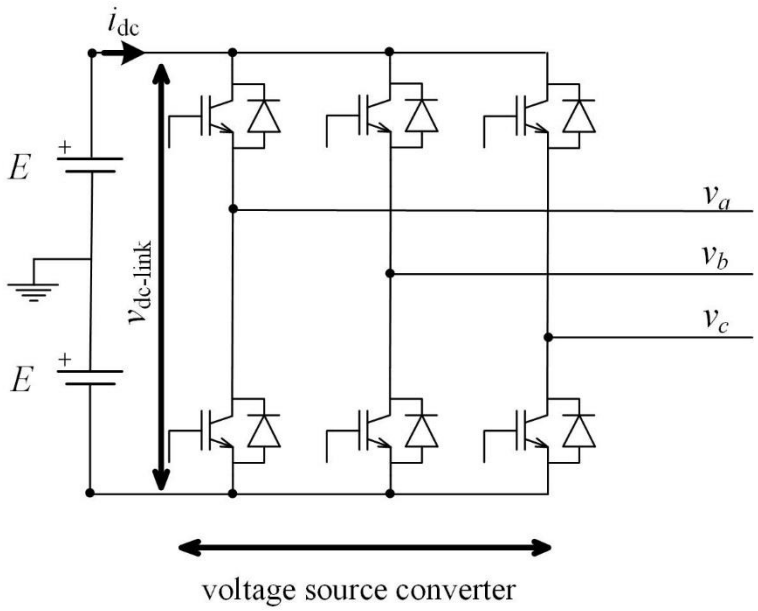

Figure 2.13: Three phase VSC schematic diagram

2.2.4.1 VSC control

In this section, the control system of a VSC is described. Figure 2.14 shows the schematic diagram of a VSC in interaction with an ac system. The VSC is connected to the ac system via line filters (series inductor and resistor). The inductor and resistor could also resemble a transformer (resistance and leakage impedance of the transformer). Equation (2.5) describes the relationship of circuit parameters in Figure 2.14. The voltage of the converter (v_c), voltage of the source (v_s), and the current (i) are in the form of vectors in (2.5). Like any ac system, assuming a constant phase and magnitude of the source voltage (v_s), the transferred active (P) and reactive (Q) power from the converter to the ac system depend on the phase and the magnitude of the converter voltage (v_c). Thus, the control system needs to control the phase and the magnitude of the converter voltage to meet the control targets.

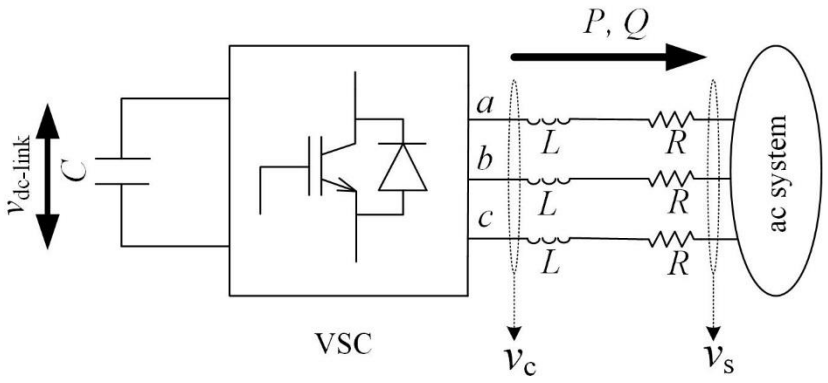

Figure 2.14: VSC power transfer

$$\vec{v}_c(t) = L\frac{d\vec{i}(t)}{dt} + R\vec{i}(t) + \vec{v}_s(t) \tag{2.5}$$
$$\vec{v}_c(t) = [v_{ca}(t), v_{cb}(t), v_{cc}(t)]^T$$
$$\vec{i}(t) = [i_a(t), i_b(t), i_c(t)]^T$$
$$\vec{v}_s(t) = [v_s(t), v_s(t), v_s(t)]^T$$

The qd0 transformation is used to transfer (2.5) to the qd0 frame. The qd0 transformation (often referred to as Park's transformation) is a transformation of the three-phase time-domain signals from a stationary phase coordinate system (abc) to a rotating coordinate system (qd0). As will be seen in this section, the VSC controller is designed to de-couple the coupled parameters in qd0 domain. Equation (2.6) shows Park's transformation. Park's transformation transforms any vector in the abc domain to a vector in qd0 domain. These vectors may be time-variant such as voltage or current of a 3-phase system. The angle θ is used in (2.6), which may vary with time. Thus, the qd0 domain is known as a rotating domain in the literature.

$$\vec{x}_{qdo} = \mathbf{K}.\vec{x}_{abc} \tag{2.6}$$

$$\mathbf{K} = \frac{2}{3}\begin{bmatrix} \cos(\theta) & \cos(\theta - \frac{2\pi}{3}) & \cos(\theta + \frac{2\pi}{3}) \\ \sin(\theta) & \sin(\theta - \frac{2\pi}{3}) & \sin(\theta + \frac{2\pi}{3}) \\ \frac{1}{2} & \frac{1}{2} & \frac{1}{2} \end{bmatrix}$$

As mentioned, Park's transformation is used to transfer (2.5) to the qd0 domain. To do this, matrix K is multiplied to both sides of (2.5) as shown below in (2.7).

$$\begin{aligned} v_{c-qd0} &= \mathbf{K}.v_{c-abc} = \mathbf{K}.L.\frac{d}{dt}\mathbf{K}^{-1}i_{qd0} + \mathbf{K}.R.\mathbf{K}^{-1}.i_{qd0} + \mathbf{K}.v_{s-qd0} \\ &= (\mathbf{K}.L.\mathbf{K}^{-1}).\frac{di_{qd0}}{dt} + \mathbf{K}.L.i_{qd0}.\frac{d}{dt}\mathbf{K}^{-1} + R.i_{qd0} + \mathbf{K}.v_{s-qd0} \end{aligned} \tag{2.7}$$

Equation (2.7) is simplified and is shown in (2.8) and (2.9). These equations relate the converter voltage (v_c) and the source voltage (v_s) in the qd0 domain (q and d projections); for example, the converter voltage (v_c) is decomposed into a projection onto the q axis (v_{cq}) and a projection onto the d axis (v_{cd}). Equations (2.8) and (2.9) describe voltages and currents of a VSC and the terminating ac system.

$$v_{cq} = R.i_q + \omega L i_d + L\frac{d}{dt}i_q + v_{sq} \tag{2.8}$$

$$v_{cd} = R.i_d - \omega L i_q + L\frac{d}{dt}i_d + v_{sd} \tag{2.9}$$

Figure 2.15 shows the schematic diagram of the ac system and the control strategy that is used to control the VSC. The system in Figure 2.15 shows the schematic diagram of (2.8) and (2.9). The controller is formed in a way to de-couple q and d projections of voltages and currents. Thus by further simplification, the coupled terms are cancelled out. Figure 2.16 shows the simplified

control systems of the VSC. After de-coupling, a first-order model remains. It is now straightforward to design two controllers, $C_d(s)$ and $C_q(s)$, for the simplified model. Assume that the controller $C_d(s)$ is in the general format of a PI controller as described in Equation (2.10).

$$C_d(s) = \frac{k_p s + k_i}{s} \tag{2.10}$$

The closed-loop system is simplified as in Equation (2.11). The time constant (τ) is defined by the designer as per system's requirements. Parameters of the PI controller are shown in Equations (2.12) and (2.13). The same principle applies to the design procedure of $C_q(s)$.

$$\frac{i_d(s)}{i_{d-\text{ref}}(s)} = \frac{1}{\tau s + 1} \tag{2.11}$$

$$k_p = L/\tau \tag{2.12}$$

$$k_i = R/\tau \tag{2.13}$$

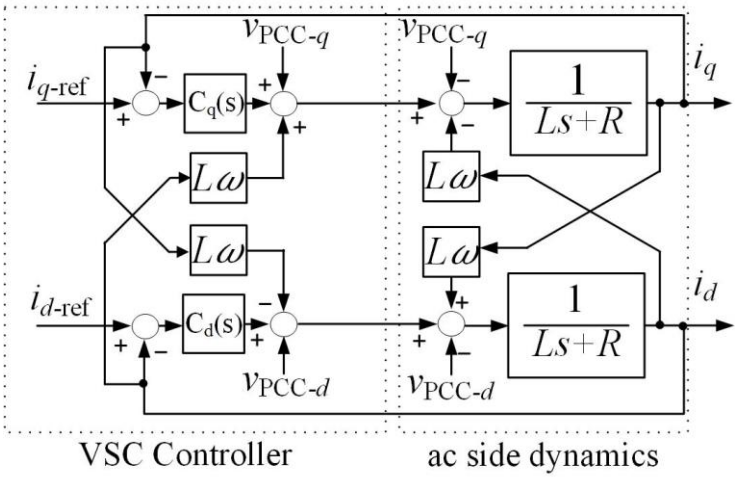

Figure 2.15: VSC controller

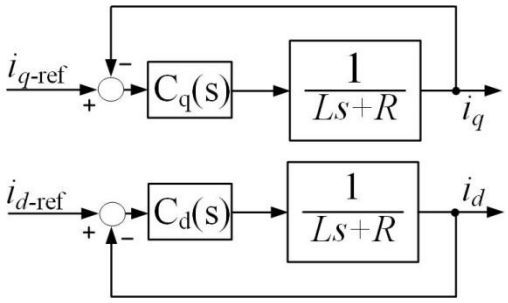

Figure 2.16: Simplified VSC controller

The ultimate goal of the control systems is to regulate the VSC's real power (in a BESS). Equation (2.14) shows the instantaneous power in terms of phase voltage and currents in a VSC (abc domain). Park's transformation is applied to Equation (2.14) to determine power in the qd0 domain. Equation (2.15) and (2.16) show VSC real (P) and reactive power (Q) in the qd0 domain.

$$P = v_{sa} i_a + v_{sb}.i_b + v_{sc}.i_c \tag{2.14}$$

$$P = \frac{3}{2}(v_{sd}.i_d + v_{sq}.i_q) \tag{2.15}$$

$$Q = \frac{3}{2}(v_{sq}.i_d - v_{sd}.i_q) \tag{2.16}$$

In practial applications a phase lock loop (PLL) is used to track the phase angle of the point of common coupling (PCC). PCC phase angle is used as a reference in the calculation of the converter voltage angle according to the control criteria. Assume that the voltage of the ac system is as in (2.17) and $\theta=\omega t$ (θ is the angle used in the calculation of K in Park's transformation). Then the q and d projection of the voltage would be as indicated in (2.18) and (2.19). Hence, (2.15) and (2.16) are simplified as shown in (2.20) and (2.21) [60] [61]. These equations show that the real and reactive power of the VSC can be independently controlled by changing the current componenets in the q and d directions, respectively.

$$\begin{aligned} v_{sa} &= V_m.\cos(\omega t) \\ v_{sb} &= V_m.\cos(\omega t - \frac{2\pi}{3}) \\ v_{sc} &= V_m.\cos(\omega t + \frac{2\pi}{3}) \end{aligned} \tag{2.17}$$

$$v_{sq} = V_m \tag{2.18}$$

$$v_{sd} = 0 \tag{2.19}$$

$$P(t) = \frac{3}{2}(V_m.i_q) \tag{2.20}$$

$$Q(t) = \frac{3}{2}(V_m.i_d) \tag{2.21}$$

2.3 BESS control

This section discusses the control system of the BESS. The operation of major BESS components was discussed in the previous sections of this chapter. This chapter basically combines converter and VSC control systems and describes how they operate together. Figure 2.17 shows a schematic diagram of the BESS components.

When the BESS is discharging with a specific power set-point, the VSC ensures that the set-point power is exported from the BESS by adjusting its modulation index and phase angle. Thus, the stored energy in the VSC dc-link reduces and so does the voltage of the dc-link ($v_{\text{dc-link}}$). The dc-dc converter ensures that the dc-link voltage is maintained by exporting energy from battery to the dc-link. Maintaining the dc-link voltage is important for normal operation of the VSC. Thus, the dc-dc converter operates in boost mode. This means that the battery bank will be discharged and the energy is transferred from the battery bank to the dc-link (capacitor).

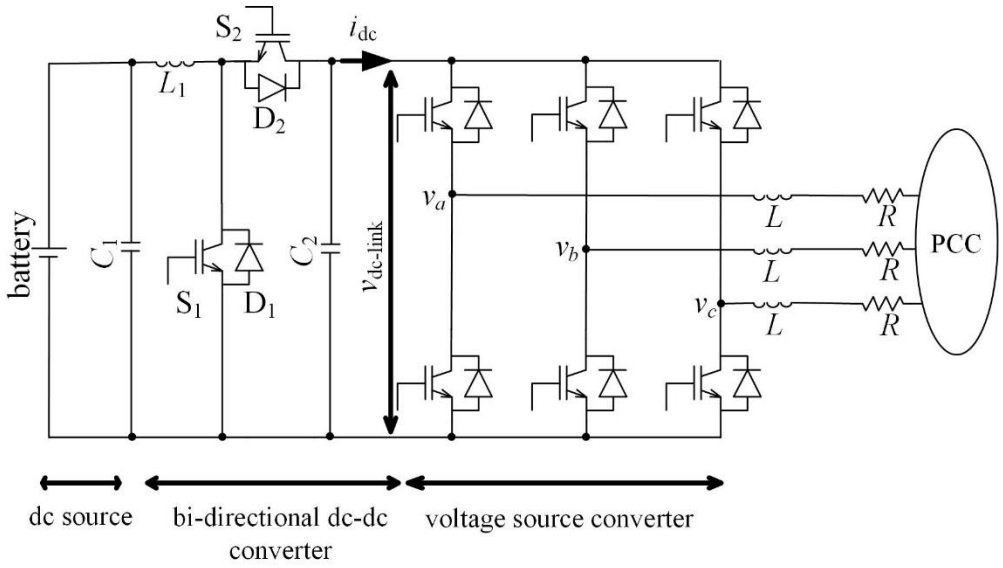

Figure 2.17: BESS structure

Alternatively, when the BESS is charging with a specific power set-point, the VSC ensures that the required power is imported from the grid by adjusting its modulation index and the phase angle. This increases the energy on the dc-link and also the dc-link voltage. The dc-dc converter adjusts the dc-link voltage by charging the battery bank (removing energy from dc-link). Therefore, power will be transferred from the dc-link to the battery bank.

Figure 2.18 shows a BESS's control system. As mentioned earlier, this is a combination of the dc-dc converter and the VSC control systems. The use of PI controllers is the standard control methodology in the literature and practical systems for converters. Hence, the used of PI controllers is preferred to the use of other control methods such as adaptive or predictive control methods in this study.

2.4 Chapter Summary and contributions

This chapter reviewed different type of batteries, common battery parameters from a battery application stand-point, and the BESS structure and topology. The basic operation principles of the dc-dc converter and the VSC were also described in this chapter. In addition, the control system of a BESS was described in the last section of this chapter.

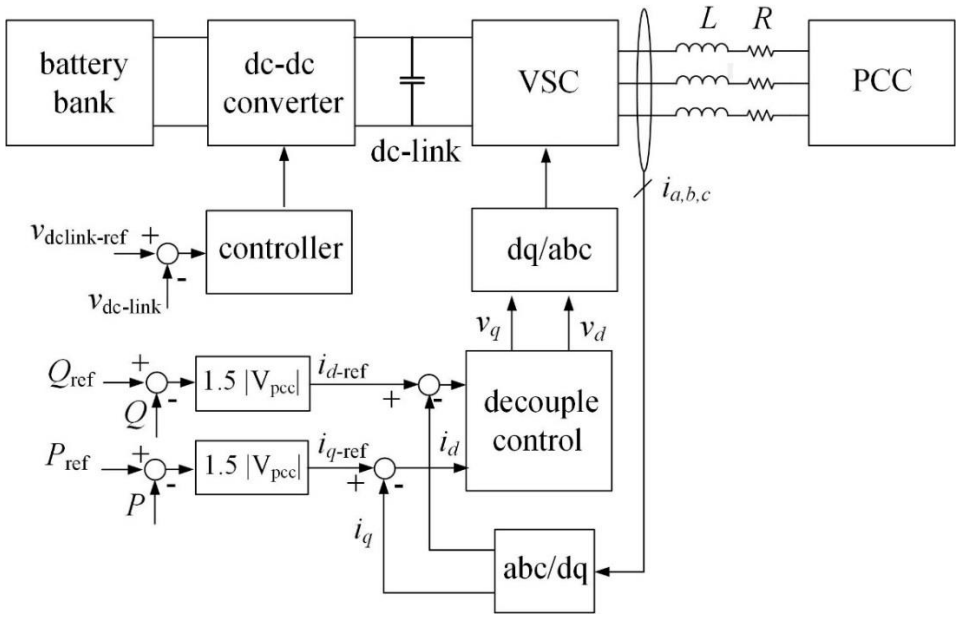

Figure 2.18: A BESS's control system

Chapter 3 Modeling

This chapter models a grid-connected BESS. A model is required to analyse the stability and the dynamic characteristics of the BESS in the grid. In this chapter, at first BESS components are modeled individually. The Shepherd model, which is widely used in the literature to model a battery, is presented in this chapter. Afterwards, the dc-dc converter will be modeled using a discontinuous conduction mode averaged-value model. A reduced-order model and a full-order model will be presented in this chapter for the buck and the boost modes of the dc-dc converter. The reduced-order and the full-order models will then be compared against each other. Then, the VSC will be modeled using an averaged-value modeling technique. The VSC will be modeled as a variable resistor in this chapter to facilitate further modeling of the BESS. Finally, a set of four non-linear state equations will be presented for a grid-connected BESS model.

3.1 Battery model

This section describes the Shepherd battery model. This model is widely used in the literature due to its simplicity and relatively high accuracy. The Shepherd battery model can be tuned for a specific battery by adjusting model parameters. This is usually done by matching the real and battery model discharge curves for a specific type of battery [62].

A Shepherd model is composed of a variable voltage source and a constant resistor. The variant voltage source and the resistor represent the battery cell voltage and the internal resistance, respectively. The voltage of the battery cell dependents on the battery's SoC as in (3.1). The values of A, B and K are presented in (3.2), (3.3), and (3.4), respectively. Values of V_{exp}, Q_{exp}, V_{nom}, Q_{nom}, V_{full} depend on the battery characteristics and are defined by extracting

information from the discharge curve of the battery at 0.2C discharge rate [63] [64]. Figure 3.1 shows the Shepherd battery model parameters on a typical battery discharge curve. The internal resistance of the battery is usually measured for a specific type of battery and is used as the value of the resistor in this model. Figure 3.2 shows the schematic diagram of a Shepherd battery model.

$$V = V_0 - K\frac{Q}{Q - \int i(t)dt} + A\exp(-B\int i(t)dt) \tag{3.1}$$

$$A = V_{\text{full}} - V_{\text{exp}} \tag{3.2}$$

$$B = \frac{3}{Q_{\text{exp}}} \tag{3.3}$$

$$K = \frac{(V_{\text{full}} - V_{\text{nom}} + A(\exp(-BQ_{\text{nom}}) - 1))}{Q_{\text{nom}}}(Q - Q_{\text{nom}}) \tag{3.4}$$

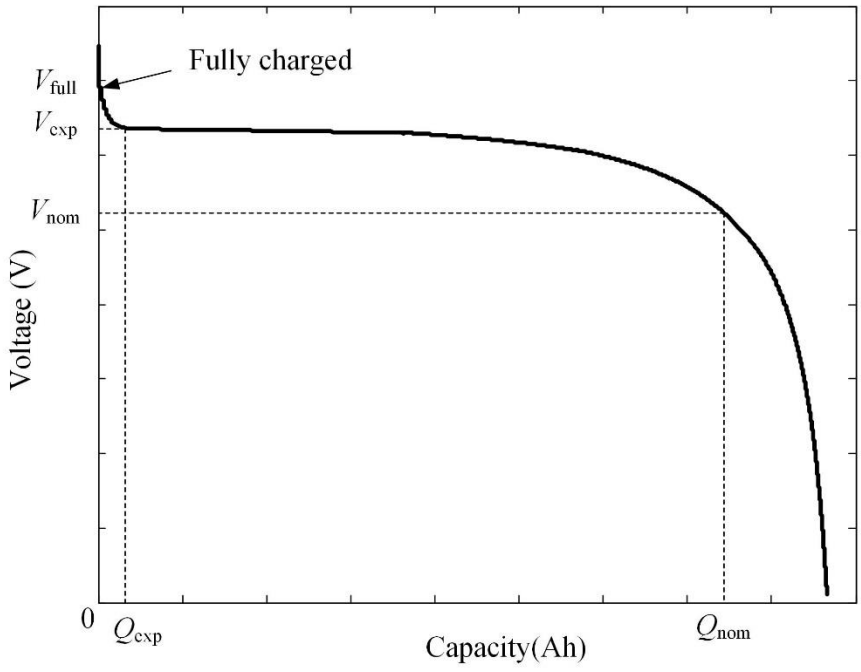

Figure 3.1: Shepherd battery model parameters on a battery discharge curve

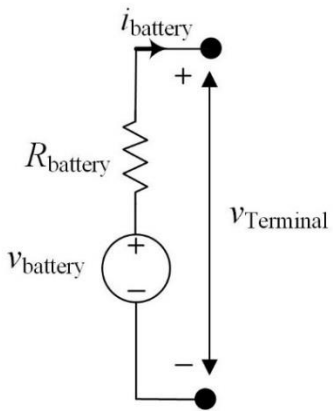

Figure 3.2: Schematic diagram of the Shepherd battery model

3.1.1 Battery bank model

The structure of a battery bank was discussed in Chapter 2. A battery bank is composed of a number of batteries in series (m) and parallel (n). Assuming that the same type of battery is used in a BESS, by using basic circuit rules, an equivalent circuit of the battery bank will be developed in this section. In the equivalent circuit, the equivalent battery bank voltage source ($v_{battery}$) equals to m times the single battery cell voltage ($v_{batt\text{-}cell}$) and the resistor in the equivalent circuit ($R_{battery}$) equals to m/n times the single battery cell internal resistance ($R_{batt\text{-}cell}$). Figure 3.3 shows a schematic diagram of the equivalent circuit of a battery bank. This equivalent circuit model will be used in Chapter 4 to analyse the configuration of battery cells in a battery bank.

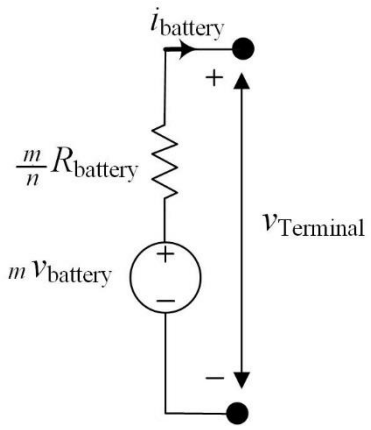

Figure 3.3: Equivalent circuit of a battery bank

3.2 dc-dc Converter model

In this section a BESS's dc-dc converter will be modeled. An averaged-value modeling technique is used to model the dc-dc converter in discontinuous conduction mode (DCM) for boost and buck modes separately. In the DCM mode, the inductor current may be zero for a portion of the switching period.

The analysis presented in this thesis is based on averaged-value modeling, where the effect of high-frequency switching is neglected. In practice, high frequency switching will cause ripples in the voltage and currents of the BESS.

A reduced-order model and a full-order model are developed for buck and boost converters. In the reduced-order model, unlike the full-order model, the inductor current does not appear as a state variable.

As discussed earlier in Chapter 2, a dc-dc converter connects the battery bank to the VSC. This means that battery bank is connected to one terminal of the converter as the other converter terminal is connected to the VSC. To simplify the BESS modeling steps and to keep the notations in this thesis unified, the dc-dc converter is assumed to be connected to the battery bank at this

stage without loss of generality. Thus as will be shown, the internal resistance of the battery bank ($R_{battery}$) and the battery bank voltage ($v_{Battery}$) appear in the dc-dc converter's describing equations.

3.2.1 State space averaging

In state-space averaging approach, matrix elements are averaged over different intervals. This method of averaging is known as state-space averaging in the literature [65] [66]. Equations (3.5)-(3.7) show state space equations of a typical system for three time intervals. x is the state variable in these equations.

$$0 < t < d_1 T_S : \dot{x} = a_1 x + b_1 u \tag{3.5}$$

$$d_1 T_S < t < (d_1 + d_2) T_S : \dot{x} = a_2 x + b_2 u \tag{3.6}$$

$$(d_1 + d_2) T_S < t < T_S : \dot{x} = a_3 x + b_3 u \tag{3.7}$$

$$\dot{\bar{x}} = [d_1 a_1 + d_2 a_2 + (1 - d_1 - d_2) a_3]\bar{x} + [d_1 b_1 + d_2 b_2 + (1 - d_1 - d_2) b_3]u \tag{3.8}$$

Equation (3.8) shows the state-space average of equations (3.5)-(3.7). In this method, it is assumed that the average of product terms over a switching cycle is the same as the product of averages. For example this implies $\sum_{i=1}^{3} (a_i d_i . x) = \sum_{i=1}^{3} (a_i d_i) . \bar{x}$. This assumption is valid if the state variable is not zero [67], for example for dc-dc converter in continuous conduction mode (CCM). In discontinuous conduction mode (DCM), the average of product terms is the same as the product of averages for non-zero state variables such as converter input and output voltages, but since the inductor current is zero, by definition in DCM in a converter, this assumption is not valid for this state variable. For the i_L state variable, in particular, the state space averaging

method needs to be modified. Thus, the average inductor current using the state space averaging method needs to be divided by the term "d_1+d_2" [67].

3.2.2 Boost dc-dc converter modeling

Figure 3.4 shows a schematic diagram of a boost dc-dc converter. The inductor current (i_L) increases when the switch is on and decreases when it is off. Figure 3.5 shows the inductor current during a switching period in the boost dc-dc converter. The switching period is divided into three intervals based on the status of the switch (S_1) and diode (D_1). The state equations of the dc-dc converter are separately analysed in each interval and are averaged over time to determine the average model of the converter. Figure 3.6 shows the schematic diagram of the boost converter in the first time-interval. In this interval, the switch is on and the diode is off. Equation (3.5) shows the state equation of the circuit in this time-interval. The inductor current (i_L), voltage of the input (v_{T1}), and output terminal ($v_{dc\text{-}link}$) are the state variables in (3.9).

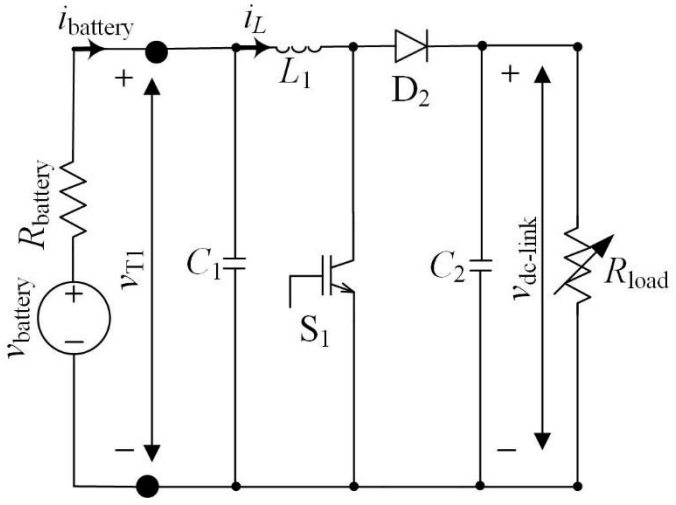

Figure 3.4: A boost dc-dc converter

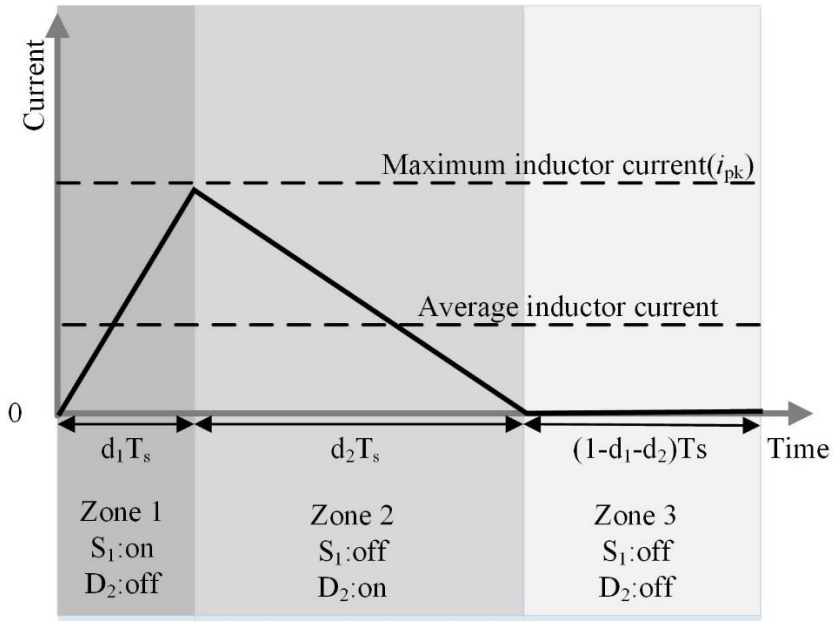

Figure 3.5: Inductor current in a boost dc-dc converter

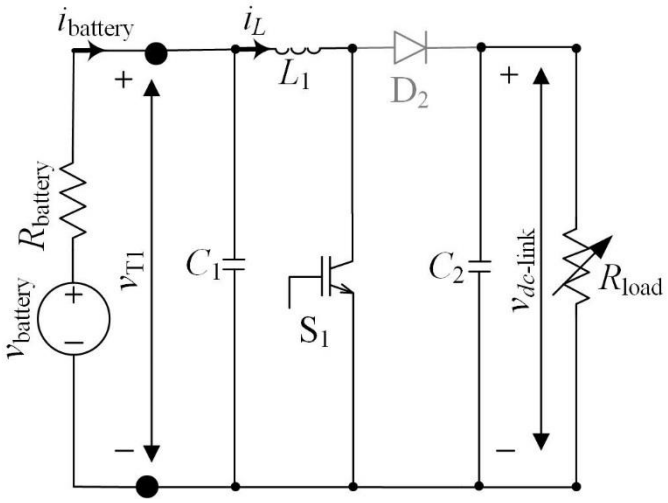

Figure 3.6: A boost dc-dc converter in time-interval 1

$$0 < t < d_1 T_S :$$

$$\frac{d}{dt}\begin{bmatrix} i_L \\ v_{T1} \\ v_{\text{dc-link}} \end{bmatrix} = \begin{bmatrix} 0 & \frac{1}{L} & 0 \\ \frac{-1}{C_1} & \frac{-1}{C_1 R_{\text{battery}}} & 0 \\ 0 & 0 & \frac{-1}{C_2 R_{\text{load}}} \end{bmatrix} \begin{bmatrix} i_L \\ v_{\text{T1}} \\ v_{\text{dc-link}} \end{bmatrix} + \begin{bmatrix} 0 \\ \frac{1}{C_1 R_{\text{battery}}} \\ 0 \end{bmatrix} v_{\text{battery}} \tag{3.9}$$

Figure 3 shows the schematic diagram of the boost dc-dc converter in the second time-interval. In this time-interval the diode (D_2) is on and switch (S_1) is off. Equation (3.10) shows the state equations of the dc-dc converter in this time interval.

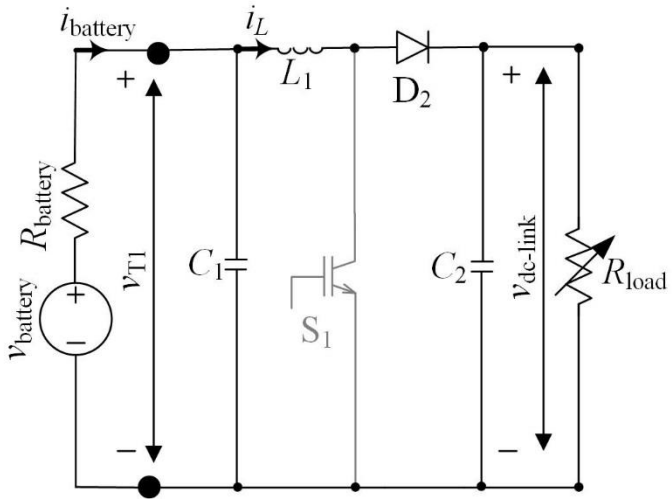

Figure 3.7: A boost dc-dc converter in time-interval 2

$$d_1 T_S < t < (d_1 + d_2) T_S :$$

$$\frac{d}{dt}\begin{bmatrix} i_L \\ v_{\text{T1}} \\ v_{\text{dc-link}} \end{bmatrix} = \begin{bmatrix} 0 & \frac{1}{L} & \frac{-1}{L} \\ \frac{-1}{C_1} & \frac{-1}{C_1 R_{\text{battery}}} & 0 \\ \frac{1}{C_2} & 0 & \frac{-1}{C_2 R_{\text{load}}} \end{bmatrix} \begin{bmatrix} i_L \\ v_{\text{T1}} \\ v_{\text{dc-link}} \end{bmatrix} + \begin{bmatrix} 0 \\ \frac{1}{C_1 R_{\text{battery}}} \\ 0 \end{bmatrix} v_{\text{battery}} \tag{3.10}$$

Figure 3.8 shows a schematic diagram of the boost dc-dc converter in the third time-interval. In this time-interval the diode (D_2) and switch (S_1) are both off. Thus the inductor current (i_L) in this time-interval equals zero. Equation (3.11) shows the state equations of the dc-dc converter in this time interval.

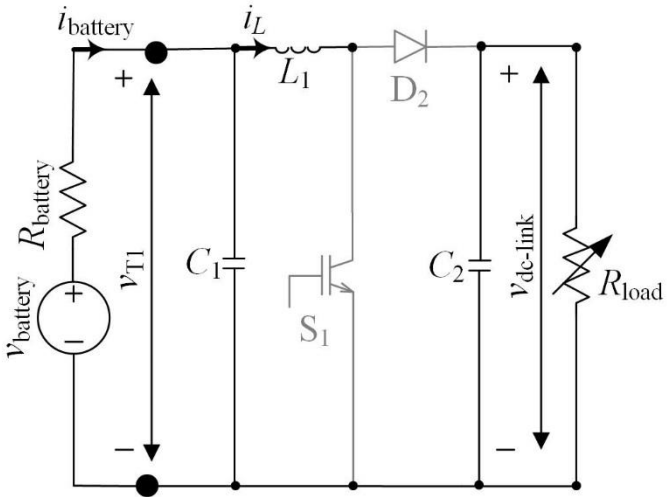

Figure 3.8: A boost dc-dc converter in time interval 3

$(d_1 + d_2)T_S < t < T_S$:

$$\frac{d}{dt}\begin{bmatrix} i_L \\ v_{T1} \\ v_{dclink} \end{bmatrix} = \begin{bmatrix} 0 & 0 & 0 \\ 0 & \dfrac{-1}{C_1 R_{battery}} & 0 \\ 0 & 0 & \dfrac{-1}{C_2 R_{load}} \end{bmatrix} \begin{bmatrix} i_L \\ v_{T1} \\ v_{dc\text{-}link} \end{bmatrix} + \begin{bmatrix} 0 \\ \dfrac{1}{C_1 R_{battery}} \\ 0 \end{bmatrix} v_{battery} \tag{3.11}$$

$$\frac{d}{dt}\begin{bmatrix} \bar{i}_L \\ \bar{v}_{T1} \\ \bar{v}_{dc\text{-}link} \end{bmatrix} = \begin{bmatrix} 0 & \dfrac{d_1 + d_2}{L} & \dfrac{-d_2}{L} \\ \dfrac{-(d_1 + d_2)}{C_1} & \dfrac{-1}{C_1 R_{battery}} & 0 \\ \dfrac{d_2}{C_2} & 0 & \dfrac{-1}{C_2 R_{load}} \end{bmatrix} \begin{bmatrix} \bar{i}_L \\ \bar{v}_{T1} \\ \bar{v}_{dc\text{-}link} \end{bmatrix} + \begin{bmatrix} 0 \\ \dfrac{1}{C_1 R_{battery}} \\ 0 \end{bmatrix} v_{battery} \tag{3.12}$$

Equation (3.12) shows a weighted average of (3.9)-(3.11) over the switching period (T_s). Equation (3.15) shows the modified state space averaged-value model for the boost converter by taking the required modification mentioned in section 3.2.1 into consideration.

Equation (3.13) shows the average inductor current in a boost converter (see Figure 3.5). Equation (3.14) shows the calculated averaged inductor current using the state space averaging method.

$$\bar{i}_L = \frac{i_{\text{pk}}(d_1 + d_2)}{2} \tag{3.13}$$

$$\bar{i}_L = \bar{d}.\bar{i}_L = (d_1 + d_2)\frac{i_{pk}(d_1 + d_2)}{2} \tag{3.14}$$

$$\frac{d}{dt}\begin{bmatrix} \bar{i}_L \\ \bar{v}_{\text{T1}} \\ \bar{v}_{\text{dc-link}} \end{bmatrix} = \begin{bmatrix} 0 & \frac{d_1 + d_2}{L} & \frac{-d_2}{L} \\ \frac{-1}{C_1} & \frac{-1}{C_1 R_{\text{battery}}} & 0 \\ \frac{d_2}{C_2(d_1 + d_2)} & 0 & \frac{-1}{C_2 R_{\text{load}}} \end{bmatrix}\begin{bmatrix} \bar{i}_L \\ \bar{v}_{\text{T1}} \\ \bar{v}_{\text{dc-link}} \end{bmatrix} + \begin{bmatrix} 0 \\ \frac{1}{C_1 R_{\text{battery}}} \\ 0 \end{bmatrix} v_{\text{battery}} \tag{3.15}$$

3.2.2.1 Full-order model

Equation (3.16) shows the averaged-value inductor current in terms of the maximum inductor current (i_{pk}), and the duration of the first and the second time interval (d_1, d_2) shown in Figure 3.5. Equation (3.17) indicates the maximum inductor current in terms of dc-dc converter input terminal voltage (v_{T1}), duration of the first time interval (d_1), and the inductor value (L). Combination of (3.16) and (3.17) yields (3.18). Equation (3.18) relates the duration of the first and the second time intervals (d_2, d_1) in a boost dc-dc converter.

$$\bar{i}_L = \frac{i_{\text{pk}}(d_1 + d_2)}{2} \tag{3.16}$$

$$i_{\text{pk}} = \frac{v_{\text{T1}} d_1 T_s}{L} \tag{3.17}$$

$$d_2 = \frac{2L\bar{i}_L}{d_1 T_s v_{T1}} - d_1 \tag{3.18}$$

By replacing d_2 from (3.18) in (3.15), (3.15) is no longer dependent on d_2. Therefore, after simplification, equations (3.19)-(3.21) will show the dc-dc converter's state equations. These equations are known as the full-order model of a dc-dc converter in the literature [68].

$$\frac{d\bar{i}_L}{dt} = \frac{2\bar{i}_L}{d_1 T_{\text{S}}}\left(1 - \frac{\bar{v}_{\text{dc-link}}}{\bar{v}_{\text{T1}}}\right) + \frac{d_1 \bar{v}_{\text{dc-link}}}{L} \tag{3.19}$$

$$\frac{d\bar{v}_{\text{dc-link}}}{dt} = \frac{\bar{i}_L}{C_2} - \frac{d_1^2 T_{\text{S}} \bar{v}_{\text{T1}}}{2LC_2} - \frac{\bar{v}_{\text{dc-link}}}{R_{\text{load}} C_2} \tag{3.20}$$

$$\frac{d\bar{v}_{\text{T1}}}{dt} = -\frac{\bar{i}_L}{C_1} - \frac{\bar{v}_{\text{T1}}}{R_{\text{battery}} C_1} + \frac{v_{\text{battery}}}{R_{\text{load}} C_2} \tag{3.21}$$

3.2.2.2 Reduced-order model

Equations (3.22) and (3.23) show the relation between the maximum inductor current and the inductor voltage for the first and the second time-intervals (d_1, d_2). Equation (3.24) is derived by combining (3.22) and (3.23). Equation (3.24) present d_2 in terms of d_1. Therefore, d_2 is eliminated in (3.25)-(3.27) by replacing (3.24) in (3.15). Equations (3.25)-(3.27) show the reduced-order model of the dc-dc converter [68].

$$i_{\text{pk}} = \frac{v_{\text{T1}}}{L} d_1 T_{\text{S}} \tag{3.22}$$

$$i_{\text{pk}} = \frac{v_{\text{dc-link}} - v_{\text{T1}}}{L} d_2 T_S \tag{3.23}$$

$$d_2 = \frac{v_{\text{T1}}}{v_{\text{dc-link}} - v_{\text{T1}}} d_1 \tag{3.24}$$

$$\frac{d\bar{i}_L}{dt} = 0 \tag{3.25}$$

$$\frac{d\bar{v}_{\text{dc-link}}}{dt} = \frac{v_{\text{T1}}\bar{i}_L}{v_{\text{dc-link}}C_2} - \frac{v_c}{R_{\text{load}}C_2} \tag{3.26}$$

$$\frac{d\bar{v}_{\text{T1}}}{dt} = -\frac{\bar{i}_L}{C_1} - \frac{\bar{v}_{\text{T1}}}{R_{\text{battery}}C_1} + \frac{v_{\text{battery}}}{R_{\text{load}}C_2} \tag{3.27}$$

Equation (3.28) is derived by replacing (3.22) and (3.24) in (3.16). Equation (3.28) shows the averaged inductor current in a boost converter. This may be used to further simplify (3.26). Equation (3.29) is derived by replacing averaged inductor current (i_L) in (3.26). (3.29) will be used in Chapter 5 to tune the feed-forward control system for a BESS.

$$\bar{i}_L = \frac{v_{\text{T1}}}{2L} d_1^2 T_{\text{s}} \left(\frac{v_{\text{dc-link}}}{v_{\text{dc-link}} - v_{\text{T1}}}\right) \tag{3.28}$$

$$\frac{d\bar{v}_{\text{dc-link}}}{dt} = \frac{d_1^2 v_{\text{T1}}^2 T_{\text{s}}}{2LC_2(v_{\text{dc-link}} - v_{\text{T1}})} - \frac{v_{\text{dc-link}}}{R_{\text{load}}C_2} \tag{3.29}$$

3.2.3 Buck dc-dc converter

Figure 3.9 shows a dc-dc converter in the buck operating mode. In this mode of operation the flow of power is from right to left in Figure 3.9 (to charge the battery). Without loss of generality, a resistor (R_L) is placed on the dc-link in Figure 3.9. Since the power flows from the load side (dc-link side) to the battery in this mode of operation, the value of this resistor is negative. This means that the load generates power rather than consuming it. Using a negative

resistive load in the analysis of the buck converter instead of a voltage source helps to obtain similar (in nature) equations to those of the boost converter.

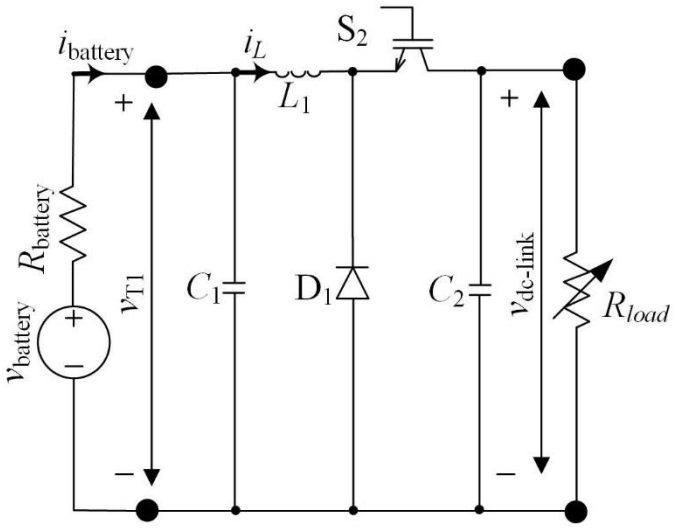

Figure 3.9: A buck dc-dc converter

Similar to a boost converter, a buck converter is analysed in discontinuous conduction mode. Figure 3.10 shows the inductor current in a buck converter in discontinuous mode. Three time intervals are defined on the figure. In the first time-interval, the switch (S_2) conducts and the diode (D_1) is off. This results in a decrease in the inductor current (i_L). Figure 3.11 shows the schematic diagram of a buck converter in the first time interval. Equation (3.30) shows the state equation of the buck converter in the first time interval.

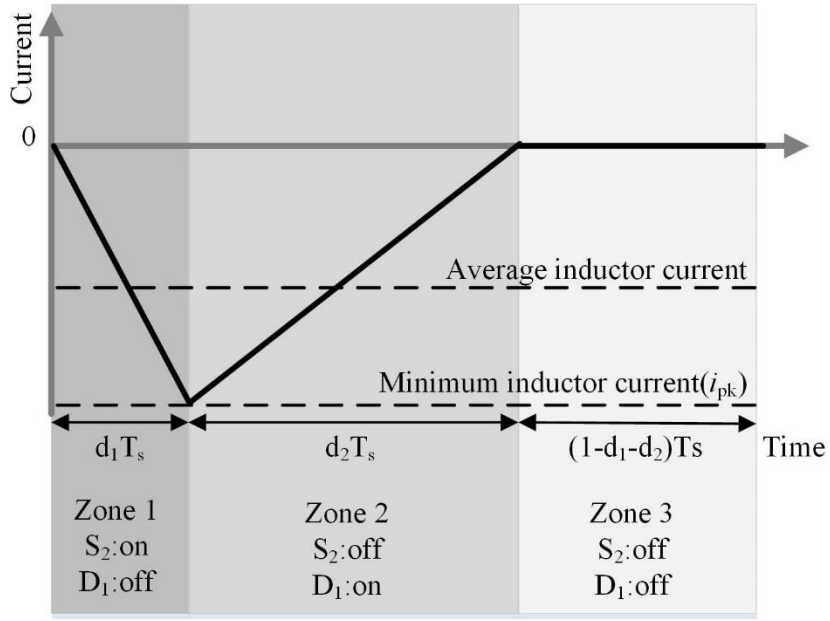

Figure 3.10: Buck inductor current in DCM

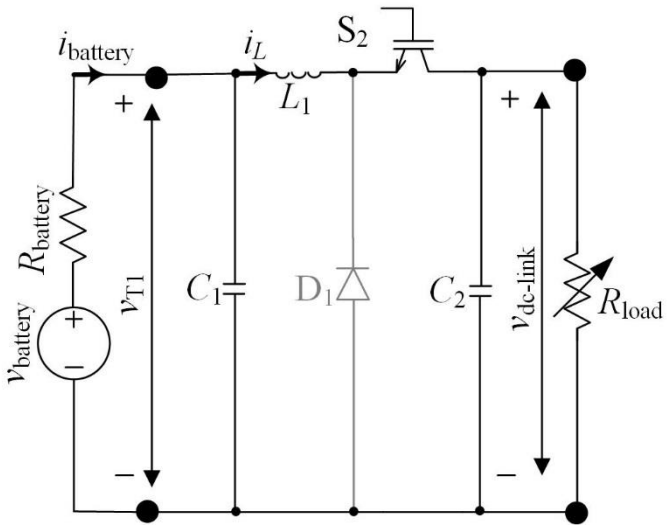

Figure 3.11: A buck dc-dc converter in time interval 1

$$0 < t < d_1 T_S :$$

$$\frac{d}{dt}\begin{bmatrix} i_L \\ v_{T1} \\ v_{dclink} \end{bmatrix} = \begin{bmatrix} 0 & \frac{1}{L} & \frac{-1}{L} \\ \frac{-1}{C_1} & \frac{-1}{C_1 R_{battery}} & 0 \\ \frac{1}{C_2} & 0 & \frac{-1}{C_2 R_{load}} \end{bmatrix} \begin{bmatrix} i_L \\ v_{T1} \\ v_{dc\text{-}link} \end{bmatrix} + \begin{bmatrix} 0 \\ \frac{1}{C_1 R_{battery}} \\ 0 \end{bmatrix} v_{battery} \tag{3.30}$$

Figure 3.12 shows schematic diagram of the buck converter in the second time interval. In the second time interval, the diode (D_1) conducts and the switch (S_2) is off. Thus, the inductor current (i_L) increases. Equation (3.31) shows states equations of the buck converter in the second time interval.

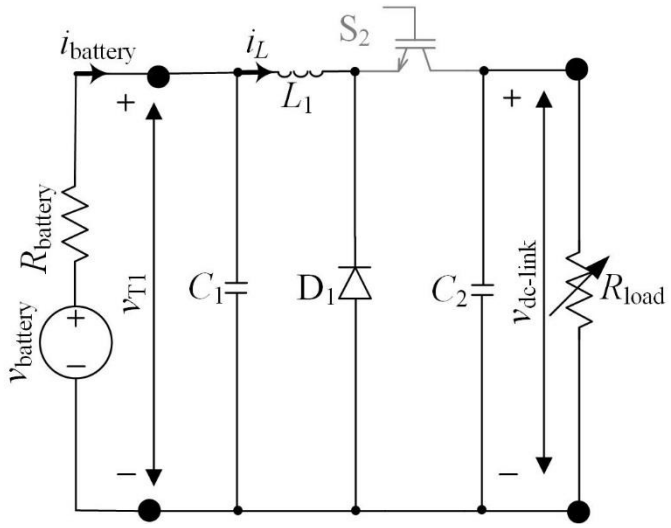

Figure 3.12: A buck dc-dc converter in time interval 2

$$d_1T_s < t < (d_1 + d_2)T_s :$$

$$\frac{d}{dt}\begin{bmatrix} i_L \\ v_{T1} \\ v_{dc\text{-}link} \end{bmatrix} = \begin{bmatrix} 0 & \frac{1}{L} & 0 \\ \frac{-1}{C_1} & \frac{-1}{C_1 R_{battery}} & 0 \\ 0 & 0 & \frac{-1}{C_2 R_{load}} \end{bmatrix} \begin{bmatrix} i_L \\ v_{T1} \\ v_{dc\text{-}link} \end{bmatrix} + \begin{bmatrix} 0 \\ \frac{1}{C_1 R_{battery}} \\ 0 \end{bmatrix} v_{battery} \quad (3.31)$$

Figure 3.13 shows schematic diagram of a buck converter in the third time interval. In this time interval, the diode (D_1) and the switch (S_2) are both off. Equation (3.32) shows the state equation of the buck converter in the third time interval.

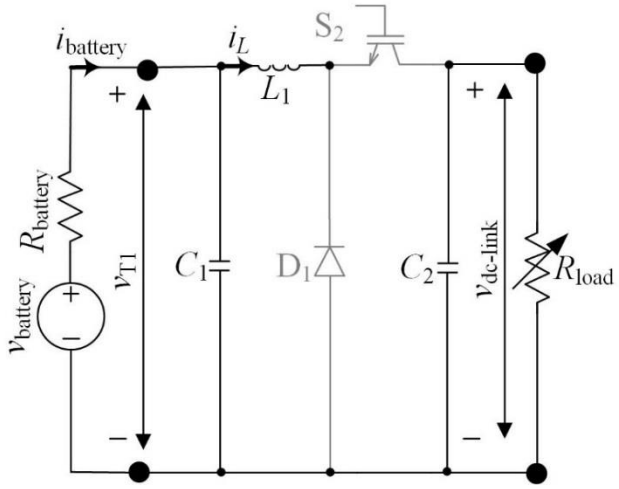

Figure 3.13: A buck dc-dc converter in time interval 3

$$(d_1 + d_2)T_S < t < T_S :$$

$$\frac{d}{dt}\begin{bmatrix} i_L \\ v_{T1} \\ v_{dc\text{-}link} \end{bmatrix} = \begin{bmatrix} 0 & 0 & 0 \\ 0 & \dfrac{-1}{C_1 R_{battery}} & 0 \\ 0 & 0 & \dfrac{-1}{C_2 R_{load}} \end{bmatrix} \begin{bmatrix} i_L \\ v_{T1} \\ v_{dc\text{-}link} \end{bmatrix} + \begin{bmatrix} 0 \\ \dfrac{1}{C_1 R_{battery}} \\ 0 \end{bmatrix} v_{battery} \tag{3.32}$$

Equation (3.33) shows the state space average of equations (3.27)-(3.30). As discussed in the previous subsection, since the converter is operating in DCM, the state space averaging method needs to be modified for the inductor current (i_L). Equation (3.34) shows the modified state space average model for the buck dc-dc converter as explained in section 3.2.1.

$$\frac{d}{dt}\begin{bmatrix} \bar{i}_L \\ \bar{v}_{T1} \\ \bar{v}_{dc\text{-}link} \end{bmatrix} = \begin{bmatrix} 0 & \dfrac{d_1 + d_2}{L} & \dfrac{-d_1}{L} \\ \dfrac{-(d_1 + d_2)}{C_1} & \dfrac{-1}{C_1 R_{battery}} & 0 \\ \dfrac{d_1}{C_2} & 0 & \dfrac{-1}{C_2 R_{load}} \end{bmatrix} \begin{bmatrix} \bar{i}_L \\ \bar{v}_{T1} \\ \bar{v}_{dclink} \end{bmatrix} + \begin{bmatrix} 0 \\ \dfrac{1}{C_1 R_{battery}} \\ 0 \end{bmatrix} v_{battery} \tag{3.33}$$

$$\frac{d}{dt}\begin{bmatrix} \bar{i}_L \\ \bar{v}_{T1} \\ \bar{v}_{dc\text{-}link} \end{bmatrix} = \begin{bmatrix} 0 & \dfrac{d_1 + d_2}{L} & \dfrac{-d_1}{L} \\ \dfrac{-1}{C_1} & \dfrac{-1}{C_1 R_{battery}} & 0 \\ \dfrac{d_1}{C_2(d_1 + d_2)} & 0 & \dfrac{-1}{C_2 R_{load}} \end{bmatrix} \begin{bmatrix} \bar{i}_L \\ \bar{v}_{T1} \\ \bar{v}_{dc\text{-}link} \end{bmatrix} + \begin{bmatrix} 0 \\ \dfrac{1}{C_1 R_{battery}} \\ 0 \end{bmatrix} v_{battery} \tag{3.34}$$

3.2.3.1 Full order model

Equation (3.35) shows the averaged inductor current (i_L) during a switching period. Equation (3.36) shows the minimum inductor current (i_{pk}) in terms of converter parameters. Equations (3.35) and (3.36) are combined to form (3.37).

$$\bar{i}_L = \frac{i_{\text{pk}}(d_1 + d_2)}{2} \tag{3.35}$$

$$i_{\text{pk}} = \frac{(v_{\text{T1}} - v_{\text{dc-link}})d_1 T_{\text{s}}}{L} \tag{3.36}$$

$$d_2 = \frac{2L\bar{i}_L}{d_1 T_{\text{s}}(v_{\text{T1}} - v_{\text{dc-link}})} - d_1 \tag{3.37}$$

Replacement for d_2 from (3.37) in (3.34) yields (3.38)-(3.40). These equations show the buck converter's full-order averaged-value model.

$$\frac{d\bar{i}_L}{dt} = \frac{2\bar{i}_L}{(v_{T1} - v_{\text{dc-link}})d_1 T_{\text{s}}} v_{\text{T1}} - \frac{d_1 \bar{v}_{\text{dc-link}}}{L} \tag{3.38}$$

$$\frac{d\bar{v}_{\text{dc-link}}}{dt} = \frac{d_1^2 T_{\text{s}}(\bar{v}_{\text{T1}} - v_{dclink})}{2LC_2} - \frac{\bar{v}_{\text{dc-link}}}{R_{\text{load}} C_2} \tag{3.39}$$

$$\frac{d\bar{v}_{\text{T1}}}{dt} = -\frac{\bar{i}_L}{C_1} - \frac{\bar{v}_{\text{T1}}}{R_{\text{battery}} C_1} + \frac{v_{\text{battery}}}{R_{\text{load}} C_2} \tag{3.40}$$

3.2.3.2 Reduced-order model

Equation (3.37) is not the only algebraic equation that relates d_1 and d_2. Equations (3.41) and (3.42) show two equations that describe the minimum inductor current (i_{pk}). Combination of (3.41) and (3.42) yields (3.43). This equation relates d_1 and d_2.

$$i_{\text{pk}} = \frac{v_{\text{T1}} - v_{\text{dc-link}}}{L} d_1 T_{\text{s}} \tag{3.41}$$

$$i_{\text{pk}} = \frac{-v_{\text{T1}}}{L} d_2 T_{\text{s}} \tag{3.42}$$

$$d_2 = \frac{v_{\text{T1}}}{v_{\text{dc-link}} - v_{\text{T1}}} d_1 \tag{3.43}$$

Replacement for d_2 from (3.43) in (3.34) yields (3.44)-(3.46). These equations are known as the buck converter's reduced-order model.

$$\frac{d\bar{i}_L}{dt} = 0 \tag{3.44}$$

$$\frac{d\bar{v}_{\text{dc-link}}}{dt} = \frac{v_{\text{T1}} i_L}{v_{\text{dc-link}} C_2} - \frac{v_{\text{dc-link}}}{R_{\text{load}} C_2} \tag{3.45}$$

$$\frac{d\bar{v}_{\text{T1}}}{dt} = -\frac{\bar{i}_L}{C_1} - \frac{\bar{v}_{\text{T1}}}{R_{\text{battery}} C_1} + \frac{v_{\text{battery}}}{R_{\text{load}} C_2} \tag{3.46}$$

Equation (3.47) is derived by replacing (3.41) and (3.43) in (3.35). Equation (3.47) shows the average inductor current in a buck converter. Replacement for the average inductor current in (3.45) from (3.47) results in (3.48). Equation (3.48) will be used in Chapter 5 to tune the feed-forward control system for a BESS.

$$\bar{i}_L = \frac{v_{\text{dc-link}}}{2L} d_1^2 T_{\text{s}} \left(\frac{v_{\text{T1}} - v_{\text{dc-link}}}{v_{\text{T1}}} \right) \tag{3.47}$$

$$\frac{d\bar{v}_{\text{dclink}}}{dt} = \frac{(v_{\text{in}} - v_{\text{dclink}}) d_1^2 T_{\text{s}}}{2LC_2} - \frac{v_{\text{dclink}}}{R_{\text{load}} C_2} \tag{3.48}$$

3.2.4 Comparing dc-dc converter models

Figure 3.14 (a) and (b) show comparison of the predicted dc-link voltage by the full-order and reduced-order models against prediction of a detailed model in PSCAD/EMTDC for different frequencies. The values for the full-order model shown in Fig. 3.14 (a) are derived by solving (3.19) and (3.20) for $v_{\text{dc-link}}$. The values for the reduced-order model shown in Fig. 3.14 (b) are derived by solving (3.29) for $v_{\text{dc-link}}$. As shown both models have excellent accuracy in prediction of the dc-link voltage. Figure 3.14 is shown for a boost converter. Table 3.1 shows the specifications of the boost converter.

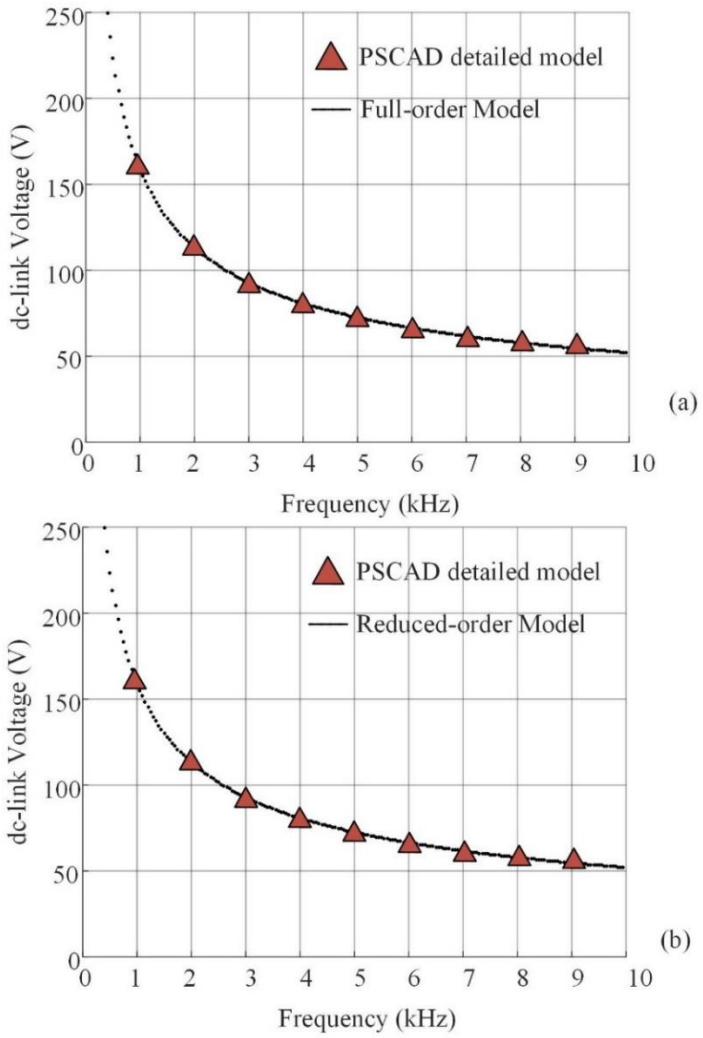

Figure 3.14: Comparison of dc-dc converter models against a detailed model in PSCAD: (a) full-order and (b) reduced-order models

Table 3.1: Boost converter specifications

L_1 (μH)	D_1	C (μF)	R_{load} (Ω)	V_{T1} (V)
5	0.7	40	20	5

3.3 Voltage source converter modeling

The principles of operation and the control system of a VSC were discussed earlier in Chapter 2. This section presents a VSC model for the purpose of BESS modeling. In dynamic averaged-value modeling, the high-frequency switching of a VSC is neglected and the low-frequency contents are retained. Equations (3.49)-(3.51) show an averaged-value model of the VSC. This model is widely used in the literature [69], [70].

$$v_a = 0.5 m v_{\text{dc-link}} \cos(\theta_c) \tag{3.49}$$

$$v_b = 0.5 m v_{\text{dc-link}} \cos(\theta_c - \frac{2\pi}{3}) \tag{3.50}$$

$$v_c = 0.5 m v_{\text{dc-link}} \cos(\theta_c + \frac{2\pi}{3}) \tag{3.51}$$

These equations describe the fundamental-frequency output voltage of VSC as a function of the dc-link voltage ($v_{\text{dc-link}}$), the modulation index (m), and converter phase angle (θ_c). The phase angle of the converter voltage (θ_c) may lead (discharging mode) or lag (charging mode) the phase angle of the point of common coupling (the reference angle in this study). The phase angle of the PCC is assumed to be zero (reference in this thesis).

Equation (3.52) shows the VSC phase voltages in the dq0 domain. Park's transformation was used to transform the phase voltages from the abc domain to the dq0 domain. Park's transform

was presented in (2.6). The phase angle of PCC is tracked by a phase-locked loop (PLL) in a BESS.

$$\begin{bmatrix} v_q \\ v_d \\ v_0 \end{bmatrix} = 0.5 m v_{\text{dc-link}} \begin{bmatrix} \cos(\theta_c) \\ -\sin(\theta_c) \\ 0 \end{bmatrix} \tag{3.52}$$

Figure 3.15 shows the schematic diagram of the averaged model of the VSC. The exchanged real power between the VSC and the terminating ac system (P_{VSC}) is calculated as in (3.53). In this equation i_d and i_q are the d and q components of ac current. Equation (3.54) shows the exchanged power between the VSC and dc-dc converter ($P_{\text{converter}}$). Assuming a lossless VSC, to maintain the voltage of the dc-link the exchanged real power of the VSC must be compensated by the dc-dc converter. This results in (3.55). The value of the i_{dc} is either positive (discharging) or negative (charging) depending on the direction of the power exchange with the grid.

$$P_{\text{VSC}} = \frac{3}{2}(i_d v_d + i_q v_q) \tag{3.53}$$

$$P_{\text{converter}} = v_{\text{dc-link}} i_{\text{dc}} \tag{3.54}$$

$$i_{\text{dc}} = \frac{3}{4} m(\cos(\phi) i_q - \sin(\phi) i_d) \tag{3.55}$$

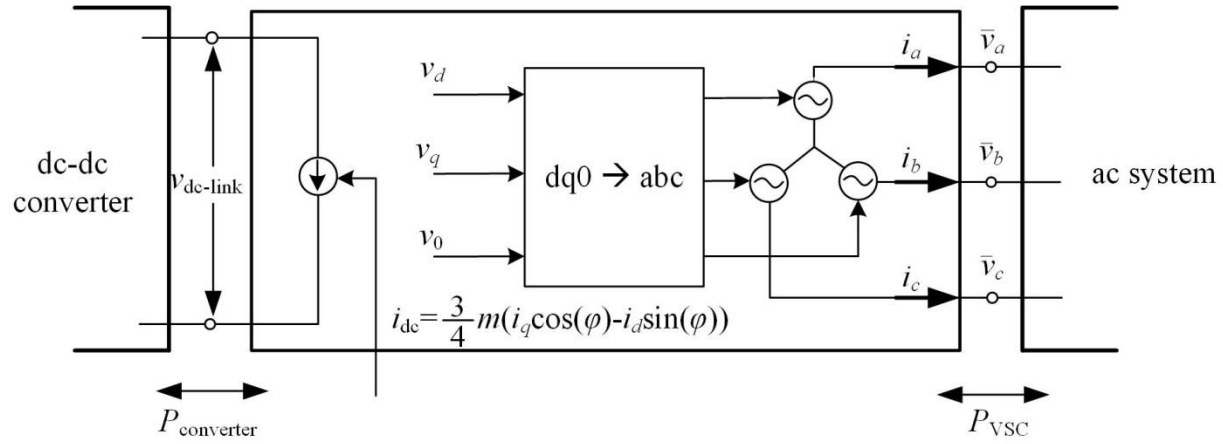

Figure 3.15: Schematic diagram of an averaged VSC model

A VSC connected to a dc-dc converter is essentially a variable load for the dc-dc converter as is shown in (3.56). Since both the voltage and current of this current source are dc, it is concluded that the VSC and its terminating system can be represented as a variable resistive load for the dc-dc converter as in Figure 3.16.

$$R_{load}=\frac{4\bar{v}_{dclink}}{3m(\cos(\phi)i_q-\sin(\phi)i_d)} \tag{3.56}$$

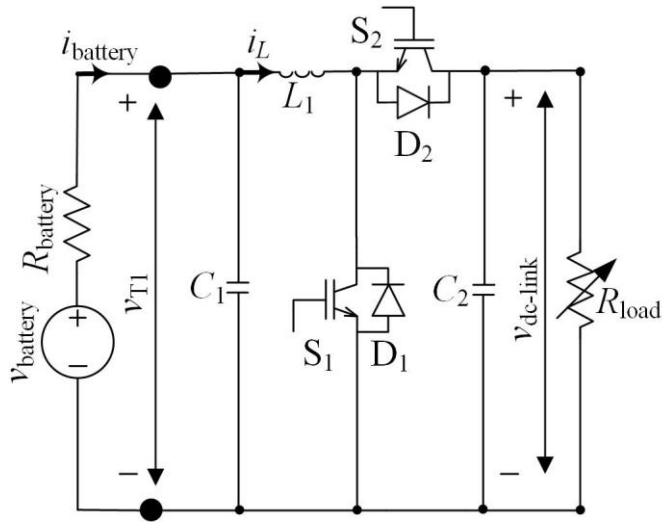

Figure 3.16: A dc-dc converter with variable resistive load

3.3.1 Comparing VSC models

This section compares the averaged VSC model described in the last section to a VSC detailed model in an electromagnetic transient simulation software (PSCAD/EMTDC). Figure 3.17 compares the VSC's dc-link current of the averaged model (in (3.56)) and the detailed model. As is seen in Figure 3.17, the impact of high frequency switching is visible in the VSC's detailed model and is filtered in the averaged VSC model.

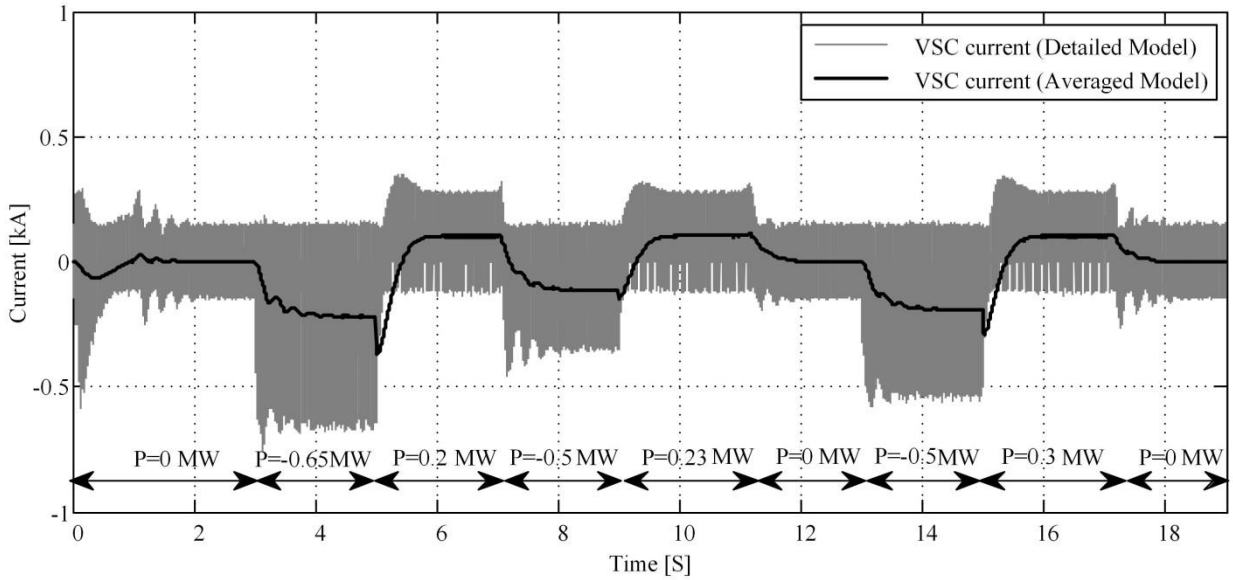

Figure 3.17: Comparing VSC dc-link averaged current

3.4 BESS modeling

Section 2 of this chapter discussed averaged models of the boost and the buck dc-dc converters. Section 3 of this chapter also discussed that a converter connected VSC may be represented as a varying resistive load. Thus, considering a variant resistive load, equations (3.19)-(3.21) and (3.38)-(3.40) describe a BESS in discharge and charge modes respectively. In these equations three state variables exist. Since a PI controller is usually used to control a dc-dc converter (see

Figure 2.8) an extra state equation needs to be added to the system equations. Equations (3.57) and (3.58) describe a general format of a PI controller for the dc-dc converter with k_i and k_p parameters as the integrator and proportional gains, respectively. x presents the forth state variable of the descriptive equations. Thus by replacement for d_1 from (3.58) in (3.19)-(3.21) and (3.38)-(3.40) and (3.57) results in two sets of four nonlinear state equations that describe the BESS in the boost and the buck modes, respectively.

$$\frac{dx}{dt} = \text{error } (e) = v_{\text{dclink-ref}} - v_{\text{dc-link}} \tag{3.57}$$

$$d_1 = k_p (v_{\text{dclink-ref}} - v_{\text{dc-link}}) + k_i x \tag{3.58}$$

3.5 Chapter Summary and contributions

The BESS components were individually modeled in this chapter using averaged-value modeling technique. Two dc-dc converter models were developed and compared against each other. Although these models were introduced previously in the literature, these models were used to model a BESS in this thesis. In addition, a variable resistor was proposed and evaluated as a VSC averaged-value model in this thesis. Afterwards, a set of non-linear equations were introduced as the BESS descriptive equations. These equation will be later used in the next chapter to study the stability and the dynamics of the BESS. A detailed model of the BESS (including detailed model of each component) was developed in PSCAD/EMTDC to carry out simulations and evaluate the accuracy of the averaged-value models.

Chapter 4 Stability Analysis

This chapter discusses the stability of the BESS, defines a stability region for the BESS, and introduces an approach to ensure that the BESS operate in a stable region. Stability of a BESS is important due to the fact that grid-connected energy storage systems are required to absorb or deliver power as scheduled. A failure in delivery or absorption of power in a part of the grid could cause an imbalance in the power supply and demand and may eventually cause instability in power systems.

4.1 Stability analysis

A BESS was modeled in the previous chapter. As was shown, two sets of four non-linear state equations present a BESS in discharge (boost) and charge (buck) modes. This chapter analyses the stability of the BESS using the developed set of equations in the previous chapter.

The internal resistance of the battery bank (R_{battery}) and the voltage of the battery bank (v_{battery}) appear in the system equations. These two parameters are proportional to the battery cell voltage and the battery cell resistance as was discussed in Section 3.1.1. The battery cell voltage and the battery cell resistance are commonly used in battery applications to monitor the status of battery cells as will be discussed in the next two paragraphs. Thus, the effect of a change in the battery bank voltage and the battery bank resistance is analysed in this study.

The battery bank's SoC is continuously monitored by a BMS during operation of the BESS. The battery bank voltage changes during BESS operation as the battery cells SoC changes. The battery model described in Section 3.1 shows the relation between the SoC and the battery cell voltage (see Section 3.1.1 for relation between battery cell voltage and battery bank voltage).

The internal resistance of the battery bank increases as the battery cells degrade. The battery cell's internal resistance might increase up to 300 percent as the battery cell degrades [50]. The battery cell's internal resistance may also be measured to determine the cell's state of health during the life cycle of the battery cell (see Section 3.1.1 for the relationship between battery cell resistance and battery bank resistance).

In this section, two methods are used to study BESS stability on a battery resistance-battery voltage plane. The battery resistance-battery voltage plane is introduced in Figure 4.1. The x-axis of this plane shows the battery bank's voltage and the y-axis shows the battery bank's internal resistance.

Since the battery bank voltage of the BESS alters (increases and decreases depending on battery cell's SoC in each cycle) and the internal resistance of the battery bank increases during the life cycle of the BESS, an operating region is defined for the BESS on the battery resistance-battery voltage plane. The operating region is shown as a rectangle in Figure 4.1. The battery resistance-battery voltage plane in Figure 4.1 is divided into stable and unstable regions. Figure 4.1 also shows the numerical boundary, stability parabola, approximated stability line, and the PSCAD verified point. These will be discussed individually in Sections 4.1.1- 4.1.3 and 4.2. As will be shown in this chapter, in the unstable region no solution exists for the system's state space equations. BESS detailed simulation in PSCAD/EMTDC shows that in unstable region the duty cycle of the dc-dc converter tends to increase without bound to maintain system's power output. Since the duty cycle is limited to 1 in a real system, the power output of the system and the voltage of the dc-link in the BESS drop to zero. The interpretation of the phenomena is as follows. The VSC tends to export power from the dc-link but the dc-dc converter is incapable of providing the required power to the dc-link due to low battery bank voltage or high battery bank

resistance. This causes a dc-link voltage drop. In this circumstance, the BESS will not be able to follow the real and reactive power set-point command and may cause an imbalance of power supply and demand in the grid. Hence, it is important to determine the stability boundary and take the required countermeasures to ensure that the BESS operates in the stable region on the battery voltage-battery resistance plane.

4.1.1 Stability parabola

Equations (4.1) and (4.2) relate the dc-dc converter power, equivalent battery bank's internal resistance, and the battery bank's voltage (see Figure 3.16). Assuming a loss-less dc-dc converter and VSC, the dc-dc converter's input power equals the VSC's output power (see BESS structure in Section 2.1). Hence, the VSC power could be replaced for dc-dc converter power in formulations expressed below. Replacing for the dc-dc converter terminal voltage (v_{T1}) from (4.2) in (4.1) and solving it for the inductor current (i_L) yields equation (4.3).

$$v_{T1} = v_{battery} - R_{battery} i_L \tag{4.1}$$

$$P_{converter} = v_{T1} i_L \tag{4.2}$$

$$i_L = \frac{v_{battery} \pm \sqrt{v_{battery}^2 - 4P_{converter}R_{battery}}}{2R_{battery}} \tag{4.3}$$

In a boost converter, where $P_{converter} > 0$, in order for the inductor current (i_L) to be a real value one must ensure that $v_{battery}^2 > 4P_{converter}R_{battery}$. Hence, the parabola given by equation (4.4) determines the static stability limit of the converter operation and is denoted as the stability parabola in Figure 4.1.

$$v_{battery}^2 = 4P_{converter}R_{battery} \tag{4.4}$$

In a buck converter, where $P_{converter} < 0$, $v_{battery}^2 - 4P_{converter}R_{battery}$ is always positive. Consequently, no stability margin is defined for the buck converter. Besides, EMT simulations of a detailed BESS in PSCAD/EMTDC do not show instability of this nature in any areas on the battery resistance-battery voltage plane.

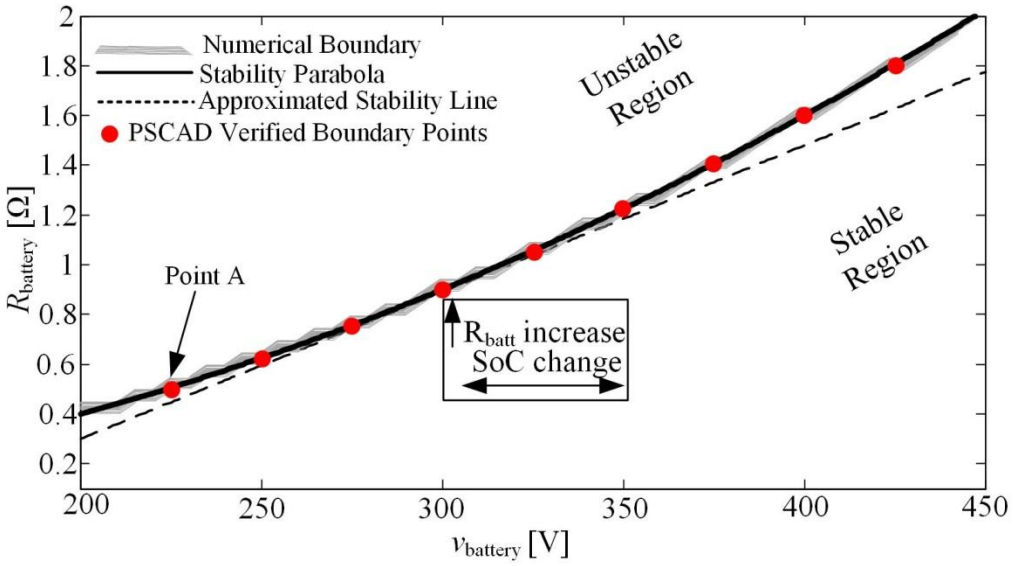

Figure 4.1: Converter stability region on the $R_{battery}$-$v_{battery}$ plane for a 25-kW rated converter.

4.1.2 PSCAD verification of the stability boundary

The stability parabola in Figure 4.1 has been verified by EMT simulations of a detailed BESS model in PSCAD/EMTDC. PSCAD-verified boundary points in Figure 4.1 represent simulation cases in which an increase in the internal battery bank resistance ($R_{battery}$) or a decrease in the battery bank's cell voltage ($v_{battery}$) causes instability. Hence, the initial operating point of the simulation cases is intentionally selected to be close to the boundary of the stable region. Table 4.1 shows specifications of point A in Figure 4.1 as an example.

Table 4.1: Point A specifications (25-kW rated converter).

I_L (A)	$\bar{v}_{\text{dc-link}}$ (V)	v_{in} (V)	x	R_{battery} (Ω)	v_{battery} (V)
188.5	600	132	78	0.49	225

Figures 4.2(a) and (b) show the state trajectories (v_{in} and $v_{\text{dc-link}}$) of the system due to a small change in R_{battery} and v_{battery}. Figure 4.2(a) shows the stable trajectories in response to a small -5% decrease in R_{battery} or a +5% increase in v_{battery}. Figure 4.2(b) shows state trajectories in response to a +5% increase in R_{battery} and a -5% decrease in v_{battery}. These latter trajectories clearly show instability as the states collapse to zero. A small ±5% change in the values of the R_{battery} and v_{battery} for this operating point (point A) may cause instability of the system depending on the direction of the change on the R_{battery}-v_{battery} plane (see figure 4.1). To further verify this, Figures 4.2 (c) and (d) show the time-domain response of the system to the same changes as in Figures 4.2(a) and (b), respectively. Changes in system's parameters in Figure 4.2 (c) has moved point A inside the stable region. Thus, the dc-link voltage is retained despite the system's parameter change. In contrast, in Figure 4.2 (d), point A is moved inside unstable region which has caused collapse of the dc-link voltage. Equations (3.19)-(3.21), (3.57), and (3.58) are solved to obtain the state trajectories shown in Fig. 4.2.

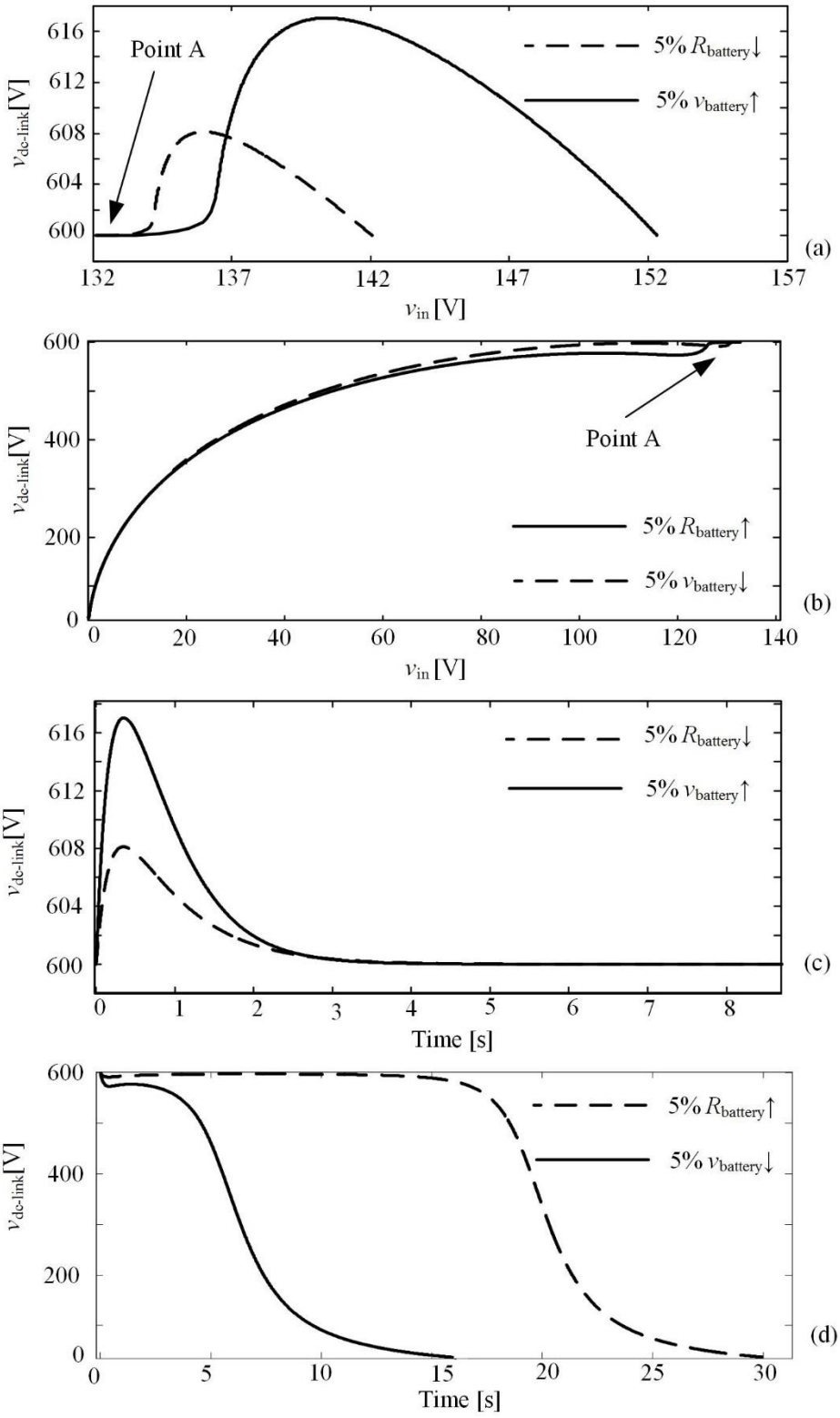

Figure 4.2:(a) Stable state trajectories, (b) unstable state trajectories, (c) stable time domain traces, (d) unstable time-domain traces of the system due to changes in the $R_{battery}$ and $v_{battery}$ in a 25-kW rated converter.

4.1.3 Numerical stability boundary

The operating point (equilibrium point) of the system can be obtained by solving the non-linear set of equations (3.19)-(3.21), (3.57), and (3.58) for the boost converter with the state derivatives set to zero. This results in the expressions shown below. Equations (4.5) and (4.6) are related to the operating point of the dc-dc converter. Equations (4.7) and (4.8) refer to the battery and the controller operating conditions, respectively.

$$M = \frac{V_{\text{dc-link}}}{V_{\text{T1}}} = \frac{1}{2} + \frac{1}{2}\sqrt{1 + \frac{2D_1^2 R_{\text{load}}}{L_1 f_s}} \tag{4.5}$$

$$I_L = \frac{D_1^2 V_{T1} M}{2L_1 f_s (M-1)} \tag{4.6}$$

$$V_{\text{T1}} = V_{\text{battery}} - R_{\text{battery}} I_L \tag{4.7}$$

$$V_{\text{dc-link}} = V_{\text{dclink–ref}} \tag{4.8}$$

In order to determine the states of the system in a stable operating point, i.e., V_{dclink}, V_{in}, I_L, and $D = k_i.x$, equations (4.5)-(4.8) must be solved simultaneously. The boundary of stability calculated using solution of equations (4.5)-(4.8) is referred to as the numerical boundary in Fig. 4.1. It is noted that in the unstable region, the state variables have either an imaginary or a negative value, both of which are considered as infeasible. Thus in the unstable region no feasible op**e**rating point exists.

Stability parabola, expressed by (4.4), matches the numerical boundary, expressed by (4.5)-(4.8). The stability parabola and the numerical boundary show the same thing using two different methods. The stability parabola uses energy conservation theorem while the numerical boundary uses mathematics to determine the stability region.

4.2 Stability design consideration

In this section, the BESS stability constraints are considered in the design of the BESS. The stability boundary, introduced in the previous section, is taken into account as a measure to prevent BESS instability. Equation (4.9) shows a linear estimation of the stable region shown in Figure 4.1, expressed by (4.4). This linear approximation is to further investigate the stability criteria in a BESS. Equation (4.9) shows a constraint on the battery bank internal resistance (R_{battery}) and the battery bank voltage (v_{battery}) parameters due to BESS stability.

As was mentioned in Chapter 3, a battery bank is composed of battery cells in parallel (n) and in series (m) (see Figure 3.3). The equivalent battery cell internal resistance ($v_{\text{batt-cell}}$) and the battery cell voltage ($v_{\text{batt-cell}}$) are replaced for the battery bank internal resistance (R_{battery}) and the battery bank voltage (v_{battery}) in equation (4.10). After further simplifications, equation (4.11) shows a constraint on the number of battery cells in parallel (n) and in series (m). Figure 4.3 shows the stable and unstable regions. The y-axis in Figure 4.3 shows the number of batteries in parallel (n) and the x axis shows the number of battery cells in series (m) in a battery pack. Figure 4.3 shows that by an increase in the value of battery cell resistance, the area of the stable region increases. Same is valid for a reduction of battery cell voltage. Hence to ensure that the BESS operates in stable region, the minimum value of battery cell internal resistance ($R_{\text{batt-cell}}$) and the maximum value of battery cell voltage ($v_{\text{batt-cell}}$) need to be considered in (4.11). Therefore, It is interpreted that if (m) and (n) satisfy the inequity of (4.11) at all time, the system would be stable.

$$R_{\text{battery}} \leq a v_{\text{battery}} + b \tag{4.9}$$

$$\frac{m}{n} R_{\text{batt–cell}} \leq amv_{\text{batt–cell}} + b \tag{4.10}$$

$$m > \frac{bn}{R_{\text{batt–cell}} - nav_{\text{batt–cell}}} \tag{4.11}$$

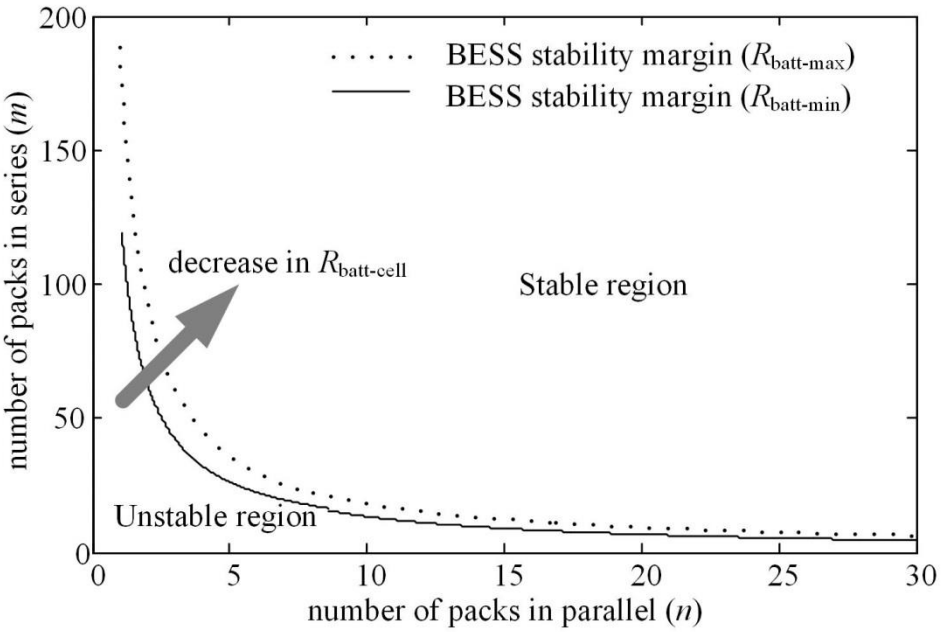

Figure 4.3: BESS stability constraint on battery bank configuration in a 25-kW rated system

In addition to the BESS stability constraint on the battery bank configuration, a BESS power delivery constraint exists as will be discussed. Equation (4.12) shows the power delivery constraint of a BESS battery bank. A BESS battery bank must be able to deliver a certain minimum power (P_{min}) despite the battery cell voltage. Equation (4.12) shows the delivered power in a battery bank composed of a number of battery cells in parallel (n) and in series (m). The minimum value of the battery cell voltage and the maximum battery cell current (set by manufacturer) needs to be considered in (4.12) to form a constraint on (n) and (m). Equation (4.13) shows the power requirement constraint on the number of battery cells in parallel (n) and in series (m) in the BESS battery bank.

Figure 4.4 shows the stability and the power requirement constraints described in (4.11) and (4.13). The constraint margin lines divide Figure 4.3 into four regions. In regions 2 and 3, the converter is stable while in regions 1 and 2 the battery pack is able to deliver the minimum power at all the time. Thus, R2 is the appropriate configuration of the battery bank in which the dc-dc converter is both stable and able to deliver the minimum required power. Figure 4.4 suggests that for a sufficiently large number of battery cells in series (large v_{battery}) or a sufficiently large number of battery cells in parallel (small R_{battery}) the system will be stable. This aligns with the findings of Section 4.2. EMT simulations of a BESS's detailed model in PSCAD/EMTDC confirm that the BESS stability margin and the BESS power requirement margin shown in Figure 4.4 are accurate.

$$mv_{\text{batt-cell(min)}}.nI_{\max} > P_{\min} \tag{4.12}$$

$$m > \frac{P_{\min}}{v_{\text{batt-cell(min)}} nI_{\max}} \tag{4.13}$$

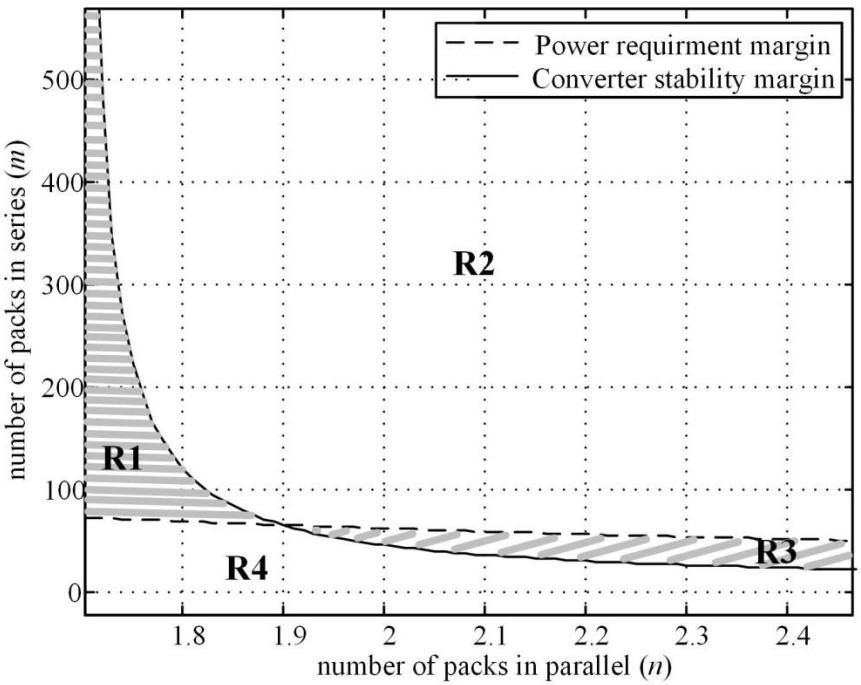

Figure 4.4: Constraints on battery bank configuration in a 25-kW rated system

4.3 Chapter summary and contributions

This chapter analysed the stability of a grid-connected BESS in terms of battery parameters using the developed BESS model in Chapter 3. The stability region of the BESS on the battery internal resistance-battery internal voltage was clearly determined using three different methods. The stability boundary was estimated and was used to derive an inequality to regulate the number of battery cells in a battery bank. The BESS stability and the power requirement constraints on helps the system designers to prevent the described instability in this chapter by appropriately configuring the BESS battery bank.

Chapter 5 BESS Response Dynamics

In this chapter the BESS response dynamics upon a change in the power set-point is studied. In the first section of this chapter, the importance of the dc-link voltage regulation on smooth operation of the BESS is shown. It is shown that dc-link voltage variations have negative impacts on the BESS operation. As is shown in Chapter 2, a BESS dc-dc converter helps to regulate and stabilises the dc-link voltage. Hence, an improvement in BESS dc-dc converter's response time contributes to the improvement of BESS response dynamics. To improve the BESS dc-dc converters response time, the system parameters and the control system configuration is studied in this chapter.

The reduced-order averaged-value model of the BESS (described in Chapter 3) is linearized around an operating point to study the impact of the system parameters on the dc-dc converters response-time. Afterwards, the linearized model is used to study the eigen-values of the closed-loop system. Then, the system parameters are analysed to study their impact on the system's eigen-values and the performance of the BESS. Outcomes of this section are evaluated by EMT simulations of a BESS detailed model in PSCAD/EMTDC.

In the third section of this chapter, a feed-forward/feed-back controller is proposed to improve the BESS dc-dc converters response time. In this section, a feed-forward pathway is added to the closed-loop control system of the BESS described in Chapter 3. Outcomes of this section are evaluated by EMT simulations of a BESS detailed model in PSCAD/EMTDC. The outcomes of this section are also evaluated by experimental tests on a BESS laboratory prototype.

5.1 Impact of dc-link voltage variations on the BESS performance

This section focuses on the impact of the dc-link voltage variation on the BESS operation. Although a constant dc-link voltage is ideal for the VSC operation, dc-link voltage variation is inevitable in particular upon a change in real or reactive power set-point (P_{ref} and Q_{ref} in Figure 2.18).

Upon a change in the VSC power set-point, the dc-link voltage changes due to a mismatch in the VSC and the dc-dc converter dynamics. For example, when the power set-point increases (positive when BESS is discharging), the VSC exports energy from the dc-link capacitor to the grid. Hence, the dc-link voltage decreases momentarily. This activates the control loop of the dc-dc converter and changes the duty cycle such that the dc-link voltage variation is compensated. Alternatively, by a decrease in the VSC power set-point, the dc-link voltage increases momentarily. Figure 5.1 (a) demonstrates the impact of a change in the power set-point (ΔP=350kW) on the dc-link voltage. Table 5.1 shows specifications of the detailed BESS model in PSCAD/EMTDC accordingly. Figure 5.1(b) shows changes of the BESS real and reactive power in the same simulation case. The dc-link voltage fluctuation results in improper operation of VSC's decoupled control system, as will be described later in this section. This is apparent by comparing Figure 5.1(b) with Figure 5.1(c) where the dc-dc converter is replaced by a constant dc source (1.9 kV) in the simulation case. The BESS's real power shown in Figure 5.1(c) resemble a typical first-order system response (τ=0.2). This is expected as VSC's PI controller parameters were selected as described in Chapter 2 (k_p=0.001,k_i=0.5). The reactive power set-point (Q_{ref} in Figure 2.18) is usually set to zero in a BESS for the purpose of maximum real power capability.

Table 5.1: BESS specification

Parameters	Values	Description
L	0.2mH	Line filter inductor
R	0.1Ω	Line filter resistor
L_1	1.5mH	dc-dc converter inductor
C	4000uF	dc-dc converter capacitor
$v_{\text{dc-link}}$	1900V	dc-link voltage
v_{PCC}	690V	PCC voltage

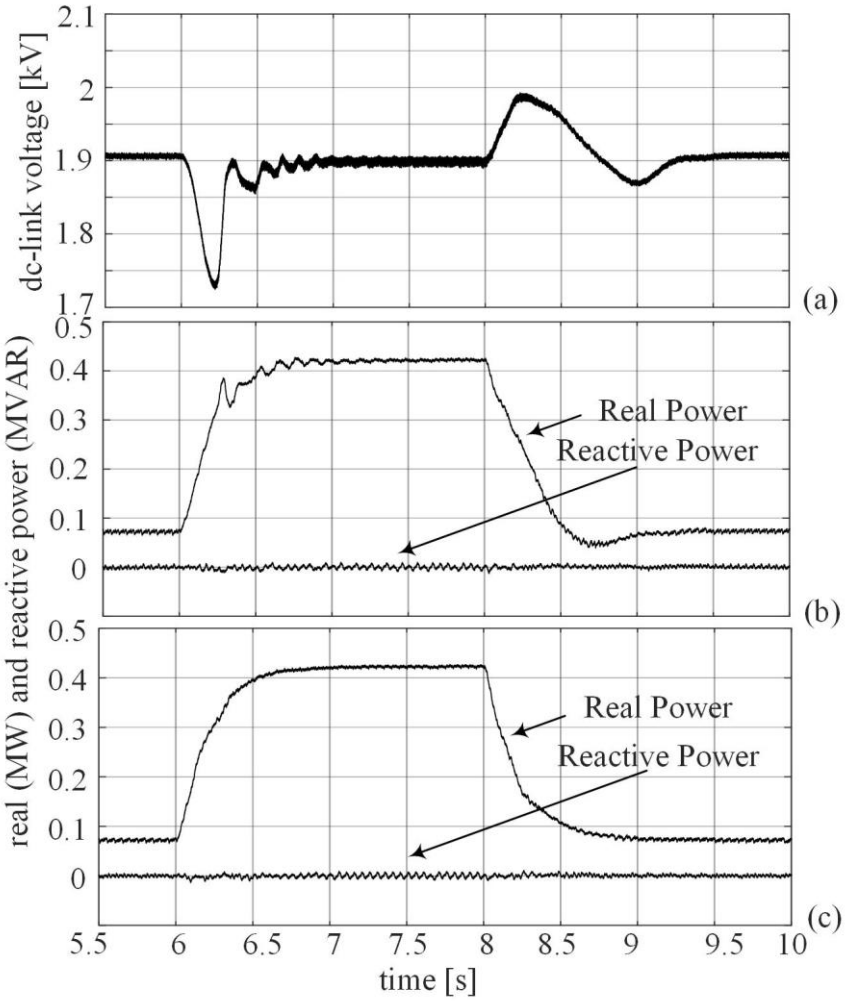

Figure 5.1: Effect of power set-point change (ΔP=350kW positive at t=6s and negative at t=8s) on (a) dc-link voltage, (b) VSC power and reactive power, and (c) VSC power and reactive power with constant dc-link voltage.

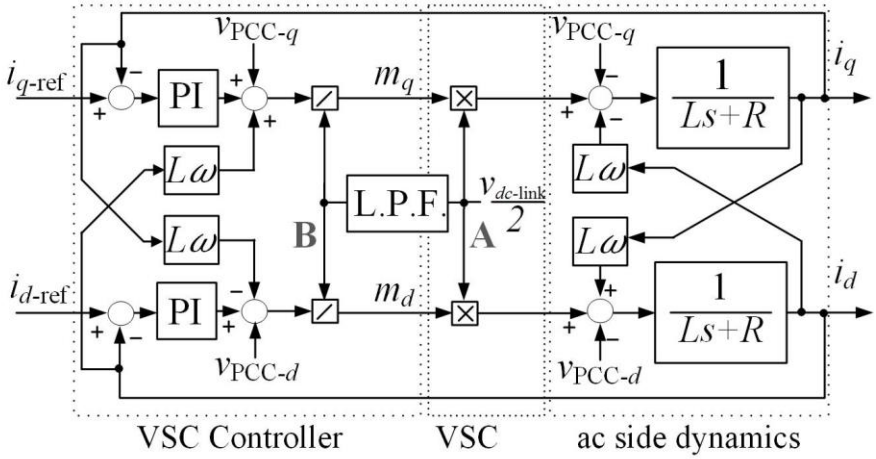

Figure 5.2: Schematic diagram of the VSC controller, the VSC model and the ac side dynamics in qd0 domain

Figure 5.2 shows a schematic diagram of the VSC controller, the VSC model and the ac side dynamics in a BESS. This figure is essentially the same as Figure 2.15. Addition of a VSC averaged-value model in dq0 domain yields Figure 5.2 (see (3.53)). The low pass filter, filters the high frequency components (cut-off frequency of 500 Hz) of the dc-link voltage caused by VSC's high frequency switching. This filter is software-implemented and is used to filter out dc-link voltage ripples.

Since the dc-link voltage variations are minor during normal operation of the BESS, the low pass filter has negligible impact on the operation of the control system. Hence, the effect of low pass filtering is not considered during the tuning procedure of the PI controller parameters as was shown in Figures 2.15 and 2.16.

Upon a change in the voltage of the dc-link, such as when the real and reactive power set-point changes, the voltage of the dc-link in reality and in the control system (points A and B in Figure 5.2 respectively) are not exactly the same. This is due to dynamics of the low pass filter in Figure 5.2. The difference in the voltage of points A and B in Figure 5.2 depends on the level of

change in the dc-link voltage and also on the cutting frequency of the low pass filter. In this circumstance the schematic diagram of the Figure 5.2 could not be simplified as in Figure 2.16.

To prevent improper operation of the VSC's control system upon a change in real and reactive power set-point, this chapter proposes two methods to reduce the dc-link voltage variations and consequently improve the BESS dynamic response. In the first approach the system parameters (in particular battery parameters) are analysed to reduce the dc-link voltage variations as will be described in section 5.2. In the second approach the control system configuration is studied to reduce the dc-link voltage variations as will be described in section 5.3.

5.2 Impact of battery parameters on the dc-link voltage dynamics

The full-order model of the BESS dc-dc converter is used to study the impact of the battery parameters on the dc-link voltage variations upon a change in the real and reactive power set-point in this section. Equations (3.19)-(3.21), (3.57), and (3.58) and also (3.38)-(3.40), (3.57), and (3.58) are linearized to analyse the boost and the buck converters in a BESS. Equation (5.1) shows the linearized system around an operating point (equilibrium point). Constant values in equation (5.1) such as α_i, β_i, and γ_i are given in Appendix 2.

$$\begin{bmatrix} \frac{d}{dt}\Delta i_L \\ \frac{d}{dt}\Delta v_{\text{dc-link}} \\ \frac{d}{dt}\Delta v_{\text{in}} \\ \frac{d}{dt}\Delta x \end{bmatrix} = \begin{bmatrix} \beta_1 & \beta_2 - k_{\text{p}}\beta_4 & \beta_3 & k_{\text{i}}\beta_4 \\ \alpha_1 & \alpha_2 - k_{\text{p}}\alpha_4 & \alpha_3 & k_{\text{i}}\alpha_4 \\ \gamma_1 & 0 & \gamma_2 & 0 \\ 0 & -1 & 0 & 0 \end{bmatrix} \begin{bmatrix} \Delta i_L \\ \Delta v_{\text{dc-link}} \\ \Delta v_{\text{in}} \\ \Delta X \end{bmatrix} + \begin{bmatrix} k_p\beta_4\Delta v_{\text{dclink-ref}} \\ k_p\alpha_4\Delta v_{\text{dclink-ref}} + \alpha_5\Delta R_{\text{load}} \\ 0 \\ \Delta v_{\text{dclink-ref}} \end{bmatrix} \quad (5.1)$$

The two system inputs in (5.1) are the change of the resistive load (ΔR_{load}) and the change of the dc-link voltage set-point ($\Delta v_{\text{dclink-ref}}$). The change of the resistive load (ΔR_{load}) is a disturbance in the sense that it is determined by the VSC load in a BESS as was discussed earlier (see equation (3.57)). The dc-link voltage set-point ($\Delta v_{\text{dclink-ref}}$) is, however, a user-defined input of the BESS control systems. Normally $\Delta v_{\text{dclink-ref}}$ is set to 0 as the intention of the control system is to retain the voltage of the dc-link.

The impacts of the battery internal resistance (R_{battery}) and the battery internal voltage (v_{battery}) on the dc-dc converter's response time are the focus of this section. These two parameters are commonly used in battery applications as was discussed in Chapter 4. These parameters are not the actual 'inputs' of the system in (5.1); rather, they are 'model parameters', which influence the behaviour of the nonlinear and linearized systems.

Figure 5.3 evaluates the accuracy of the linearized model (in MATLAB) against a fully detailed model in the PSCAD/EMTDC for a ±5% change in the value of the dc-dc converter's resistive load, i.e., for a $\Delta R_{\text{load}} = \pm 0.72\ \Omega$ (-at t = 1 s and + at t = 3 s). System specification and

parameter values for simulation cases presented in Figures 5.3-5.7 are given in Table 5.2.

Table 5.2: System specifications

L_1 (μH)	f_s (kHz)	R_{load}(Ω)	$\bar{v}_{dc\text{-}link}$ (V)	k_i	k_p	P_{max}(kW)
368	2	14.4	600	0.01	0.0002	25

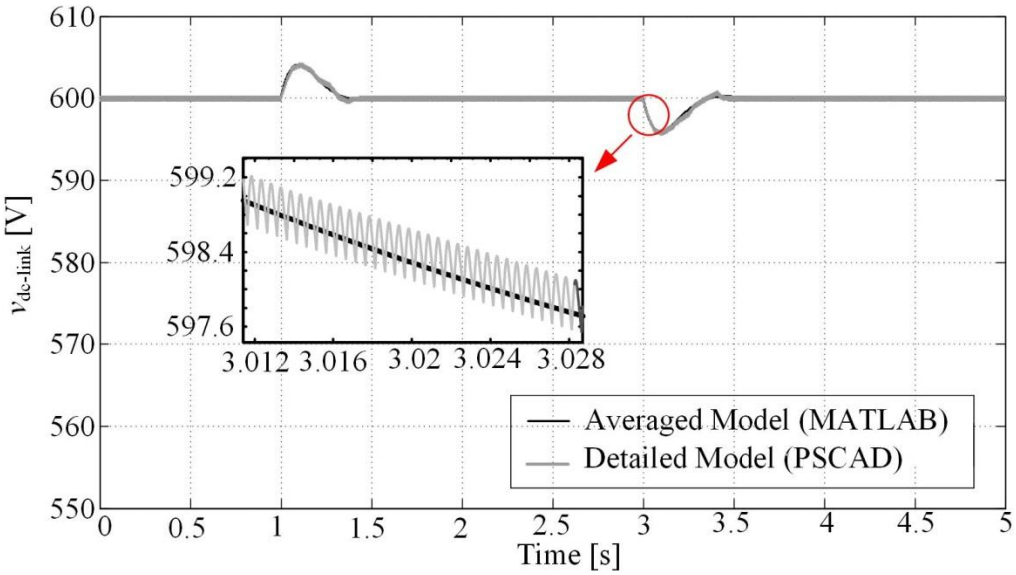

Figure 5.3: The BESS model verification.

Figure 5.4 plots the locus of the system's dominant eigen-values (the system has four poles but only traces of the two poles closer to the $j\omega$ axis are shown here) when the internal voltage of the battery ($v_{battery}$) in the considered case study decreases from 400 V to 300 V. This plot is obtained by observing the movement of the eigen-values of a set of linearized models around 25 different operating points when the battery voltage is incrementally changed in 25 steps from 400 V to 300 V.

As seen this change moves the dominant eigen-values of the system closer to the $j\omega$ axis, causing a slower response and further closeness to instability. Note that the elements of the matrices in (5.1) are independent of the internal voltage of the battery ($v_{battery}$); however,

variations of the internal voltage of the battery ($v_{battery}$) do affect the operating point of the nonlinear system and consequently the eigen-values of the linearized model. The system also has a complex-conjugate pair of non-dominant eigen-values at high frequencies (not shown).

Figure 5.5 shows the time-domain response of the converter to a -5% change in its resistive load for different values of the battery internal voltage ($v_{battery}$). Two traces, one from the linearized model and one from a detailed EMT simulation model in the PSCAD/EMTDC, are shown for each value of the internal battery voltage. As expected from the eigen-value plot of Figure 5.4, the response of the system becomes faster for larger battery internal voltage ($v_{battery}$) values.

It is important to note that the EMT model developed is a fully-detailed representation of the nonlinear dynamics of the system. This model includes the switching components of the converter topology and uses high-frequency PWM for generation of the firing pulses. Other details of the system including controller dynamics are also fully included.

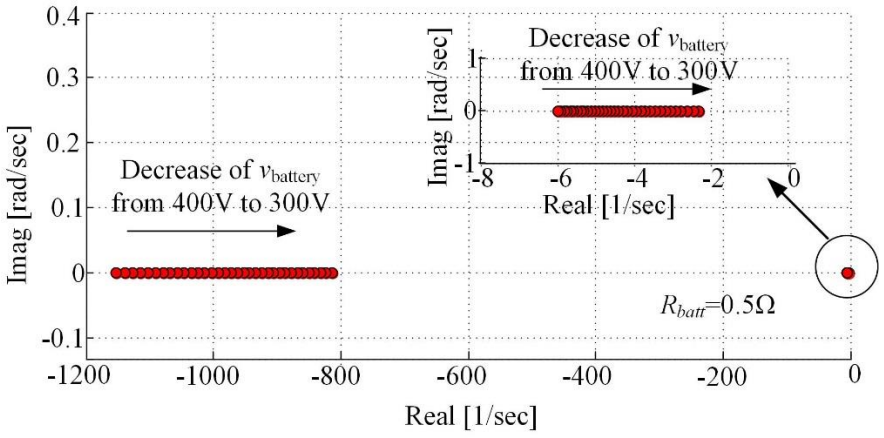

Figure 5.4: Locus of the system eigen-values for the change of the battery's internal voltage.

Figure 5.6 shows the change in the location of the system's dominant eigen-values as the internal resistance of the battery ($R_{battery}$) increases. As seen one of the (real) dominant poles of

the system crosses the $j\omega$ axis for a sufficiently large value of the internal resistance causing instability. For values less than this threshold the response of the system remains stable but become increasingly slower as the $R_{battery}$ increases.

Similar to Figure 5.5, Figure 5.7 shows the system response to a -5% change in the load resistance for different values of the internal resistance, which confirm the slowing of the response for larger internal resistance values.

The time-domain system responses in Figure 5.5 and Figure 5.7 verify that by an increase in the value of the battery internal resistance ($R_{battery}$) or a decrease in battery internal voltage ($v_{battery}$) the system becomes slower. This aligns with the findings from Figure 5.4 and Figure 5.6, where the movements of the systems dominant eigen-values are depicted.

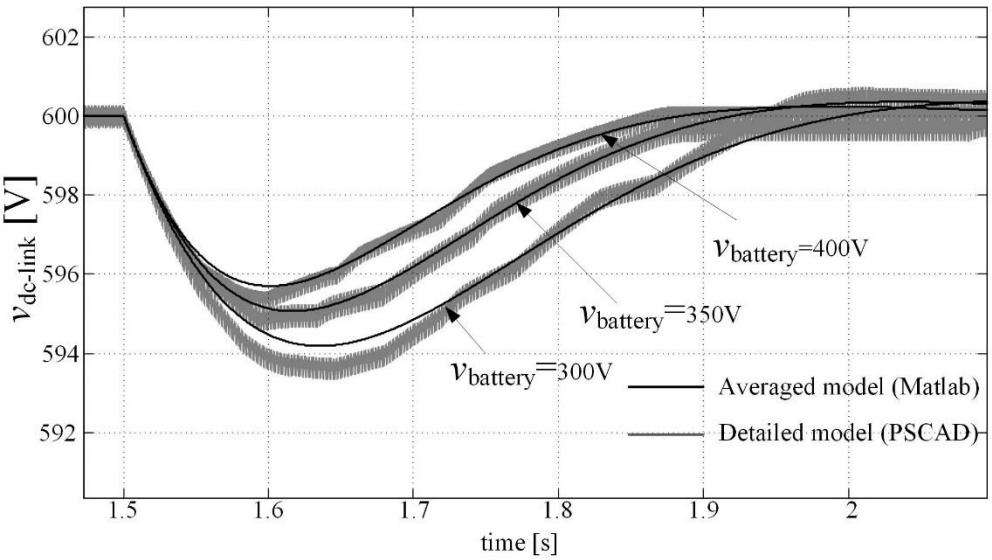

Figure 5.5: Small signal response of the dc-link voltage to a load change for different $v_{battery}$ values.

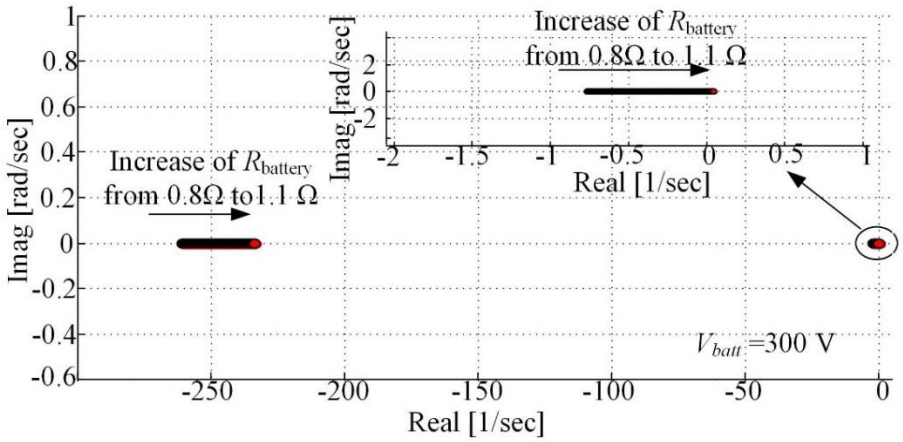

Figure 5.6: Locus of system's dominant eigen-values for the change of the battery's internal resistance.

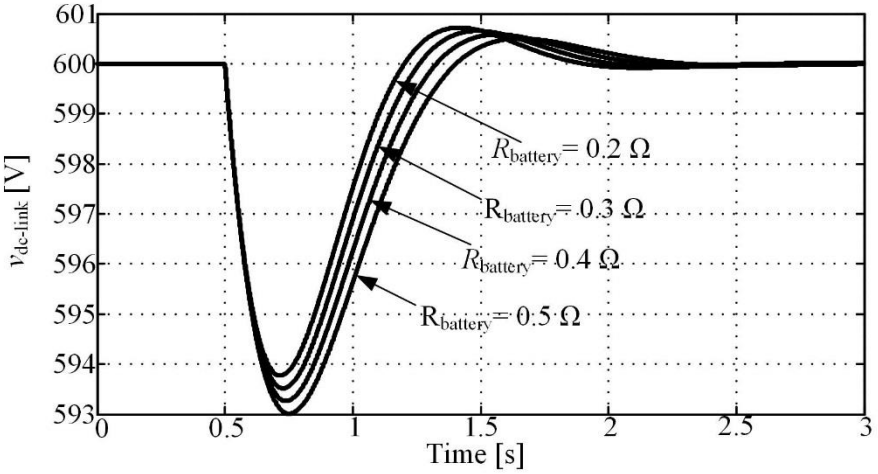

Figure 5.7: dc-link voltage response of the linearized model to a load change for different $R_{battery}$ values.

5.2.1 Performance evaluation

This section shows EMT simulation results of a fully detailed model of a BESS (detailed models are used for both the dc-dc converter and the VSC). The system specifications for the simulation results shown in Figure 5.8 and 5.9 are as the system of Table 5.1. Figure 5.8 shows the drop in the dc-link voltage upon a change in the power set-point (ΔP=300kW). As is shown in Figure 5.8, the BESS with lower battery internal resistance has a faster response time in maintaining the dc-link voltage. Figure 5.9 shows the drop in the dc-link voltage upon a change in the power set-

point (ΔP=300kW). As is shown in Figure 5.8, the BESS with higher battery internal voltage has a faster response time in maintaining the dc-link voltage. The EMT simulation results for the buck converter leads to the same conclusion as of boost converter.

Following the same principle discussed in Chapter 4, the configuration of the battery bank was analysed to study the impact of the battery configuration on the response time of the BESS dc-dc converter upon a change in the BESS power set-point. Simulation results show that by increasing the number of batteries in series (increase of battery bank internal voltage) and increasing the number of battery cells in parallel (reduction of battery bank internal resistance) the dc-dc converter response-time upon a change in the BESS power set-point improves.

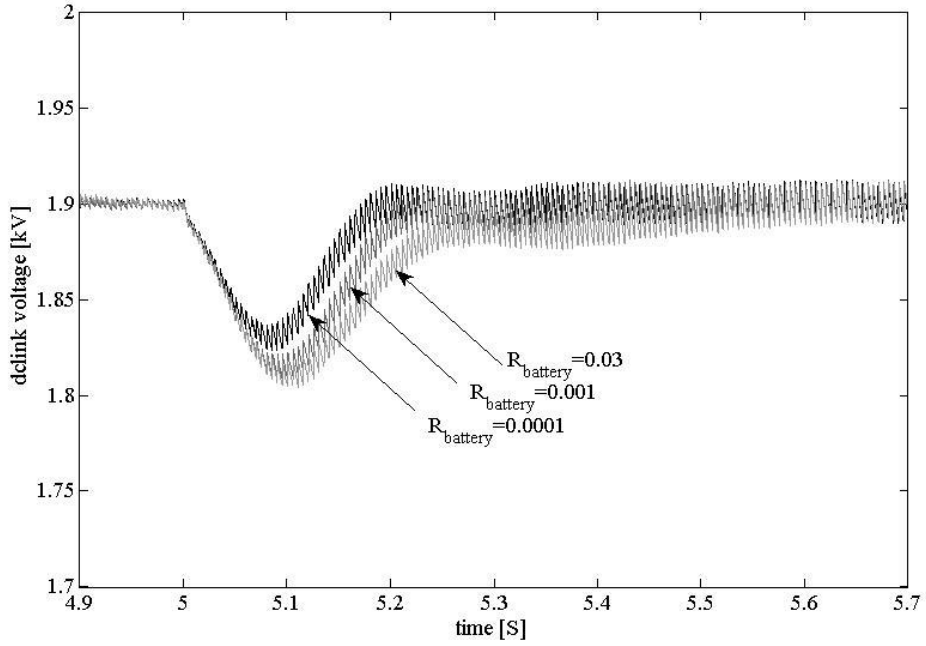

Figure 5.8: Comparing dc-link voltage changes in a BESS with different battery internal resistance

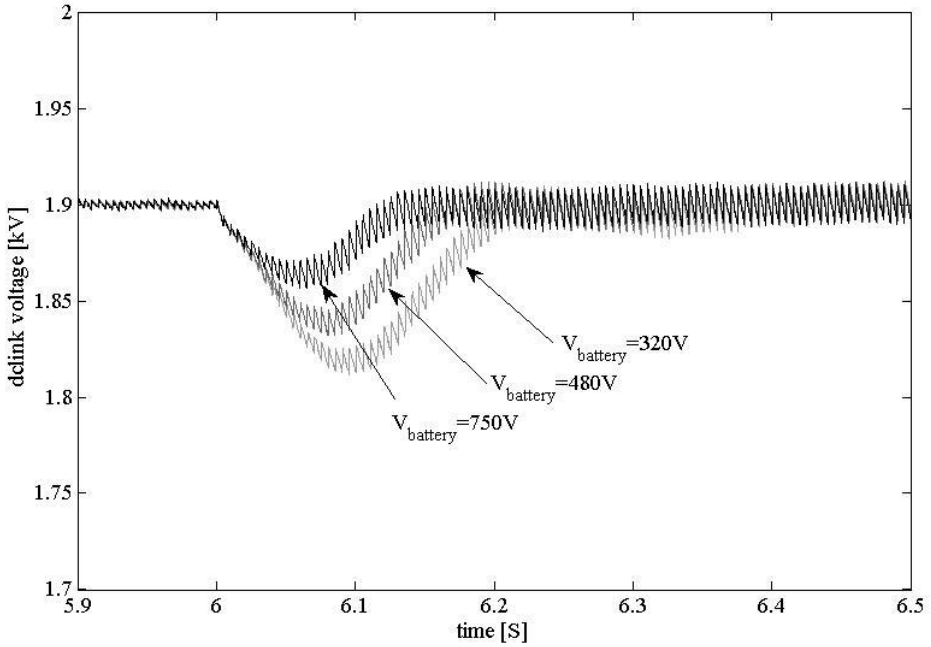

Figure 5.9: Comparing dc-link voltage changes in a BESS with different battery internal voltage

5.3 BESS controller improvement

This section aims to improve the response-time of the BESS dc-dc converter by the means of designing a feed-forward controller. The feed-forward controller improves a system's performance due to its disturbance rejection capability [57]. Figure 5.10 shows the schematic diagram of a feed-forward controller. In feed-forward control strategy, the disturbance (x_d (s)) proceeds in parallel through the process (P(s)), and the feed-forward controller (G_{ff}(s)=-G_d(s)/P(s)). The controller manipulates the disturbance to counteract the disturbance effect in the output (y(s)).

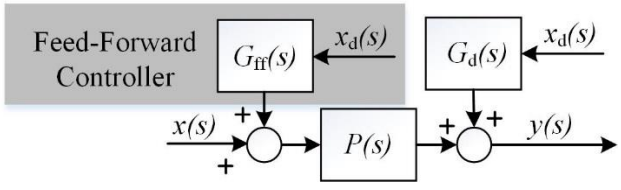

Figure 5.10: Schematic diagram of a feed-forward controller

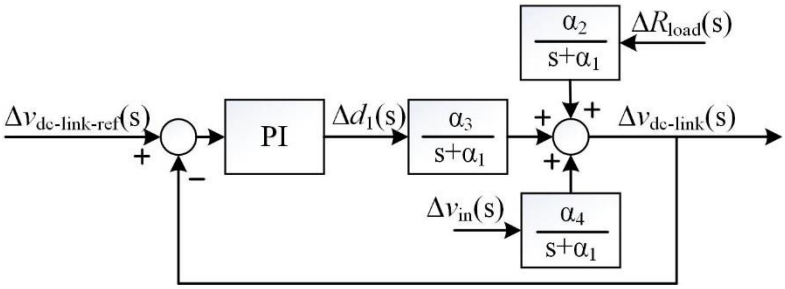

Figure 5.11: Schematic diagram of a boost dc-dc converter's feed-back control system.

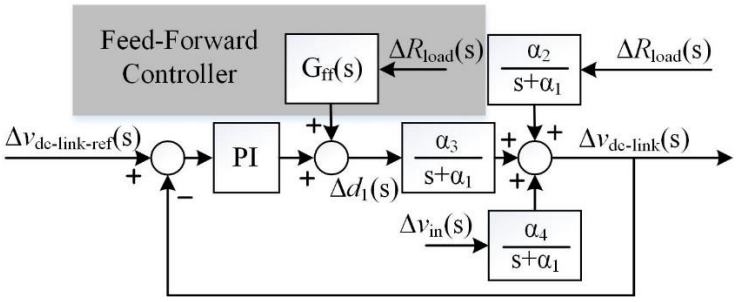

Figure 5.12: Schematic diagram of a boost dc-dc converter's feed-back/feed-forward control system.

Equation (5.2) is the linearized expression of a reduced-order averaged-value model of a BESS around an operating point. Values of α_i are presented in Appendix 2 for the buck and boost converter. Equation (5.3) presents (5.2) in the Laplace domain. As is seen in (5.3), the dc-link voltage is affected by changes in the load (ΔR_{load}), changes in the duty cycle (Δd_1), and changes in the converter's input voltage (Δv_{in}). Variations in dc-dc converter input voltage (Δv_{in}) are caused by changes in the battery terminal voltage. Δv_{in} is assumed to be zero in this paper (ideal battery model with low internal resistance). Changes in the load (ΔR_{load}) are caused by changes in BESS exchanged power with the grid (ΔP). Figure 5.11 shows the schematic diagram of the dc-dc converter closed-loop control system.

$$\frac{d\Delta\bar{v}_{\text{dc-link}}}{dt} = \alpha_1\Delta\bar{v}_{\text{dc-link}} + \alpha_2\Delta R_{\text{load}} + \alpha_3\Delta d_1 + \alpha_4\Delta v_{\text{T1}} \tag{5.2}$$

$$\Delta\bar{v}_{\text{dc-link}}(s) = \frac{\alpha_2}{s+\alpha_1}\Delta R_{\text{load}}(s) + \frac{\alpha_3}{s+\alpha_1}\Delta d_1(s) + \frac{\alpha_4}{s+\alpha_1}\Delta v_{\text{in}}(s) \tag{5.3}$$

Figure 5.12 shows the schematic diagram of the proposed feed-back/ feed-forward control system. The feed-forward controller (G_{ff}(s)) should cancel out the effect of a change in the load (ΔR_{load}) on the dc-link voltage ($\Delta v_{\text{dc-link}}$) as described in (5.4). The poles of the disturbance gain ($G_{\text{d}}(s)=\alpha_2/s+\alpha_1$) and the process ($P=\alpha_2/s+\alpha_1$) are on the left hand side of $j\omega$ axis, hence the proposed controller does not cause instable pole/zero cancellation. The duty cycle (d_1) and the load value (R_{load}) of the operating point in (5.4) are obtained as described in (5.5).

$$\mathrm{G}_{ff}(s) = -\frac{\dfrac{\alpha_2}{s+\alpha_1}}{\dfrac{\alpha_3}{s+\alpha_1}} = -\frac{\alpha_2}{\alpha_3} = -\frac{d_1}{2R_{\text{load}}} \tag{5.4}$$

The dc-dc converter's input power equals the dc-dc converter's output power and the VSC's output power in a BESS as is shown in (5.5). Equation (5.5) is valid for different operating points. Replacement of (3.28) and (3.47) in (5.5) for averaged inductor current and further simplification results in the feed-forward controller as described by (5.6) and (5.7) for the boost and the buck dc-dc converter respectively.

$$\bar{i}_L \times v_{in} = \frac{\bar{v}_{\text{dc-link}}^2}{R_{\text{load}}} \tag{5.5}$$

$$G_{\text{ff}}(s) = -\frac{\alpha_2}{\alpha_3} = -\frac{\sqrt{(v_{\text{dc-link}} - v_{\text{T1}})L_1 v_{\text{dc-link}}}}{R_{\text{load}}\sqrt{2v_{\text{T1}}^2 T_s R_{\text{load}}}} \tag{5.6}$$

$$G_{\text{ff}}(s) = -\frac{\alpha_2}{\alpha_3} = \frac{\sqrt{L_1 v_{\text{dc-link}}}}{R_{\text{load}}\sqrt{2(v_{\text{T1}} - v_{\text{dc-link}})T_s R_{\text{load}}}} \tag{5.7}$$

Since the small signal analysis is accurate in proximity of the operating point, the average value of the load value (R_{load}) before and after the change of the operating point is used for improved results in (5.6) and (5.7).

5.3.1 Performance Evaluation

In this section, the performance of the proposed feed-back/feed-forward controller for a grid-connected BESS is evaluated by means of EMT simulations in PSCAD/EMTDC and experimental tests on a laboratory prototype.

5.3.1.1 EMT simulations

The simulation results of the proposed feed-back/feed-forward controller, in PSCAD/EMTDC environment, are reported in this section. A detailed model of a grid-connected BESS is adopted, whose parameters are set according to Table 5.1. The simulation studies were conducted for boost (discharging batteries) and buck (charging batteries) operating modes of the dc-dc converter in the grid-connected BESS to evaluate the performance of the proposed controller. This section shows results for the boost operating mode of the dc-dc converter since computer simulations of buck operating mode of the dc-dc converter shows similar results. As is shown in

Figure 5.13, the system with the feed-forward/feed-back controller performs better compared to the system with only the feed-back controller.

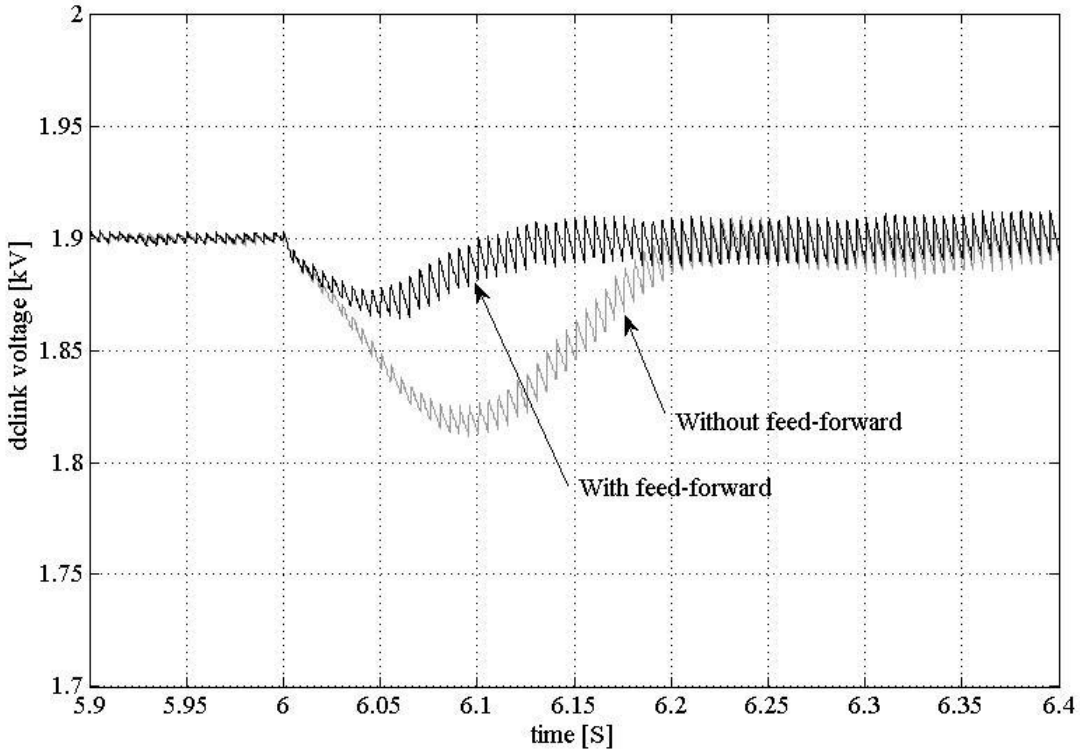

Figure 5.13: Comparing dc-link voltage changes in a BESS with and without feed-forward controller upon a change in power set-point

5.3.1.2 Experimental Results

In order to experimentally verify the findings, a BESS laboratory prototype with the same layout as the study system of Figure 2.17 is used. A 12V-220Ah AGM Victron lead-acid battery is used in the test bench. The PCC in the test-bench is replaced with a resistive-inductive (*RL*) load with parameters indicated in Table 5.2. The proposed feed-back/feed-forward controller is implemented for the boost operation of the dc-dc converter in a fully customized digital control

platform using a C2000 Piccolo LaunchPad shown in Figure 5.14. The C2000 Piccolo LaunchPad is from a series of 32-bit Texas instrument microcontroller family that are commonly used for real-time applications. It includes a 60 MIPS processing core, a 64 kB of integrated flash, 8 PWM channels and 12-bit analogue to digital converters.

Table 5.3: Test bench specifications

Parameters	Values	Description
L	1.5mH	Load inductance
R	10Ω	Load resistance
L_1	1.5mH	dc-dc converter inductor
C	44000uF	dc-dc converter capacitor
$v_{\text{dc-link}}$	100V	dc-link voltage
v_{battery}	12V	battery voltage

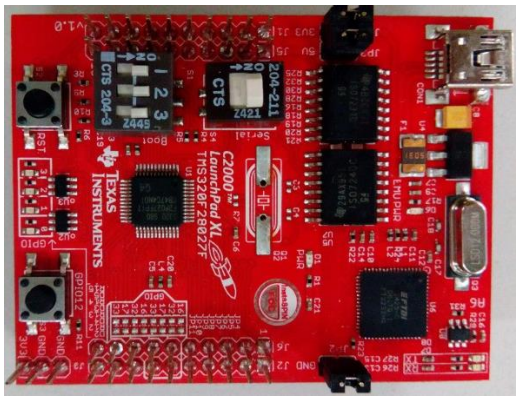

Figure 5.14: C2000 Piccolo Launchpad

The dc-dc converter and the VSC were designed and developed in the Power Electronics Advanced Research Laboratory at Monash University using two converter boards. Figure 5.15 shows the converter board. A Fairchild semiconductor smart power module (SPM 45H), which includes three pairs of IGBTs was used on each converter board. Figures 5.16 and 5.17 show pictures of the test bench.

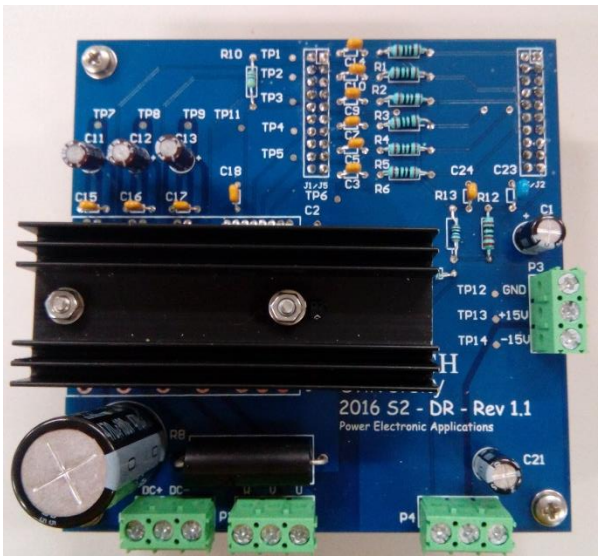

Figure 5.15: Converter board

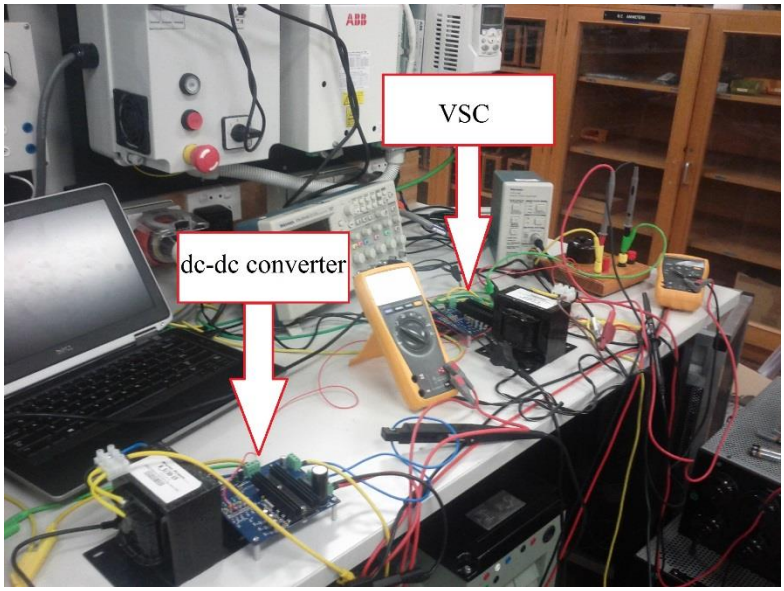

Figure 5.16: Test setup showing the dc-dc and voltage-source converters

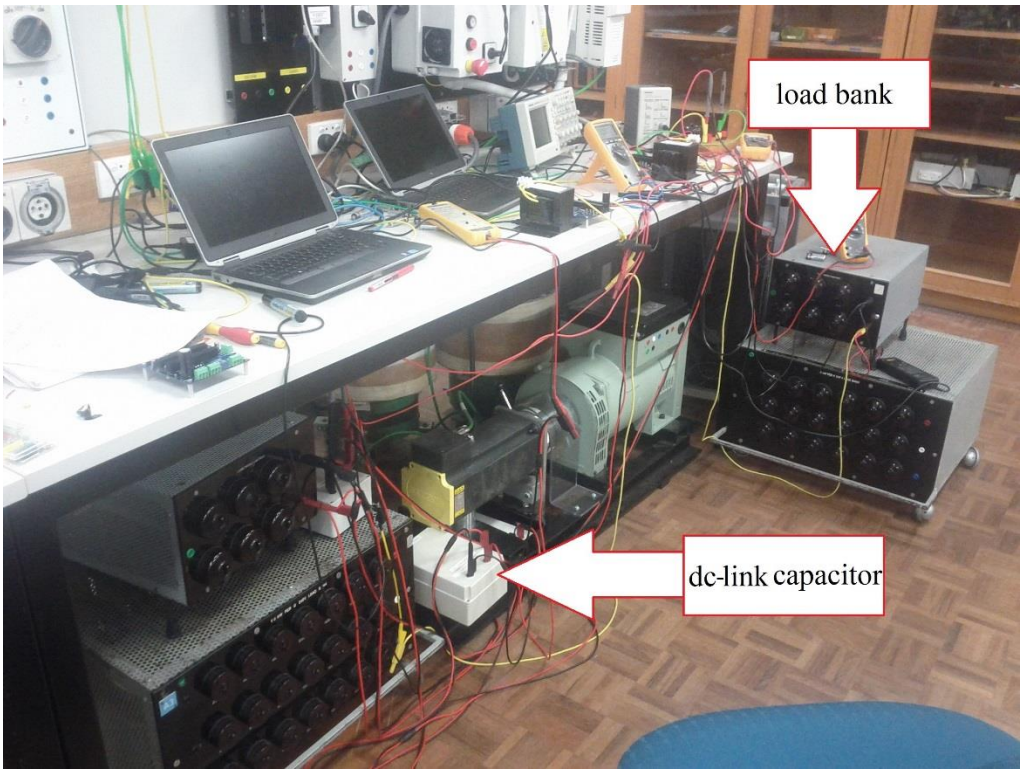

Figure 5.17: Test setup showing the dc link capacitor and load banks.

Fig. 5.18 shows the dc-link voltage of the BESS (laboratory prototype and EMT simulation) upon a change in power set-point (ΔP=100 W positive at t = 1 s and negative at t = 6 s). A feed-back control strategy is used in Fig. 5.18 (a) and (b). Figs. 5.18 (a) and (b) show the dc-link voltage of the BESS in the experimental and EMT simulation respectively. A feed-back/feed-forward control strategy is used in Fig. 5.18 (c) and (d). Figs. 5.18 (c) and (d) show the dc-link voltage of the BESS in the experimental and EMT simulation respectively. As is shown in Fig. 5.18, the experimental tests verify performance of the proposed feed-forward control strategy in maintaining the dc-link voltage upon a change in the power set-point.

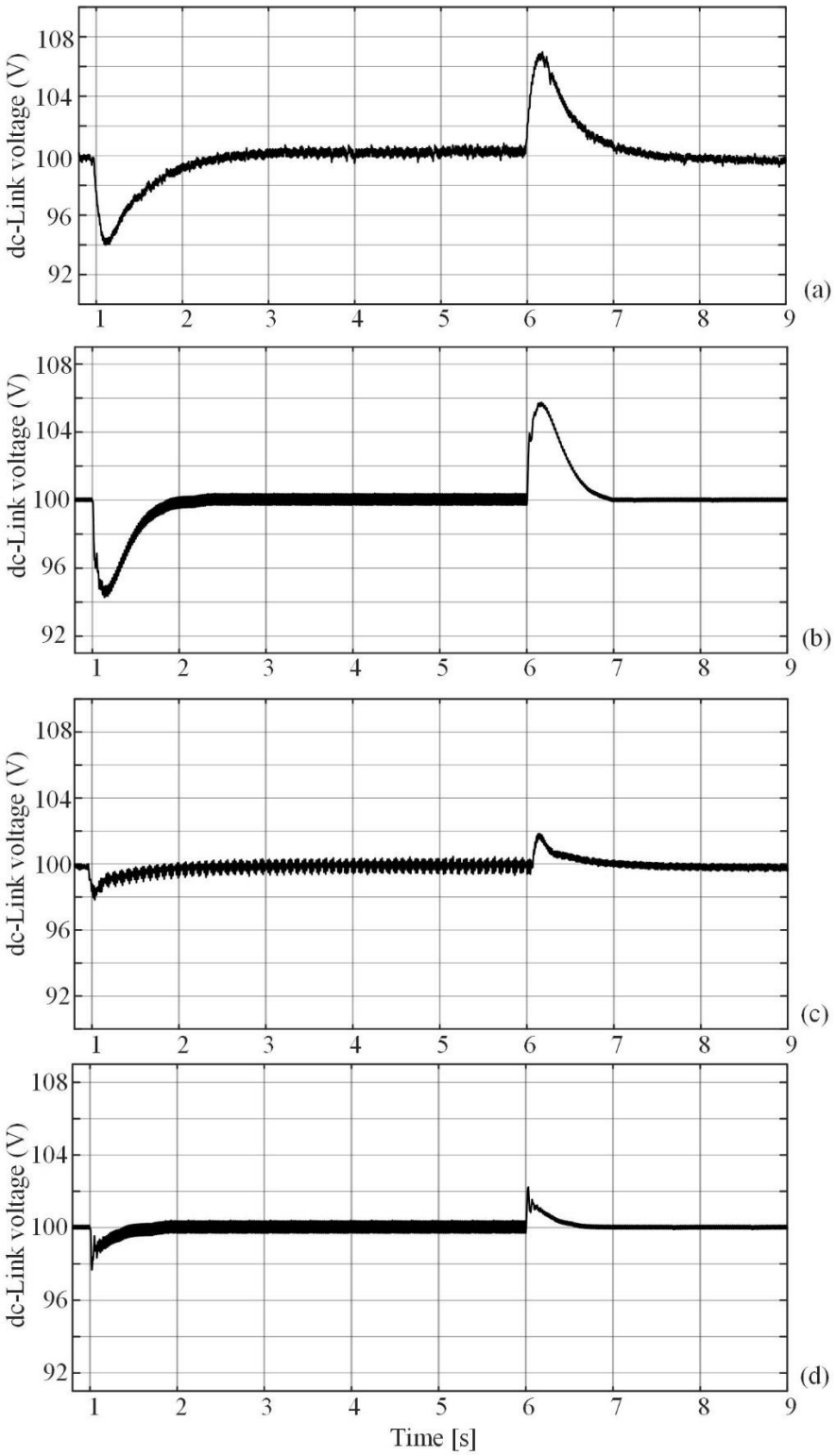

Figure 5.18: BESS dc-link voltage change upon a change in power set-point, (a) feed-back controller is used in experimental setup, (b) feed-back controller is used in EMT simulation (c) feed-back/feed-forward controller is used in experimental setup, (d) feed-back/feed-forward controller is used in EMT simulation

Fig 5.19 shows the dc-link voltage of the same setup in Fig. 5.18 with a larger sized capacitor ($C_{\text{dc-link}}$ = 8800 µF) for the same change in the power set-point (ΔP=100 W positive at t = 1 s and negative at t = 6 s). A feed-back control strategy is used in Figs. 5.19 (a) and (b). Figs. 5.19 (a) and (b) show the dc-link voltage of the BESS in the experimental and EMT simulation respectively. A comparison between Figs. 5.18 (c) and 5.19 (a) and also Figs. 5.18 (d) and 5.19 (b) shows that the addition of the feed-forward pathway to the exisiting feed-back control strategy has the same impact of enlarging the dc-link capacitor in regulation of dc-link voltage upon a change in the power set-point. Hence, the proposed feed-forward controller could be used to eliminate the need of an increase in the BESS dc-link capacitor size for dc-link voltage regulation upon a change in power set-point.

Figure 5.19: BESS dc-link voltage change upon a change in power set-point, (a) feed-back controller (experimental result, $C_{\text{dc-link}}$ = 8800 µF), (b) feed-back controller (EMTDC simulation, $C_{\text{dc-link}}$ = 8800 µF).

5.4 Chapter Summary and contributions

This chapter showed the importance of the dc-link voltage regulation on the smooth operation of the BESS. It was shown that the dc-link voltage deviations upon a change in the BESS power set-point could cause fluctuations in the BESS power dynamic profile. Since the dc-dc converter regulates the dc-link voltage in a BESS (as was discussed in Chapter 2), it is interpreted that by increasing the response time of the dc-dc converter, any fluctuations in the dc-link voltage will be eliminated in a shorter time interval and less fluctuations would occur in the BESS power dynamic profile. The system parameters and the control system of the dc-dc converter were studied to improve the dc-dc converter's response time in this chapter.

The impact of battery parameters on the dc-dc converters response time was studied in this chapter. It was shown that an increase in the battery bank internal resistance or a decrease in the battery internal voltage moves the closed-loop eigen-values further from the ($j\omega$) axis and makes the system slower. Time-domain EMT simulations were also performed for the boost and buck operation of the BESS dc-dc converter to evaluate this.

A feed-back/feed-forward controller was proposed in the third section of this chapter to reduce the dc-link voltage variations in a BESS upon a change in the power set-point. The third section of this chapter also included the tuning procedure for the proposed feed-back/feed-forward controller. The performance of the proposed controller was evaluated by means of EMT simulations of a detailed BESS model and experimental tests on a BESS laboratory prototype test-bench.

Chapter 6 Contributions, Conclusions, and Recommendations for Future Work

6.1 Conclusions and contributions

This chapter presents the conclusions and contributions of this thesis as outlined below. Contributions 1, 2, 3 and 5 have been published in the form of a research paper in a peer-reviewed IEEE journal. Contributions 4 and 6 have been presented in the form of a research paper in a peer-reviewed IEEE Journal (under review at the time of writing this thesis).

1) BESS Modeling: At first, BESS components were separately modeled in this study. The Shepherd model was introduced, which was later used in the EMT simulation cases. The result of these simulation cases were later shown in Chapters 4 and 5. Two averaged-value models (one reduced-order and one full-order) were developed and evaluated for the buck and the boost mode of the BESS dc-dc converter. These models were used to model a BESS in this thesis. Furthermore, a variable resistive load was developed, evaluated, and presented as a VSC model in this thesis. The BESS modeling was presented in Chapter 3 of this report.
2) BESS stability study: A stability plane (in terms of battery parameters) was introduced in this thesis. The stable and the unstable regions were clearly indicated on the plane using three different methods. It was shown that an increase in the value of the battery internal resistance or a decrease in the value of battery state of charge (consequently internal voltage) could cause instability if the operating point of the system is chosen close to the stability boundary. These analyses were carried out by analysing the BESS model

presented in Chapter 3. The battery stability study was presented in Chapter 4 of this thesis.

3) BESS battery bank structure review: The configuration of the battery cells in a battery bank was studied in this thesis. It was shown that the power delivery constraint (ensures that the battery bank can deliver the required power) and the BESS stability constraint (estimated from outcomes of BESS stability study) are important in determination of the BESS battery bank configuration. These two constraints were studied in this thesis (Chapter 4) to propose the structure of the BESS battery bank.
4) Importance of dc-link voltage regulation on BESS operation: The importance of the dc-link voltage regulation for smooth BESS operation was shown in this thesis. It was shown that sudden changes in the BESS dc-link voltage causes ripples in the BESS power exchange dynamics. This part of the study was shown in Chapter 5 of the thesis.
5) Studying Impact of battery parameters on a BESS dc-dc converter response time: A regulated dc-link voltage is appealing for smooth operation of the BESS in particular upon changes in the BESS power set-point. The change in the BESS power set-point is essentially a disturbance for the BESS dc-dc converters control system. The impact of battery parameters on the dc-dc converters response time was studied in this thesis. It was shown that a reduction in the battery internal resistance or an increase in the battery internal voltage improves the dc-dc converters response time. These findings could help the system designers to appropriately select the type of battery or configuration of the battery bank (so that for example the equivalent resistance of the battery bank would be low) in fast response applications. Findings of this part were presented in Chapter 5 of this thesis.

6) Improvement of the BESS dc-dc converter response-time: To improve the dc-dc converters response time upon a change in the BESS power set-point a feed-back/feed-forward controller was suggested in this thesis. The tune procedure of the feed-forward path way was presented in the Chapter 5 of this thesis.
7) ESS Literature review: In this study, different ESS types and applications were reviewed in the literature. The important parameters in the type selection of the BESS such as response time, efficiency, discharge duration and life cycle were studied. Each ESS type has a specific characteristic due to its nature and is suitable for a specific range of applications. The ESS literature review was presented in Chapter 1 of this thesis.
8) BESS Literature review: The structure, topology, components, and control systems of a BESS were studied. The batteries, dc-dc converters, and voltage source converters are the major components of a BESS. Differences between various types of batteries, the structure, the principle of operation and the control system of a dc-dc converter and a voltage source converter were also studied. The BESS literature review was presented in Chapter 2 of this thesis.
9) EMT simulation cases: A detailed model of a BESS was developed in an electromagnetic transient simulation software (PSCAD/EMTDC) to perform the computer simulations. The BESS was used in a bulk energy storage application in simulation cases of this thesis. Simulation cases were developed to evaluate effectiveness of the findings mentioned earlier.
10) BESS laboratory prototype: A small-scale laboratory prototype was developed to evaluate the performance of the proposed feed-back/feed-forward method. The dc-dc converter and the VSC were designed in house at the advanced power electronics lab at Monash

University. The test results of the experimental setup were presented in Chapter 5 of this thesis.

6.2 Recommendations for future work

This sections presents recommendations for future work. The recommendations are as follows:

1) In this study, the BESS was connected to the grid. The BESS is composed of a battery bank, a dc-dc converter and a VSC. The VSC is connected to the grid via RL loads, which resembles the transformer and/or the transmission line. The grid is a three-phase system, which is considered as the phase reference in this study. Virtually the same components and control systems exist in an electric vehicle with an induction motor as the traction system. A battery bank is connected to a dc-dc converter in an electric vehicle. The dc-dc converter is connected to a VSC that drives an induction motor. Since the induction motor can be modeled as an RL load, the structure of the studied grid-connected BESS is similar to the described system in an electric vehicle. The load on the vehicle's traction system depends on the weight, slope of the road and vehicle speed and acceleration. Thus, the load is not constant and changes due to driving circumstances [71].

   The described approach of this study can be applied to an electric vehicle to study the effect of battery parameters on the operation of the vehicle's traction system. It is also interesting to investigate the effect of dc-link voltage regulation methods on the electric vehicle's traction system performance.

2) In this study, the impact of battery parameters on the response-time of the dc-dc converter was studied. There are a few other parameters in the BESS that may contribute in the

BESS dc-dc converters response time and the BESS response dynamics such as values of the LR filter that connects the VSC to the grid, dc-link capacitor value, or the PI controller parameters that are used in the control systems of the VSC. Investigation on how these parameters could impact the BESS response dynamic is suggested as a line for future work.

3) The study of stability and dynamics of battery energy storage systems in the context of renewable energy sources such as in a wind or solar farm is also recommened as future work.

Appendices

7.1 Appendix 1

The matrix elements for the boost dc-dc converter is as follows:

$$\beta_1 = \frac{2L_1(v_{T1} - v_{dc\text{-}link})}{d_1 T_S v_{T1} L_1}, \qquad \beta_2 = \frac{d_1^2 T_S v_{T1} - 2i_L L_1}{d_1 T_S v_{T1} L_1}, \beta_3 = \frac{d_1^2 T_S v_{dc\text{-}link} + 2i_L L_1}{d_1 T_S v_{T1} L_1}, \beta_4 = \frac{2v_{dc\text{-}link}}{L_1} \quad , \alpha_1 = \frac{1}{C_2}$$

$$\alpha_2 = -\frac{1}{C_2 R_{load}} , \qquad \alpha_3 = \frac{T_S d_1^2}{2L_1 C_2}, \ \alpha_4 = -\frac{v_{T1} T_S d_1}{L_1 C_2}$$

$$\alpha_5 = \frac{2L_1 i_L - d_1^2 T_S v_{in}}{2L_1 C_2 R_{load}} \ , \gamma_1 = -\frac{1}{C_1} \ , \gamma_2 = -\frac{1}{R_{battery} C_1}$$

The matrix elements for the buck dc-dc converter is as follows:

$$\beta_1 = \frac{2(v_{T1})}{(v_{T1} - v_{dc\text{-}link}) d_1 T_s}, \qquad \beta_2 = \frac{d_1 v_{dc\text{-}link} + d_1(v_{T1} - v_{dc\text{-}link})}{(v_{T1} - v_{dc\text{-}link}) L_1}, \beta_3 = \frac{2i_L L_1 - d_1^2 T_s v_{dc\text{-}link}}{d_1 T_S (v_{T1} - v_{dc\text{-}link}) L_1},$$

$$\beta_4 = \frac{-2v_{dc\text{-}link}}{L_1} \quad , \alpha_1 = 0$$

$$\alpha_2 = \frac{-d_1^2 T_s R_L - 2L}{2LC_2 R_{load}} \ , \alpha_3 = \frac{T_S d_1^2}{2R_{load} L_1 C_2}, \ \alpha_4 = -\frac{(v_{T1} - v_{dc\text{-}link}) T_S d_1}{L_1 C_2}$$

$$\alpha_5 = \frac{d_1^2 T_s (v_{T1} - v_{dc\text{-}link})}{2L_1 C_2 R_{load}} \qquad , \gamma_1 = -\frac{1}{C_1} \ , \gamma_2 = -\frac{1}{R_{battery} C_1}$$

7.2 Appendix 2

Boost converter parameters:

$$\alpha_1 = -\frac{v_{T1} - 2v_{dc\text{-}link}}{R_{load} C_2 (v_{dc\text{-}link} - v_{T1})}$$

$$\alpha_2 = \frac{{v_{T1}}^2 d_1^2 T_S}{2L_1 C_2 R_{load} (v_{dclink} - v_{T1})}$$

$$\alpha_3 = \frac{v_{T1}^2 d_1 T_S}{L_1 C_2 (v_{dc\text{-}link} - v_{T1})}$$

$$\alpha_4 = \frac{v_{\text{T1}} d_1^2 T_{\text{S}} R_{\text{load}} + L_1 v_{\text{dc-link}}}{L_1 C_2 R_{\text{load}} (v_{\text{dc-link}} - v_{\text{T1}})}$$

Buck converter parameters:

$$\alpha_1 = \frac{d_1^2 T_{\text{S}} + 2L_1}{2L_1 R_{\text{load}} C_2}$$

$$\alpha_2 = \frac{(v_{\text{T1}} - v_{\text{dc-link}}) d_1^2 T_{\text{S}}}{2L_1 C_2 R_{\text{load}}}$$

$$\alpha_3 = \frac{d_1 v_{\text{T1}} T_{\text{S}} - d_1 v_{\text{dc-link}} T_{\text{s}}}{L_1 C_2}$$

$$\alpha_4 = \frac{d_1^2 T_{\text{s}}}{2L_1 C_2}$$

References

[1] P. Kundur, Power systems stability and control, Mcgraw-hill, 1994.

[2] L. Grigsby, Power systems stability and control, CRC press, 2012.

[3] P. Denholm, E. Ela, B. Kirby and M. Milligan, "The Role of Energy Storage with Renewable Electricity Generation," National Renewable Energy Laboratory, 2010.

[4] R. Gupta, N. K. Sharma, P. Tiwari, A. Gupta and N. Nigam, "Application of energy storage devices in power systems," *International Journal of Engineering, Science and Technology*, vol. 3, no. 1, 2011.

[5] A. Joseph, "Battery storage systems in electri power systems," in *Power Engineering Society General Meeting*, 2006.

[6] N. Bhatnagar and B. Venkatesh, "Energy storage and power systems," in *Electrical & Computer Engineering (CCECE)*, 2012.

[7] S. Swaminathan and R. Sen, "Review of power quality applications of energy storage systems," Sandia national lab, 1997.

[8] J. Mundackal, A. C. Varghese, P. Sreekala and V. Reshmi, "Grid power quality improvement and battery energy storage in wind energy systems," in *Emerging Research Areas and 2013 International Conference on Microelectronics, Communications and Renewable Energy (AICERA/ICMiCR)*, 2013.

[9] T. Sels, C. Dragu, T. V. Craenenbroeck and R. Belmans, "Overview of new energy storage systems for an improved power quality and load managing on distribution level," in *Electricity Distribution*, 2011.

[10] S. Yeleti and Y. Fu, "Effect of energy storage on the future of power systems," in *North American Power Symposium (NAPS)*, 2010.

[11] "Grid energy storage," US department of energy, 2013.

[12] G. Delille, B. Francois and G. Malarange, "Dynamic Frequency Control Support by Energy Storage to Reduce the Impact of Wind and Solar Generation on Isolated Power System's Inertia," *IEEE TRANSACTIONS ON SUSTAINABLE ENERGY*, vol. 3, no. 4, 2012.

[13] R. Carnegie, P. Preckel, D. Gotham and D. Nderitu, "Utility Scale Energy Storage Systems," DOE, State Utility Forecasting Group, 2013.

[14] M. Guerrero, E. Romero, F. Barrero, M. i. Milanes and E. Gonzalez, "Overview of Medium Scale Energy Storage Systems," in *Compatibility and Power Electronics*, 2009.

[15] M. Makarov, J. Ma, S. Lu and T. Nguyen, "Assessing the Value of Regulation Resources Based on Their Time Response Characteristics," Paccific Northwest National Laboratory, US Department of Energy, 2008.

[16] D. Stroe, M. Świerczyński, A. I. Stan and R. Teodorescu, "Experimental investigation on the internal resistance of Lithium iron phosphate battery cells during calendar ageing," in *Industrial Electronics Society, IECON 2013*, Vienna, 2013.

[17] B. Multan, A. Shafiul and S. Kumar, "Towards Implementation of Smart Grid: An Updated Review on Electrical Energy Storage Systems," *Smart Grid and Renewable Energy*, vol. 4, 2013.

[18] X. Luo, J. Wang, M. Dooner and J. Clarke, "Overview of current development in electrical energy storage technologies and the application potential in power system operation," *Applied energy*, vol. 137, no. 1, 2015.

[19] H. Chena, T. Conga, W. Yanga, T. C, Y. Lia and Y. Dinga, "Progress in electrical energy storage system: A critical review," *Progress in Natural Science*, vol. 13, no. 2, 2009.

[20] H. Kiehne, Battery Technology Handbook, John Wiley and Sons, 2003.

[21] D. Linden and T. Reddy, Handbook of Batteries, McGraw-Hill, 2002.

[22] G. Dupont, B. Homburg and P. Baltus, "Dimensioning and Grid Integration of Mega Battery Energy Storage System for System Load Levelling," in *IEEE PowerTech Conf.*, Bucharest, 2009.

[23] Z. Wangand and S. Wang, "Grid Power Peak Shaving and Valley Filling Using Vehicle-to-Grid Systems," *IEEE Trans. on Power Delivery*, vol. 28, no. 3, 2013.

[24] X. Li, D. Hui and X. Lai, "Battery Energy Storage Station (BESS)-Based Smoothing Control of Photovoltaic

(PV) and Wind Power Generation Fluctuations," *IEEE Trans. on Sustainable Energy*, vol. 4, no. 2, 2013.

[25] C. Hill, M. Such, D. Chen, J. Gonzalez and W. Grady, "Battery Energy Storage for Enabling Integration of Distributed Solar Power Generation," *IEEE Trans. on Smart Grid*, vol. 3, no. 2, 2012.

[26] J. Eyer, "Electric Utility Transmission and Distribution Upgrade Deferral Benefits from Modular Electricity Storage; A Study for the DOE Energy Storage Systems Program," Sandia national lab, USA, 2009.

[27] H. Zhouxing and W. Jewell, "The role of energy storage in transmission and distribution efficiency," in *IEEE Transmission and Distribution Conf*, 2012.

[28] M. Meyer, P. Balducci, C. Jin and T. Nguyen, Energy Storage for Power Systems Applications, U.S. Department of Energy, 2010.

[29] W. Pei, W. Deng, Z. Shen and Z. Qi, "Operation of battery energy storage system using extensional information model based on IEC 61850 for micro-grids," *IET Generation, Transmission & Distribution*, vol. 10, no. 4, 2016.

[30] P. Garoufalis, Economic Optimisation of Distributed Energy Storage, Masters thesis. Eindhoven University, 2013.

[31] T. Zhang, The Economic Benefits of Battery Energy Storage System in Electric Distribution System, Masters thesis WORCESTER POLYTECHNIC INSTITUTE, 2013.

[32] A. Khatamianfar, M. Khalid, A. V. Savkin and V. G. Agelidis, "Improving Wind Farm Dispatch in the Australian Electricity Market With Battery Energy Storage Using Model Predictive Control," *IEEE Transactions on Sustainable Energy*, vol. 4, no. 3, 2013.

[33] K. Takeda, C. Takahashi, H. Arita and N. Kusumi, "esign of hybrid energy storage system using dual batteries for renewable applications," in *PES General Meeting*, 2014.

[34] J. Zeng, B. Zhang, C. Mao and Y. Wang, "Use of Battery Energy Storage System to Improve the Power Quality and Stability of Wind Farms," in *Power System Technology*, 2006.

[35] Y. L. Ke, Y. C. Chuang, Y. K. Wu and B. T. Jou, "Implementation of a Solar Power Battery Energy Storage System with Maximum Power Point Tracking," in *Industry Applications Society Annual Meeting*, 2010.

[36] Z. Yang, C. Shen, L. Zhang and M. L. Crow, "Integration of a StatCom and battery energy storage," *IEEE Transactions on Power Systems* , vol. 16, no. 2, 2001.

[37] H. Delavaripour, H. R. Karshenas, A. Bakhshai and P. Jain, "Optimum battery size selection in standalone renewable energy systems," in *Telecommunications Energy Conference (INTELEC)*, 2011.

[38] A. Oudalov, Daettwil, R. Cherkaoui and A. Beguin, "Sizing and Optimal Operation of Battery Energy Storage System for Peak Shaving Application," in *Power Tech*, 2007.

[39] B. R. Ke, T. T. Ku, Y. L. Ke, C. Y. Chuang and H. Z. Chen, "Sizing the Battery Energy Storage System on a University Campus With Prediction of Load and Photovoltaic Generation," *IEEE Transactions on Industry Applications*, vol. 52, no. 2, 2016.

[40] Y. Yang, H. Li, A. Aichhorn, J. Zheng and M. Greenleaf, "Sizing Strategy of Distributed Battery Storage System," *IEEE ransaction on smart grid*, vol. 5, no. 2, 2014.

[41] R. Thomas and A. Blum, "Hazard Assessment of Lithium Ion Battery Energy Storage Systems," Fire protection research foundation report, 2016.

[42] D. Conover, "Inventory of safety related codes and standards for energy storage systems," Pacific northwest national lab, 2014.

[43] N. M. L. Tan, T. Abe and H. Akagi, "Design and Performance of a Bidirectional Isolated DC–DC Converter for a Battery Energy Storage System," *IEEE Transactions on Power Electronics*, vol. 27, no. 3, 2012.

[44] J. Zou, C. Peng, J. Shi, X. Xin and Z. Zhang, "State-of-charge optimising control approach of battery energy storage system for wind farm," *IET Renewable Power Generation*, vol. 9, no. 6, 2015.

[45] "Power Grid Electrical Energy Storage," Global smart grid federation, 2016.

[46] J. Neubauer and M. Simpson, "Deployment of Behind the Meter Energy Storage for Demand Charge Reduction," National Renewable Energy Laboratory, 2015.

[47] M. Gorre and P. Rajasekhar, "High voltage battery pack design for hybrid electric vehicles," in *Transportation Electrification Conference (ITEC)*, Chennai, 2015.

[48] Z. Miao, L. Xu, V. R. Disfani and L. Fan, "An SOC-based battery management system for microgrid," *IEEE transaction of smart grid,* vol. 5, no. 2, 2013.

[49] M. Lawder, "Battery Energy Storage System (BESS) and Battery Management System (BMS) for Grid-Scale Applications," in *Proceedings of the IEEE*, 2014.

[50] J. D. Dogger, B. Roosien and Nieuwenhout, "Characterization of li-ion batteries for intelligent management of distributed grid-connected storage," *IEEE Trans on energy conversion,* vol. 26, no. 1, 2011.

[51] K. Tseng, "Energy efficiency of lithium-ion battery used as energy storage devices in micro-grid," in *Industrial Electronics Society*, Yokohama, 2015.

[52] R. Kaushik and I. Mawston, "Coulombic efficiency of lead/acid batteries, particularly in remote-area power-supply (RAPS) systems," *Journal of Power Sources,* 1991.

[53] P. Denholm, J. Jorgenson, M. Hummon, T. Jenkin and D. Palchak, "The Value of Energy Storage for Grid Applications," U.S. Department of Energy, Colorado , 2013.

[54] N. Shidore and T. Bohn, "Round-trip efficiency calculations using Battery HIL," US department of energy.

[55] K. Ng, C. Moo, Y. Chen and Y. Hsieh, "Enhanced coulomb counting method for estimating state-of-charge and state-of-health of lithium-ion batteries," *Journal of Applied Energy,* 2008.

[56] H. Kiehne, Battery technology handbook, Newyork: Marcel Dekker, 2003.

[57] D. Linden and T. Reddy, Handbook of batteries, Mcgraw hill, 2001.

[58] F. Luo and H. Yu, Advanced DC-DC converters, 2004: CRC Press.

[59] M. Kazimierczuk, Pulse-Width Modulated DC-DC Power Converters, Ohio: Wiley, 2015.

[60] S. Filizadeh, Electric Machines and Drives: Principles, Control, Modeling, and Simulation, CRC Press, 2013.

[61] A. Yazdani and R. Iravani, Voltage-sourced converters in power systems, Wiley, 2010.

[62] M. Einhorn, F. V. Conte, C. Kral and J. Fleig, "Comparison, Selection, and Parameterization of Electrical Battery Models for Automotive Applications," *IEEE Transactions on Power Electronics,* vol. 28, no. 3, 2013.

[63] O. Tremblay and L. Dessaint, "Experimental validation of a battery dynamic model for ev applications," *Journal of World Electric Vehicle,* vol. 3, 2009.

[64] C. Edrington, "Virtual battery charging station utilizing power-hardware-in-the-loop: Application to v2g impact analysis," 2010.

[65] J. Mahdavi, A. Emaadi, M. Bellar and M. Ehsani, "Analysis of power electronic converters using the generalized state-space averaging approach," *IEEE Transactions on Circuits and Systems,* 1997.

[66] S. Sanders, M. Noworolski, X. Liu and X. Verghese, "Generalized averaging method for power conversion circuits," *IEEE Transactions on Power Electronics,* 1991.

[67] A. Davoudi, J. Jatskevich and T. D. Rybel, "Numerical state-space average-value modeling of PWM DC-DC converters operating in DCM and CCM," *IEEE Transactions on power electronics,* vol. 21, no. 4, 2006.

[68] J. Sun, D. Mitchell, M. Greuel, P. Krein and R. Bass, "Averaged modeling of PWM converters operating in discontinuous conduction mode," *IEEE Transaction on power electronics,* vol. 16, no. 4, 2001.

[69] P. Krause, O. Wasynczuk and S. D. Sudhoff, Analysis of Electric Machinery and drive systems, IEEE Press, 2002.

[70] E. Tara, Modeling, Optimization and Hardware-in-Loop Simulation of Hybrid Electric Vehicles, PhD dissertation, University of Manitoba, 2012.

[71] J. Larminie and J. Lowry, Electric Vehicle Technology Explained, Wiley & sons, 2003.

[72] X. Li, "Fuzzy adaptive Kalman filter for wind power output smoothing with battery energy storage system," *IET Renewable Power Generation,* vol. 6, no. 5, 2012.

[73] S. W. Mohod and M. V. Aware, "Micro Wind Power Generator With Battery Energy Storage for Critical Load," *IEEE Systems Journal,* vol. 6, no. 1, 2012.

[74] C. A. Hill, M. C. Such, D. Chen and J. Gonzalez, "Battery Energy Storage for Enabling Integration of Distributed Solar Power Generation," *IEEE Transactions on Smart Grid,* vol. 3, no. 2, 2012.

[75] K. Ogata, Modern Control Engineering, Prentice Hall, 2000.